DUAL CURRENT INJECTION-MAGNETIC RESONANCE ELECTRICAL IMPEDANCE TOMOGRAPHY USING SPATIAL MODULATION OF MAGNETIZATION

A THESIS SUBMITTED TO
THE GRADUATE SCHOOL OF NATURAL AND APPLIED SCIENCES
OF
MIDDLE EAST TECHNICAL UNIVERSITY

BY

NASHWAN NAJI

IN PARTIAL FULFILLMENT OF THE REQUIREMENTS
FOR
THE DEGREE OF MASTER OF SCIENCE
IN
ELECTRICAL AND ELECTRONICS ENGINEERING

SEPTEMBER 2016

Approval of the thesis:

DUAL CURRENT INJECTION-MAGNETIC RESONANCE ELECTRICAL IMPEDANCE TOMOGRAPHY USING SPATIAL MODULATION OF MAGNETIZATION

submitted by **NASHWAN NAJI** in partial fulfillment of the requirements for the degree of **Master of Science in Electrical and Electronics Engineering Department, Middle East Technical University** by,

Prof. Dr. Gülbin Dural Ünver
Dean, Graduate School of **Natural and Applied Sciences** ______________

Prof. Dr. Tolga Çiloğlu
Head of Department, **Electrical and Electronics Engineering** ______________

Prof. Dr. Murat Eyüboğlu
Supervisor, **Electrical and Electronics Engineering Department, METU** ______________

Examining Committee Members:

Prof. Dr. Nevzat Gençer
Electrical and Electronics Engineering Department, METU ______________

Prof. Dr. Murat Eyüboğlu
Electrical and Electronics Engineering Department, METU ______________

Prof. Dr. Tolga Çiloğlu
Electrical and Electronics Engineering Department, METU ______________

Assoc. Prof. Dr. Yeşim Serinağaoğlu Doğrusöz
Electrical and Electronics Engineering Department, METU ______________

Assist. Prof. Dr. Özlem Birgül
Biomedical Engineering Department, Ankara University ______________

Date: ______________

I hereby declare that all information in this document has been obtained and presented in accordance with academic rules and ethical conduct. I also declare that, as required by these rules and conduct, I have fully cited and referenced all material and results that are not original to this work.

Name, Last Name: NASHWAN NAJI

Signature :

ABSTRACT

DUAL CURRENT INJECTION-MAGNETIC RESONANCE ELECTRICAL IMPEDANCE TOMOGRAPHY USING SPATIAL MODULATION OF MAGNETIZATION

Naji, Nashwan
M.S., Department of Electrical and Electronics Engineering
Supervisor : Prof. Dr. Murat Eyüboğlu

September 2016, 93 pages

Electrical conductivity of biological tissues provides valuable information on physiological and pathological state of tissues. This may provide conductivity imaging a great potential to have diagnostic applications in clinical field. Developing a method that is able to recognize conductivity variations inside human body has received a great attention over the last decades. Magnetic Resonance Electrical Impedance Tomography (MREIT) is an imaging modality that utilizes current injection during magnetic resonance imaging to visualize conductivity distributions. In conventional MREIT pulse sequence, current is injected once in each repetition time (T_R), which makes scan time quite long. Reducing imaging time helps in avoiding motion artifacts and reducing patient discomfort. In addition, a shorter scan time facilitates improving Signal-to-Noise Ratio (SNR) by averaging, and obtaining 3D images. In this thesis, a novel MREIT pulse sequence is proposed to reduce scan time by injecting two current profiles in each T_R. This pulse sequence utilizes Spatial Modulation of Magnetization (SPAMM) technique to make recovering magnetic flux information due to each injected current profile achievable. This concept is implemented in two different pulse sequences, Spin-Echo (SE) and Gradient-Echo (GE), and evaluated using simulation models and phantom experiments. The performance of the proposed method is investigated in SNR, minimum measurable current and T_2^* relaxation effect. Obtained results demonstrated that the proposed method is able to collect data twice faster with retained resolution, in comparison with the conventional MREIT.

Keywords: conductivity imaging, magnetic resonance, pulse sequence, spatial modulation of magnetization

ÖZ

MANYETİZASYONUN UZAYSAL MODÜLASYONU KULLANILARAK İKİLİ AKIM ENJEKSİYONLU -MANYETİK REZONANS ELEKTRİKSEL EMPEDANS TOMOGRAFİ

Naji, Nashwan
Yüksek Lisans, Elektrik ve Elektronik Mühendisliği Bölümü
Tez Yöneticisi : Prof. Dr. Murat Eyüboğlu

Eylül 2016 , 93 sayfa

Biyolojik dokuların elektriksel iletkenliği dokunun fizyolojik ve patolojik durumu hakkında değerli bilgiler vermektedir. Bu da iletkenlik görüntülemeye, klinik ortamda tanı uygulamalarında kullanılmak üzere büyük bir potansiyel oluşturmaktadır. İnsan vücudu içerisinde iletkenlik değişimlerini fark edebilen bir yöntem geliştirmek son yıllarda yoğun bir ilgi çekmiştir. Manyetik Rezonans Elektriksel Empedans Tomografisi (MREET) manyetik rezonans görüntüleme sırasında uygulanan akımından yararlanarak iletkenlik dağılımını görselleştiren bir görüntüleme yöntemidir. Alışılagelmiş MREET darbe diziliminde, akım tekrarlanma süresinde (TS) bir defa uygulanır, bu da görüntüleme süresinin oldukça uzun hale getirir. Görüntüleme süresinin kısaltılması hareketten kaynaklanan artefaktlerin engellenmesine ve hastanın cihaz içindeki rahatsızlığının azalmasına yardımcı olur. Buna ek olarak, daha kısa görüntüleme süresi, daha fazla averajlama ile Sinyal-Gürültü-Oranının(SGO) iyileştirilmesine ve 3B görüntüler alınmasına imkan sağlar. Bu tezde, her TS'te iki akım uygulama profili yöntemiyle görüntüleme süresini kısaltan yeni bir MREET darbe dizilimi önerilmiştir. Bu darbe dizilimi Manyetizasyonun Uzaysal Modülasyonu (MUM) tekniğinden faydalanarak akım uygulama bilgisini farklı bir biçimde muhafaza eder. Bu yolla farklı profillerden uygulanan akım bilgisinin tek seferde elde edilebilmesine olanak sağlar. Bu konsept iki farklı darbe dizilimi kullanılarak uygulanmıştır: Spin Echo (SE) ve Gradient Echo (GE). Bu yöntem simulasyon modelleri ve fantom deneyleriyle değerlendirilmiş, önerilen yöntemin Sinyal Gürültü Oranı, ölçülebilen en düşük akım değeri ve T_2^* relaksasyon etkisi performansı incelenmiştir. Elde edilen sonuçların gösterdiği üzere önerilen yöntem alışılagelmiş MREET yöntemine kıyasla çözünürlüğü korurken iki kat daha hızlı veri toplayabilmektedir.

Anahtar Kelimeler: iletkenlik görüntüleme, manyetik rezonans, darbe dizilimi,manyetizasyonun uzaysal modülasyonu

To my country and my family

ACKNOWLEDGMENTS

First, I would like to express my deepest gratitude to my supervisor Prof. Dr. Murat Eyüboğlu for his guidance, suggestions, encouragement and support throughout the entire research. His expertise, ample time spent and advices helped me to bring this study into success.

To my parents, Mr. Ameen and Mrs. Nabilah, words are not sufficient to convey my love and gratitude for you. Your love, faith, and endless support were the energy that pushed me always forward throughout my study. You and my brothers and sisters are the meaning of my life.

To Mehdi Sadighi and Kemal Sümser, your encouragements and continuous support during my study in METU mean a lot for me. Without your accompany and advices, completing my research would be much more tough than it was. Thank you so much for your generous help.

I would like also to thank Hasan Hüseyin Eroğlu and Zakaria Alhamadi for their valuable help during this study. Their honest and endless support during experiments were really helpful and unforgettable.

My thanks also go to all my friends I met in Turkey, you made my stay in Turkey much easier than I expected it was going to be. I wish you all the best for your future life and career.

This study is supported by The Scientific and Technological Research Council of Turkey (TÜBİTAK) project 113E979, and Middle East Technical University research grant BAP-07-02-2014-007-470.

TABLE OF CONTENTS

ABSTRACT v

ÖZ vii

ACKNOWLEDGMENTS x

TABLE OF CONTENTS xi

LIST OF TABLES xiv

LIST OF FIGURES xv

LIST OF ABBREVIATIONS xix

CHAPTERS

1 INTRODUCTION 1

- 1.1 Electrical Conductivity of Tissues 1
- 1.2 Electrical Conductivity Imaging 2
- 1.3 Magnetic Resonance Electrical Impedance Tomography . . . 2
  - 1.3.1 MREIT Pulse Sequences 4
  - 1.3.2 MREIT Reconstruction Algorithms 17
- 1.4 Induced-Current Based Conductivity Imaging Techniques . . 19
- 1.5 Thesis Objectives 20

1.6 Thesis Outline 21

2 METHODOLOGY 23

2.1 Spatial Modulation of Magnetization 23

2.2 Forward Problem of MREIT 26

2.3 Conventional Magnetic Flux Measurement Technique 28

2.3.1 Pulse Sequence 28

2.3.2 $\mathbf{B_z}$ Extraction 29

2.4 Proposed $\mathbf{B_z}$ Measurement Technique 30

2.4.1 Pulse Sequence 30

2.4.2 $\mathbf{B_z}$ Extraction 32

2.4.3 Filtering and Spatial Resolution 35

2.4.4 $\mathbf{T_2^*}$ Limitation 37

2.4.5 Signal to Noise Ratio Considerations 38

2.5 Inverse Problem of MREIT 40

3 SIMULATION AND EXPERIMENTAL SETUPS 43

3.1 Simulation Setup 43

3.1.1 $\mathbf{B_z}$ Data Simulation 44

3.1.2 Pulse Sequence Simulation 46

3.2 Experimental Setup 48

3.2.1 Experimental Phantoms 50

3.2.2 Current Source 52

3.2.3 MRI Scanner and Pulse Sequence Design 54

3.2.4 Imaging Parameters 54

4 RESULTS AND COMPARISONS 57

4.1 Simulation Results 57

4.1.1 Uniform Model 57

4.1.2 Non-uniform Model 61

4.1.3 Performance Evaluation of Conductivity Reconstruction 63

4.1.4 Evaluation of Spatial Resolution 66

4.2 Experimental Results 68

4.2.1 Uniform Phantom 69

4.2.2 Non-uniform Phantom 69

4.2.3 Signal to Noise Ratio Measurements 72

4.2.4 Minimum Measurable Current 74

4.2.5 $\mathbf{T_2^*}$ Measurement and Limitation 75

5 CONCLUSIONS 79

REFERENCES 85

APPENDICES

A PUBLICATIONS AND PATENT APPLICATION DURING MASTER OF SCIENCE STUDY 93

A.1 Publications During M.Sc. Study 93

A.2 Patent Application During M.Sc. Study 93

LIST OF TABLES

TABLES

Table 1.1 Summary of MREIT pulse sequences found in literature, listed chronologically. 16

Table 3.1 Meshing details of the used numerical models. 45

Table 3.2 DCI-MREIT pulse sequence parameters used in MRiLab. 48

Table 3.3 Pulse sequences parameters used in MRiLab to collect the data used for evaluating the spatial resolution. 49

Table 3.4 Conductivity values and NaCl ratios in Phantom 2. 52

Table 3.5 Imaging parameters used in collecting the data used for SNR and minimum measurable current calculations. 55

Table 3.6 T_2^* measurement imaging parameters. 55

Table 3.7 Imaging parameters used in estimating maximum usable T_c. 55

Table 4.1 MSE [%] in reconstructed conductivity images from simulated data. 66

Table 4.2 MSE [%] in reconstructed conductivities of the non-uniform phantom. 72

Table 4.3 SNR values of magnitude images obtained by 3 different pulse sequences. 73

Table 4.4 $J_{min}[A/m^2]$ and $I_{min}[mA]$ of 3 different MREIT pulse sequences. . 74

Table 4.5 Calculated T_2^* values for different pairs of echo times. 76

Table 4.6 Calculated signal energy and percentage loss at different T_B durations. 78

LIST OF FIGURES

FIGURES

Figure 1.1 MR pulse sequence used by Scott et al. and given in [15]. 6

Figure 1.2 MR pulse sequence used by Mikac et al. and given in [22]. 180° RF pulses are placed at the zero-crossing of injected AC pulses. 7

Figure 1.3 ICNE pulse sequence used by Park et al. for MREIT [23]. To enhance SNR, current duration is extended till the end of readout period. . 8

Figure 1.4 b-SSFP pulse sequence proposed by Minhas et al. for MREIT [24]. 8

Figure 1.5 ICNE multi-echo pulse sequence proposed by Han et al. for MREIT [26]. In the reference, only a partial illustration of the pulse sequence is presented. 9

Figure 1.6 Non-balanced SSFP pulse sequence versions proposed by Lee et al. for MREIT [27]. a) SSFP-FID and b) SSFP-ECHO. Each of these two pulse sequences is tested with two different current injection patterns, I and II, resulting in four versions. α refers to the flip angle of the RF pulses. 10

Figure 1.7 rDESS pulse sequence proposed by Lee et al. for MREIT [28]. . . 12

Figure 1.8 FGRE pulse sequence used by DeMonte et al and given in [29]. In FGRE pulse sequence, spoiler lobes appear in all gradient axes after the readout period. 13

Figure 1.9 SS-SEPI pulse sequence used by Hamamura and Müftüler for MREIT [20]. To reduce scan time, several k-space lines are collected in a single T_R. 13

Figure 1.10 SPMGE pulse sequence used by Oh et al. for MREIT [30]. Current is injected for the duration of multiple readout lobes. 14

Figure 1.11 SPAMM-MREIT pulse sequence used by Sümser at al. Current is injected between the two hard RF pulses of SPAMM preparation module [32]. 15

Figure 2.1 Simple SPAMM preparation module. T_B is the time gap between the two 90° RF pulses. G_{tag} and T_{tag} are the amplitude and the duration of the tagging gradient lobe. 25

Figure 2.2 Illustration of a) the magnitude image, and b) the magnitude of the k-space image produced using SPAMM. 26

Figure 2.3 Conventional MREIT pulse sequence, based on SE pulse sequence. 29

Figure 2.4 SPAMM-based proposed MREIT pulse sequence. 31

Figure 2.5 An illustration of the magnitude of the k-space image produced using the proposed MREIT pulse sequence. The bottom left and the bottom right signal replicas are indicated by blue-colored and green-colored squares respectively. 34

Figure 3.1 Numerical models: (a)Uniform Model, (b) Non-uniform Model 1, and (c) Non-uniform Model 2. 45

Figure 3.2 A diagram of the proposed pulse sequence implemented using MRiLab. The unit of the time line at the bottom of the diagram is $[ms]$. . 47

Figure 3.3 A diagram of the conventional MREIT pulse sequence implemented using MRiLab. The unit of the time line at the bottom of the diagram is $[ms]$. 49

Figure 3.4 2D sketch of the used experimental phantom at the plane passing through the center of all the electrodes. 50

Figure 3.5 Phantom 1 has a uniform conductivity of $0.5\, S/m$. 51

Figure 3.6 Phantom 2: An object with $\sigma = 1.44\, S/m$ is placed at the center of the phantom to produce a variation in conductivity distribution. 51

Figure 3.7 Schematic diagram of external current switching circuit. 53

Figure 4.1 Uniform model results: (a) B_z^H, and (b) B_z^V generated by injecting current horizontally and vertically respectively. Shown data are given in unit of [T]. 58

Figure 4.2 The magnitude of the k-space data obtained using MRiLab. 59

Figure 4.3 Uniform model results: (a) ϕ_{left} and (b) ϕ_{right} obtained form the left and the right replicas respectively. The unit of the shown phase data is radian (rad). 60

Figure 4.4 Uniform model results: (a) ϕ_H and (b) ϕ_V introduced by the horizontal and the vertical current injections respectively, shown in unit of [rad]. 61

Figure 4.5 Conductivity distribution [S/m] inside the non-uniform model. . . . 62

Figure 4.6 Non-uniform model results: (a) B_z^H and (b) B_z^V obtained using the non-uniform model. Shown data are given in unit of [T]. 62

Figure 4.7 Non-uniform model results: 3D view of spatial frequency low pass filters (a) Square filter H_{square}, and (b) Gaussian filter H_{gauss}. Recovered (c) B_z^H and (e)B_z^V using H_{square}. Recovered (d) B_z^H and (f)B_z^V using H_{gauss}. The unit of the shown magnetic flux density data is [T]. 64

Figure 4.8 Non-uniform model results: Reconstructed (a) σ_{square} and (b) σ_{gauss} from data filtered with H_{square} and H_{gauss} respectively. The unit is [S/m]. . 65

Figure 4.9 $\sigma_{direct}[S/m]$ recovered directly from simulated B_z data. 66

Figure 4.10 Resolution test data: Conductivity $[S/m]$ images in the left column illustrate the distributions used in the simulations. Conductivities in the middle and the right columns are reconstructed from B_z data collected using the standard and the proposed pulse sequences respectively. Six images are given in each column in correspondence to different object diameters: 2, 4, 6, 8, 10 and 12 mm respectively. 67

Figure 4.11 Uniform phantom data: k-space data obtained using (a) SE DCI-MRIET and (b) GE DCI-MRIET pulse sequences. Imaged (c) B_z^H and (e) B_z^V data using SE version of DCI-MRIET pulse sequence. Imaged (d) B_z^H and (f) B_z^V data using GE version of DCI-MRIET pulse sequence. B_z data are shown in [T]. 70

Figure 4.12 Non-uniform phantom data: (a) B_z^H and (c) B_z^V data obtained using SE DCI-MRIET pulse sequence. Imaged (b) B_z^H and (d) B_z^V data using GE DCI-MRIET pulse sequence. (e) σ_{SE} and (f) σ_{GE} reconstructed from the data obtained using SE and GE versions of DCI-MRIET pulse sequence, respectively. 71

Figure 4.13 A plot of the curve that connects the peak values of acquired GE signals is given in red-colored solid-line. A plot of an exponential curve that fits the values of the red-colored curve is given in blue-colored dashed-line. 76

Figure 4.14 Zoomed view of the bottom left signal replica cropped from the k-space data obtained with T_B of (a) 14, (c) 18, and (e) 20 ms. Recovered B_z^H data in corresponding to the data acquired with T_B of (b) 14 ,(d) 18 ,and (f) 20 ms. The unit of the shown magnetic flux density data is [T]. . . 77

LIST OF ABBREVIATIONS

AC	Alternating Current
b-SSFP	Balanced Steady State Free Precession
CDI	Current Density Imaging
DC	Direct Current
DCI-MREIT	Dual Current Injection-Magnetic Resonance Electrical Impedance Tomography
DTI	Diffusion Tensor Imaging
EEG	Electroencephalogram
EIT	Electrical Impedance Tomography
EP	Electrical Properties
FE	Finite Element
FEM	Finite Element Method
FGRE	Fast Gradient Recalled Echo
FID	Free Induction Decay
FSE	Fast Spin-Echo
GE	Gradient-Echo
GUI	Graphical User Interface
IC-MREIT	Induced Current-Magnetic Resonance Electrical Impedance Tomography
ICNE	Injecting Current with Non linear Encoding
LPF	Low Pass Filter
MCU	Micro-Controller Unit
MEG	Magnetoencephalogram
MR	Magnetic Resonance
MRCDI	Magnetic Resonance Current Density Imaging
MREIT	Magnetic Resonance Electrical Impedance Tomography
MREPT	Magnetic Resonance-based Electrical Properties Tomography
MRI	Magnetic Resonance Imaging
MSE	Mean Square Error

NEX	Number of Excitation
rDESS	Reversed Dual-Echo-Steady-State
RF	Radio Frequency
ROI	Region of Interest
SE	Spin-Echo
SMM	Sensitivity Matrix Method
SNR	Signal to Noise Ratio
SPAMM	Spatial Modulation of Magnetization
SPMGE	Spoiled Multi Gradient Echo
SSFP	Steady State Free Precession
SSR	Solid State Relay
SS-SEPI	Single-Shot Spin-Echo Echo-Planar Imaging
TGSE	Turbo-Gradient Spin-Echo

CHAPTER 1

INTRODUCTION

1.1 Electrical Conductivity of Tissues

Tissue electrical conductivity is a quantitative measure that describes the easiness of electrical current passage through biological tissues. Conductivity of tissues has been shown to be inhomogeneous and anisotropic, giving valuable information about the internal ionic contents and structure of tissues [1, 2]. Conductivity of a tissue is also related to its pathological state [3], meaning that conductivity can be used to differentiate between healthy and unhealthy tissues. Therefore, measuring conductivity receives a decent interest from researchers investigating the possible clinical applications, of specially in the area of diagnosing diseased tissues and tumors [4, 5]. Tissue impedance variations on some human organs like lungs, breast and brain have been used in recognizing pathologies [6]. Furthermore, imaging techniques such as electroencephalogram (EEG) and magnetoencephalogram (MEG) require the knowledge of conductivity distribution for more precise source localization [7]. Knowing conductivity distribution is also needed in designing some medical devices such as pacemakers, defibrillators, and electrical stimulation and electro-surgery devices [8, 9].

Conductivity values show a tight dependency on frequency, as a result of the domination of different structural elements at different frequencies. In the range of frequencies below 100 MHz for instance, ions face resistance in the motion across cell membrane, and thus overall conductivity is mainly dominated by the structures of cell membrane. However, in high-frequencies range above 100 MHz the overall conductivity is mainly affected by the concentrations of ions. In biological tissues, frequency of electrical activities is within the range of 0 - 1000 Hz [10]. Therefore, imaging conductivity distribution at this range is of more interest for clinical applications. In the last decades, several imaging modalities for electrical conductivity at low frequency range have been developed. These imaging techniques are discussed in the following sections.

1.2 Electrical Conductivity Imaging

By the need for a technique to image tissue conductivity non-invasively, Electrical Impedance Tomography (EIT) was developed at the end of 1970s by Handerson et al. [11]. In EIT, voltage measurements from surface electrodes are used to compute the conductivity distribution of a volume conductor, by using specific reconstruction algorithms. Several electrodes are placed around the surface of the object being imaged, and then small current in order of few mA is injected through a pair of these electrodes. Boundary potential measurements recorded simultaneously through the remaining electrodes are then used to infer the conductivity of the object [12].

One of the shortcomings of EIT is that its only able to obtain images with low spatial resolution, because of the limitation on the number of electrodes that can be attached to the object surface [13]. Besides, it has a position-dependent sensitivity to the conductivity variations inside the object. This means that this method is not reliable for measuring conductivity of deeper regions far from object surface. Another issue is the errors in boundary measurements arising from the high uncontrollable skin contact impedance. However, benefiting from its low-cost simple design, EIT has found its road to clinical applications and several products have been already available in the market. Recently, EIT devices are being used to measure lungs resistivity for the purpose of monitoring respiratory cycle [14].

1.3 Magnetic Resonance Electrical Impedance Tomography

To overcome the mentioned drawbacks of EIT, another imaging modality has been developed based on Magnetic Resonance Imaging (MRI). MRI is a non-invasive imaging technique used to produce high-resolution images of internal body organs, by utilizing strong magnetic fields and radio frequency waves. Magnetic Resonance Electrical Impedance Tomography (MREIT) is a high-resolution conductivity imaging method that benefits from the resolution and the uniform sensitivity of imaging using Magnetic Resonance (MR) scanners. In this method, current is injected through surface electrodes to the object being imaged using MR scanner. This applied current generates a magnetic flux that influences MR phase images. This magnetic flux carries information about conductivity distribution inside the object, and can be extracted from the obtained MR phase images. After recovering magnetic flux density data, it can be fed to proper algorithms to reconstruct conductivity distribution [9]. Thus in MREIT, data is measured using MR scanner without the need for surface measurements. This way, boundary fault measurements are avoided, as well as the resolution and the sensitivity of the imaging method are significantly improved.

MREIT shares the same forward problem with Magnetic Resonance Current Density Imaging (MRCDI), as both of them utilize the same magnetic flux density measured using MR system as an input for their reconstruction algorithms. MRCDI is an imaging modality used to visualize current density distribution inside a conductive volume. As MREIT, MRCDI uses MR scanner to measure magnetic flux density generated inside imaged object due to current applied to the object through surface electrodes [15]. Therefore, these two imaging techniques use the same MR pulse sequences needed to operate MR scanner during imaging process. Furthermore, many MREIT reconstruction algorithms rely on first finding current density distribution using MRCDI and then recovering conductivity using this current density information [16, 17].

MREIT was first proposed at the beginning of 1990s by Zhang [16], and since then it has been developed among several aspects. MREIT developments can be classified into two main categories: MR pulse sequences and reconstruction algorithms. In the former, pulse sequences used to operate MR scanner are optimized with the purpose to reduce imaging time and improving the Signal to Noise Ratio (SNR) of obtained MR images. While in the latter, the quality of the produced conductivity images is aimed to be improved with respect to noise and resolution by developing more sophisticated reconstruction algorithms. A review through the literature of these two development areas are presented in the following two subsections.

1.3.1 MREIT Pulse Sequences

Before going through MREIT pulse sequences found in the literature, a short review of MR pulse sequence basics and associated terminology is given first. An MR pulse sequence is a set of instructions that operates an MR scanner and controls the changes in gradient fields and Radio Frequency (RF) signals during the imaging process. This pulse sequence is typically represented in a diagram composed of four time lines. These four lines are used to illustrate the shape and the time order of the applied signals by RF coil, slice-selection gradient field G_z, frequency-encoding gradient field G_x, and phase-encoding gradient field G_y respectively, as shown in Figure 1.1. RF pulses are used to excite and flip the net magnetization of the imaged object by a specific angle, called flip-angle. Produced MR signal is then collected frequency by frequency using RF coil. Encoding the frequencies to be collected is done by the gradient fields that spatially vary the frequency of magnetization [18].

The MR signal is collected in the same time duration of a G_x gradient lobe, called read-out gradient. Echo time T_E is the time duration between the middle of the first applied RF pulse (known as excitation RF pulse) and the middle of the read-out gradient. The longer the echo time, the weaker the strength of the collected MR signal. Repetition time T_R is the time between two successive excitation RF pulses, in which pulse sequence is repeated again. A long T_R is usually used to allow the magnetization recovery to its initial state before a new excitation RF pulse is applied. The necessary time for magnetization recovery is known as T_1 relaxation time, in which a full recovery takes about $5T_1$. In some pulse sequences, a 180° RF pulse (known as refocusing RF pulse) is applied at $T_E/2$ to cancel the accumulated phase dispersion in magnetization due to magnetic field inhomogeneity. This phase dispersion is known as T_2^* relaxation. The 180° RF pulse eliminates the T_2^* effect by reversing the sign of the T_2^* phase accumulated until $T_E/2$, which then get canceled by the T_2^* phase accumulated during the other half of T_E [18]. A pulse sequence that contains an excitation and a refocusing RF pulses is known as Spin-Echo (SE) pulse sequence, as the pulse sequence shown in Figure 1.1.

Optimizing MREIT pulse sequence has drawn the attention of many researchers for obtaining better SNR and reducing the needed imaging scan time. Enhancing SNR in

MREIT can be achieved either by reducing noise level in the collected phase images, or by accumulating more current-related phase and thus getting better magnetic flux density data. Better SNR means better quality of recovered conductivity information. Higher SNR also allows obtaining magnetic flux information with lower levels of current being injected. Reducing the level of current used in MREIT plays a major role in making MREIT feasible clinically. Save application of direct current (DC) pulses on human requires the level of current to not exceed 100 μA [19].

Furthermore, reducing signal acquisition time helps in avoiding motion artifacts. Human body is vulnerable to involuntary movements caused by circulatory and respiration systems. Such movements during MR imaging introduce artifacts in the obtained images, specially for organs like heart or lungs. Pulse sequences of long scan time make images more susceptible to these undesired distortions. Motion also troubles improving image SNR by averaging, as even a slight shift in object position during imaging results in a blurring in the averaged image [20].

One of the pulse sequences that aim to improve SNR is illustrated in Figure 1.1, which was used first by Scott et al. for MRCDI in 1991 [15]. This pulse sequence is basically a SE pulse sequence operated simultaneously with bipolar current pulses. Positive pulses of bipolar current are applied before the 180° RF pulses and negative pulses are applied after the 180° RF pulses. Each of these current pulses introduces a phase amount in the MR complex image. Since the 180° RF pulse reveres the sign of the accumulated phase, the phases from the two current pulses are added rather than canceling each other. Accumulating more phase by injecting current pulses with longer durations has been shown as a way to improve SNR [21]. SE based pulse sequences have a merit of canceling the phase dispersion caused by T_2^* relaxation, as mentioned above. If this phase dispersion is not avoided, MR signal decays quickly resulting in a lower SNR. Furthermore, SE is a standard MR imaging pulse sequence provided with many MR scanners. These features of SE-based MREIT pulse sequence made it widely used in MREIT studies.

This pulse sequence has been extended to be used for imaging the current density of alternating current (AC), by using multiple bipolar current cycles along with multiple 180° RF pulses [22]. The 180° RF pulses are centred at the zero-crossing of each

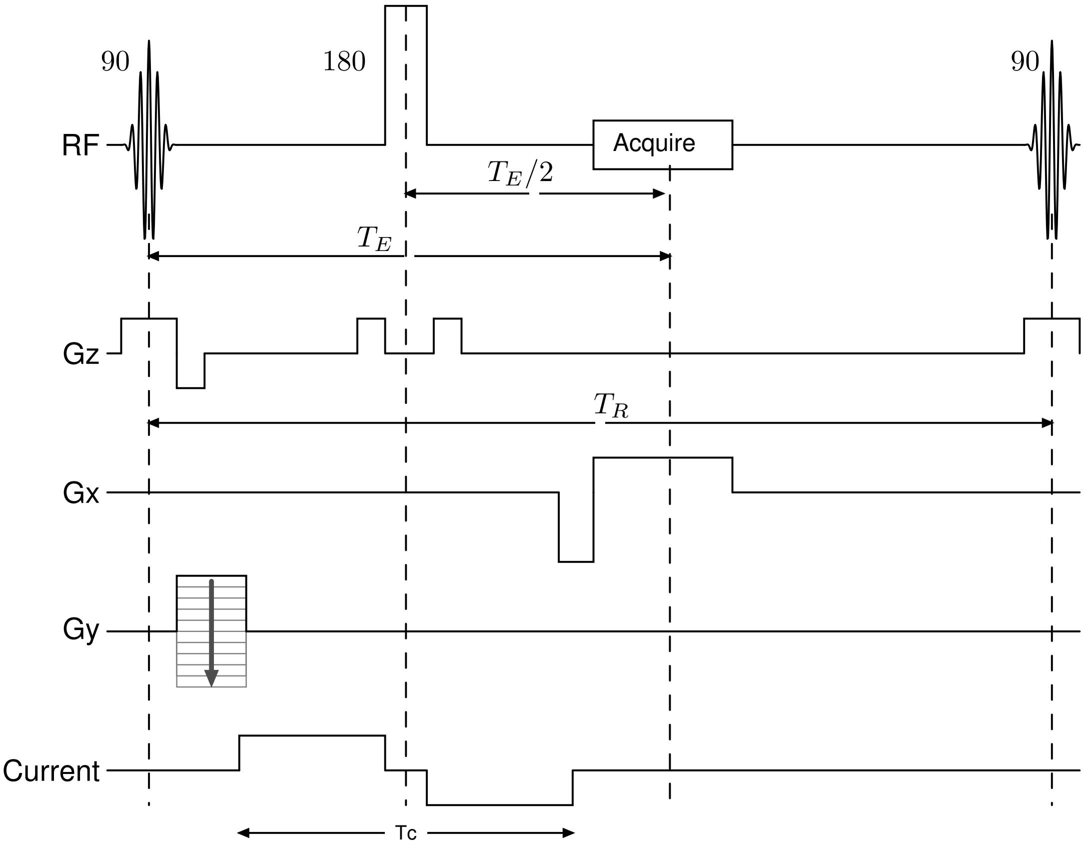

Figure 1.1: MR pulse sequence used by Scott et al. and given in [15].

current pulse cycle to accumulate the phases introduced by each current pulse, as shown in Figure 1.2. This pulse sequence was used by Mikac et al. in 2001 to compare the density distribution of current at different frequencies: 50, 150, 250, 1 K and 100 MHz.

With the aim to further enhance the SNR of MREIT measurements, in 2007 Park et al. introduced the idea of injecting current for a longer duration till the end of the read-out gradient pulse [23], as shown in Figure 1.3. This way, more current-related phase is accumulated without increasing echo time T_E, and thus without lowering the SNR level. However, applying current during the read-out time affects the linearity of the frequency encoding gradient, leading to phase artifacts in obtained MR images. To eliminate these artifacts, they introduced a new way to extract magnetic flux density information from the obtained phase images using their proposed pulse sequence. This pulse sequence is named as Injecting Current with Non linear Encoding (ICNE).

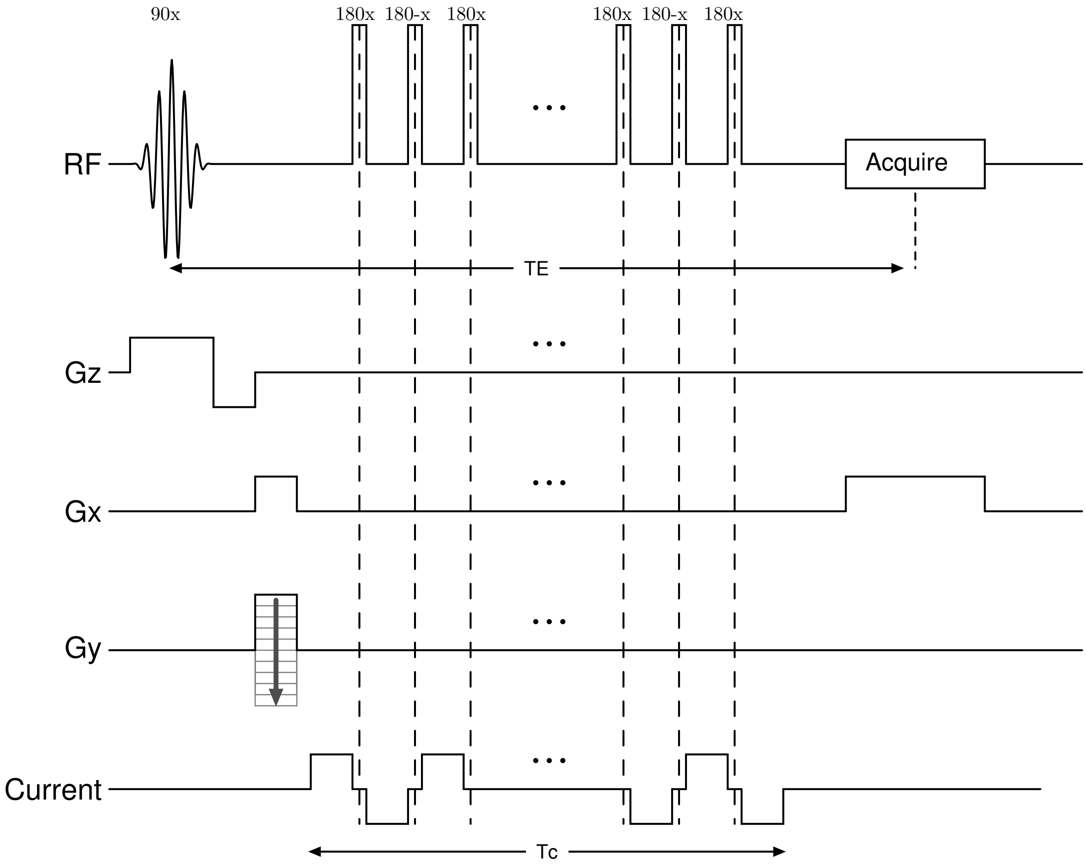

Figure 1.2: MR pulse sequence used by Mikac et al. and given in [22]. 180° RF pulses are placed at the zero-crossing of injected AC pulses.

In 2009, Minhas et al. proposed the usage of Balanced Steady State Free Precession (b-SSFP) pulse sequence for MREIT, depicted in Figure 1.4. In a simulation study, they showed that a b-SSFP pulse sequence is sensitive even to small variations in magnetization phase. Thus, employing this pulse sequence for MREIT would improve SNR and would make injecting current of lower levels possible [24]. However, utilizing this pulse sequence requires the pre-knowledge of T_2^* value at each imaging voxel, and thus additional pre-scans are required. b-SSFP pulse sequence is also sensitive to magnetic field inhomogeneities, leading to ringing artifacts in the acquired images [24]. Later in 2010, the same author demonstrated using simulation results that this pulse sequence can be used for functional MREIT to recognize small variation in conductivity over time [25].

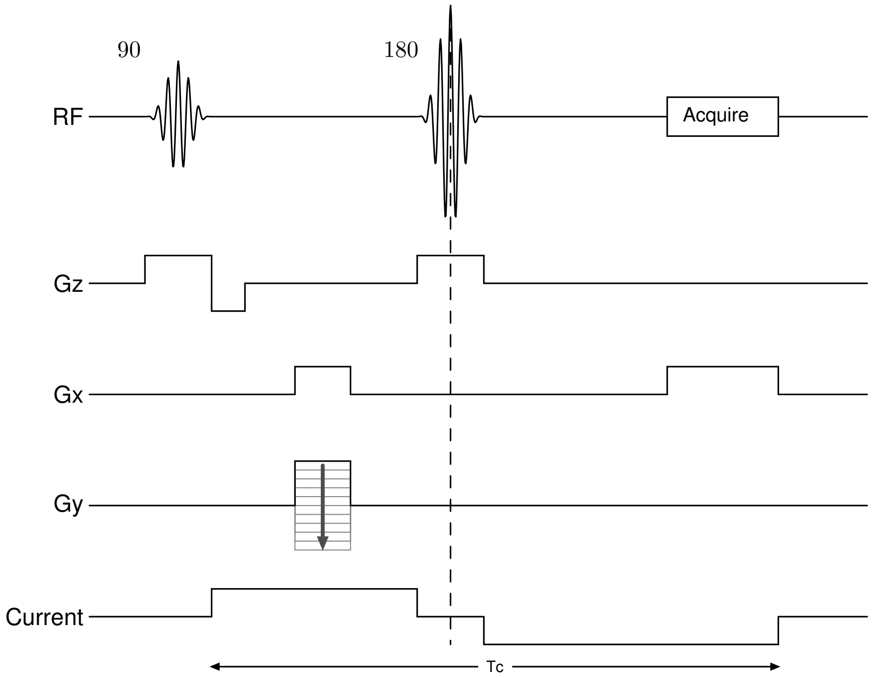

Figure 1.3: ICNE pulse sequence used by Park et al. for MREIT [23]. To enhance SNR, current duration is extended till the end of readout period.

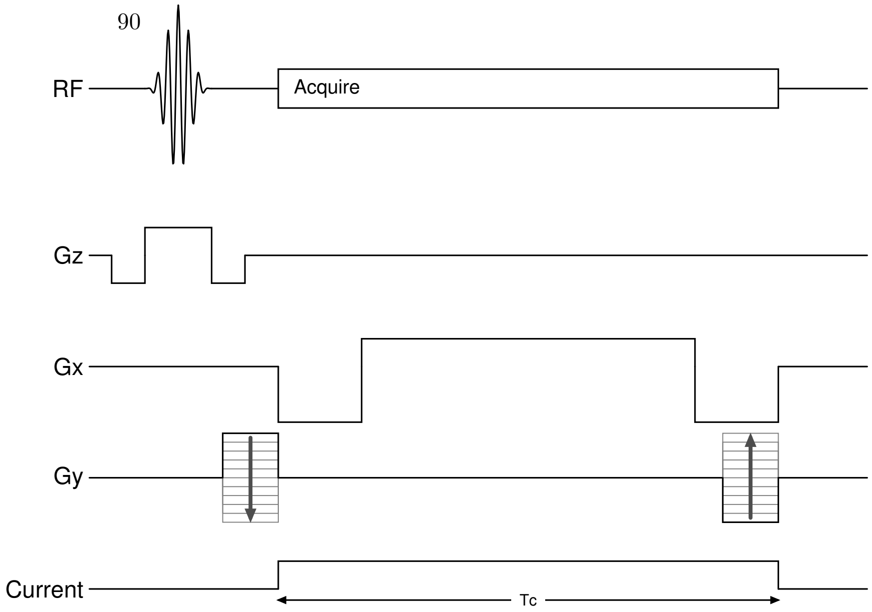

Figure 1.4: b-SSFP pulse sequence proposed by Minhas et al. for MREIT [24].

In 2010, the ICNE technique has been extended by Han et al. to inject current along several echo signals. As illustrated in Figure 1.5, bipolar current was applied along three spin-echoes of the same phase encoding line [26]. This way, each acquired echo signal carries a different amount of current-related phase, with the last echo signal

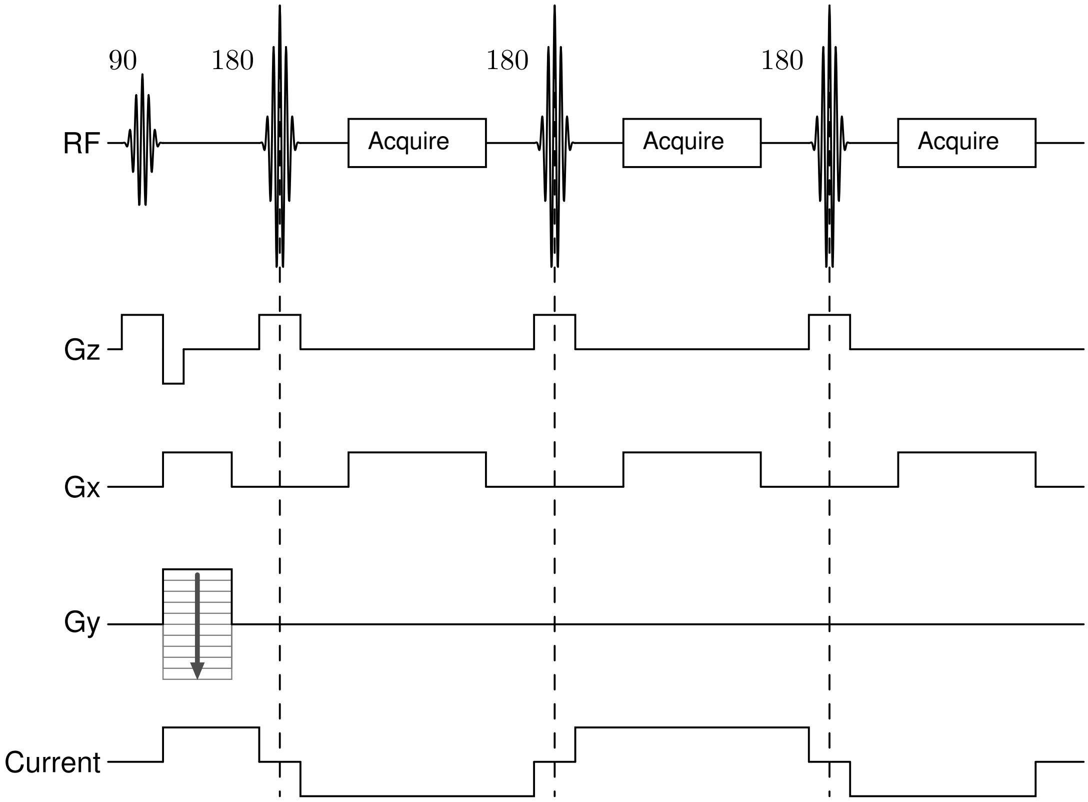

Figure 1.5: ICNE multi-echo pulse sequence proposed by Han et al. for MREIT [26]. In the reference, only a partial illustration of the pulse sequence is presented.

being carrying the most. Extracted magnetic flux density information from each echo signal are combined using proper weighting coefficients. Using this method, SNR is improved by the prolonged current injection, and the required scan time is also reduced in the sense that signal averaging is done by collecting three versions of the same signal in the same repetition time T_R.

In 2015, Lee et al. demonstrated experimentally the possibility of using non-balanced Steady State Free Precession (SSFP) pulse sequence for imaging conductivity. This pulse sequence has the merit of being high sensitive to small phase changes, and also requiring short scan time [27]. In their study, four different configurations of SSFP-MREIT technique were evaluated: the combinations of two pulse sequence versions and two current injection patterns. As shown in Figure 1.6(a), the first version is a Free Induction Decay (FID) SSFP pulse sequence, SSPF-FID. The other version is named SSFP-ECHO, which differs from the former by having G_z and G_x gradient signals being reversed with respect to time, as illustrated in Figure 1.6(b).

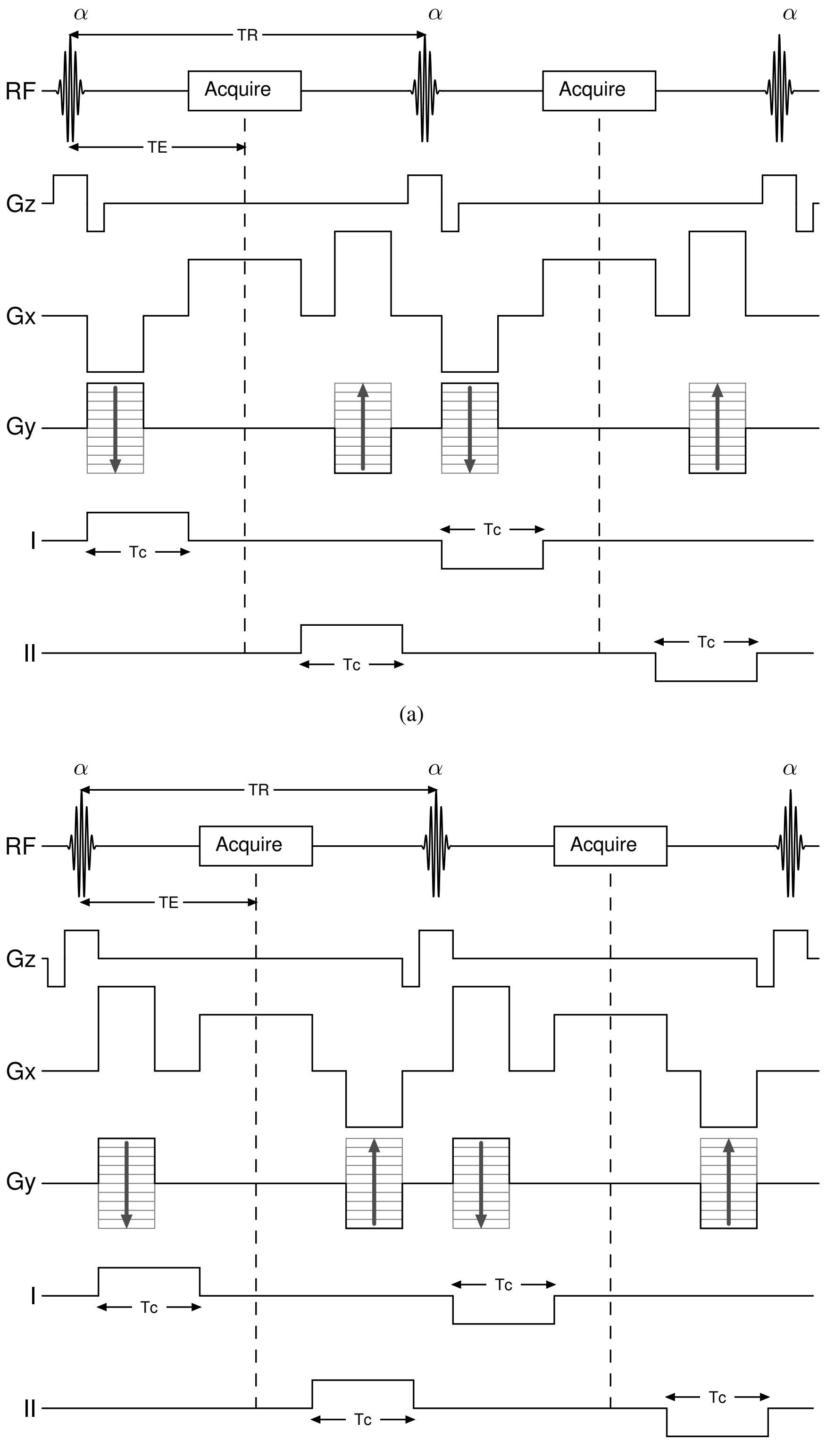

(a)

(b)

Figure 1.6: Non-balanced SSFP pulse sequence versions proposed by Lee et al. for MREIT [27]. (a) SSFP-FID and (b) SSFP-ECHO. Each of these two pulse sequences is tested with two different current injection patterns, I and II, resulting in four versions. α refers to the flip angle of the RF pulses.

Each of these two pulse sequences was tested with two different bipolar current patterns: (I) applied after the RF pulse, or (II) applied after the readout gradient. Obtained results showed that the best SNR was achieved by using SSPF-FID pulse sequence with current being injected immediately after the RF pulses (pattern I). This pulse sequence promises higher SNR using shorter scan time. However, its operation is limited with short T_R, and thus current can be injected for only short time duration. In addition, utilizing this pulse sequence assumes that T_1, T_2 and flip-angle values are known at each imaging voxel, which necessitates additional acquisitions, and therefore longer imaging time. Furthermore, with this pulse sequence the relation between the acquired phase image and magnetic flux density becomes non-linear and thus sophisticated algorithms are needed for recovering magnetic flux density data [27].

Later in 2016, another version of SSFP pulse sequence was proposed for MREIT by Lee et al. In this new version, both G_z and G_y gradient are used for phase-encoding along k_z and k_y direction respectively. G_x is used for frequency-encoding but with reversed readout polarity, as shown in Figure 1.7. This way, two echo signals are collected in each T_R: SSFP-ECHO before readout duration, and SSFP-FID after readout duration. Current pulses are injected in-between these two echo signals [28]. This pulse sequence was given the name reversed dual-echo-steady-state (rDESS). According to the authors, these two signals can be used to estimate current-related magnetic flux density, as well as T_1 and T_2 information. In comparison with the pulse sequence introduced in [27], this method eliminates the need for pre-scans to estimate T_1 and T_2 information. However, rDESS still need prior knowledge of flip-angle map at each imaging voxel. The duration of the injected current is also limited by the very-short T_R associated with SSFP pulse sequences.

From another perspective, several studies have proposed pulse sequences for reducing imaging scan time in MREIT, to avoid possible motion-related distortions in the obtained images. In 2003, DeMonte et al. used Fast Gradient Recalled Echo (FGRE) pulse sequence for rapid MRCDI imaging of animal heart tissues [29]. As shown in Figure 1.8, this pulse sequence is a typical Gradient-Echo (GE) based pulse sequence accompanied with current pulse injected after excitation RF pulses. GE based pulse sequences are typically used for fast imaging, where minimal echo time T_E is de-

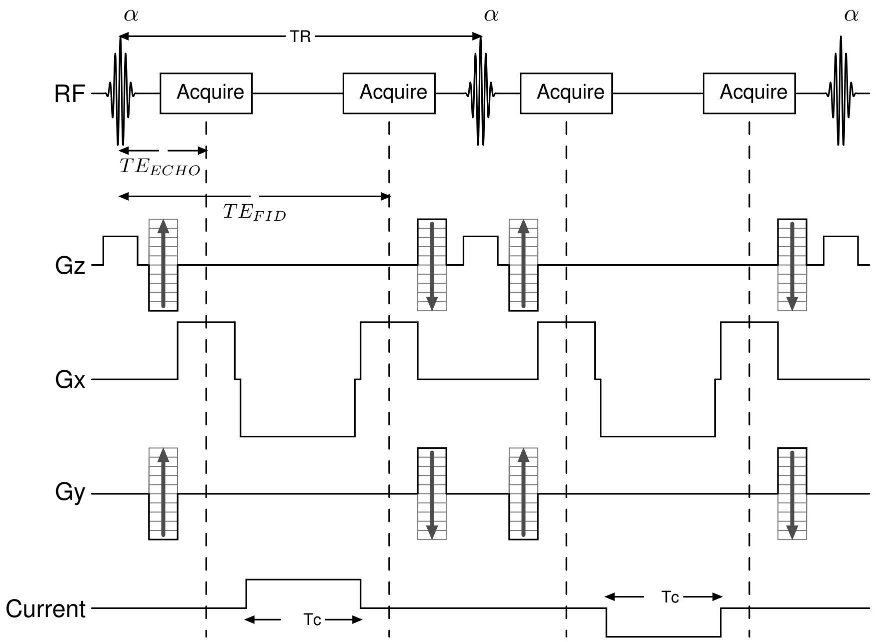

Figure 1.7: rDESS pulse sequence proposed by Lee et al. for MREIT [28].

sired. In GE pulse sequences, no 180 RF pulse is used and thus echo signal can be collected immediately after the de-phasing frequency-encoding gradient lobe. Furthermore, low flip-angle is usually used in GE-based pulse sequences to allow faster recovery for magnetization and thus shorter T_R can be used. However, reducing flip-angle reduces the SNR of the acquired MR signal. In their study, they injected current pulses of 4 ms duration to minimize T_E and to avoid possible distortions due to heart beating. However, they used a large amplitude for current pulses, 150 mA, to improve the quality of extracted magnetic flux density data.

Another study that aimed to reduce the scan time in MREIT was conducted by Hamamura and Müftüler in 2008. They proposed obtaining MREIT data in a single acquisition using Single-Shot Spin-Echo Echo-Planar Imaging (SS-SEPI) pulse sequence [20]. This pulse sequence is illustrated in Figure 1.9, where bipolar current is injected around the 180° RF pulse, and then the whole k-space signal is collected using Echo-Planar trajectory in a single T_R. However, images obtained using SS-SEPI pulse sequence suffered from artifacts like ghosting and geometric distortions, and fixing these artifacts required additional image acquisitions.

The concept of ICNE has also been implemented with GE based pulse sequence for fast imaging applications of MREIT. As shown in Figure 1.10, ICNE method is utilized with Spoiled Multi Gradient Echo (SPMGE), such that current is injected along several acquisitions of the same frequency encoding line of k-space signal. As a result, multiple versions of the signal are acquired, and each phase image has a different

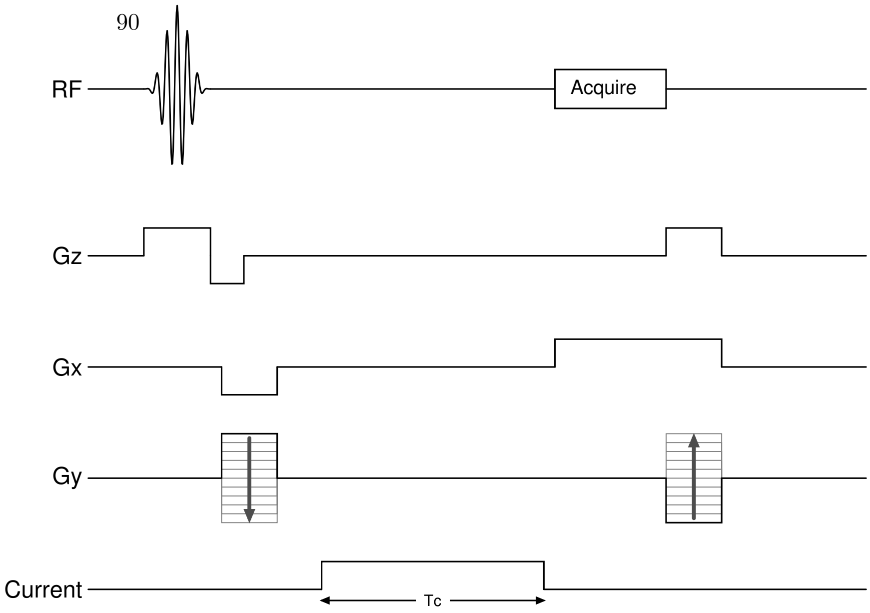

Figure 1.8: FGRE pulse sequence used by DeMonte et al and given in [29]. In FGRE pulse sequence, spoiler lobes appear in all gradient axes after the readout period.

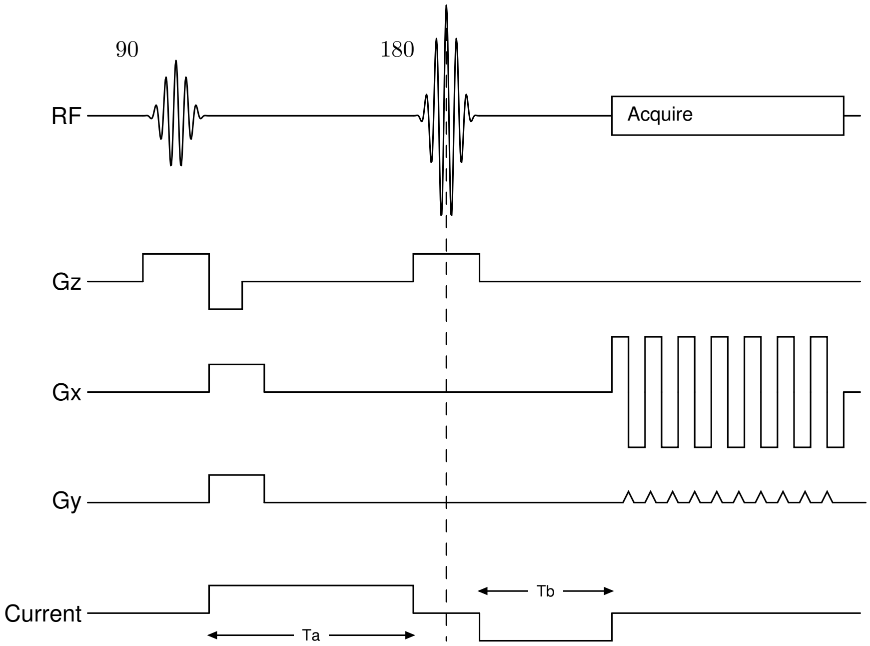

Figure 1.9: SS-SEPI pulse sequence used by Hamamura and Müftüler for MREIT [20]. To reduce scan time, several k-space lines are collected in a single T_R.

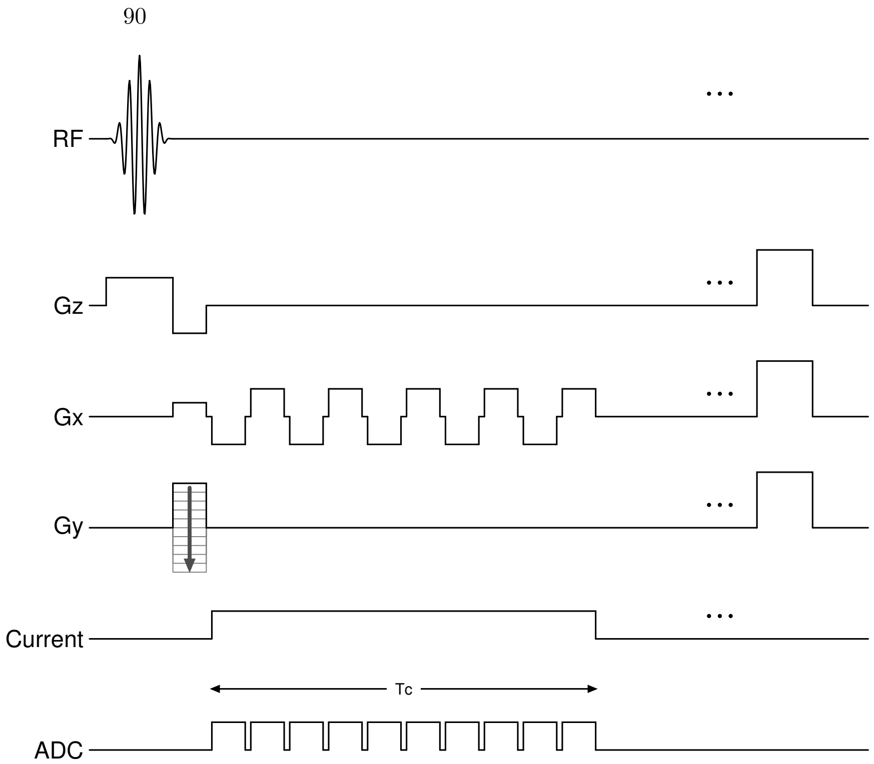

Figure 1.10: SPMGE pulse sequence used by Oh et al. for MREIT [30]. Current is injected for the duration of multiple readout lobes.

magnetic flux density information. These density data can be extracted and combined using proper weights [30]. Compared with the pulse sequence shown in Figure 1.5, this pulse sequence further reduces scan time by excluding the needed time for 180° RF pulses. The ability of this pulse sequence for fast imaging was demonstrated experimentally in [31], in which this pulse sequence was utilized for monitoring RF ablation treatment on an ex-vivo bovine muscle tissue. In their study, obtained conductivity distribution was updated every 10.24 s [31].

Recently, Sümser et al. have proposed a new pulse sequence based on Spatial Modulation of Magnetization (SPAMM) with the purpose to further reduce image acquisition time [32]. In SPAMM, a combination of RF pulses and gradient lobes are used to modulate the intensity of MR images along predefined direction. The pulse sequence proposed by Sümser et al. is shown in Figure 1.11, in which current is injected within a SPAMM preparation module that is theoretically can be combined with any imaging pulse sequence. Injecting current in a preparation module before the beginning of the actual imaging pulse sequence is what gives this method a potential for fast imaging.

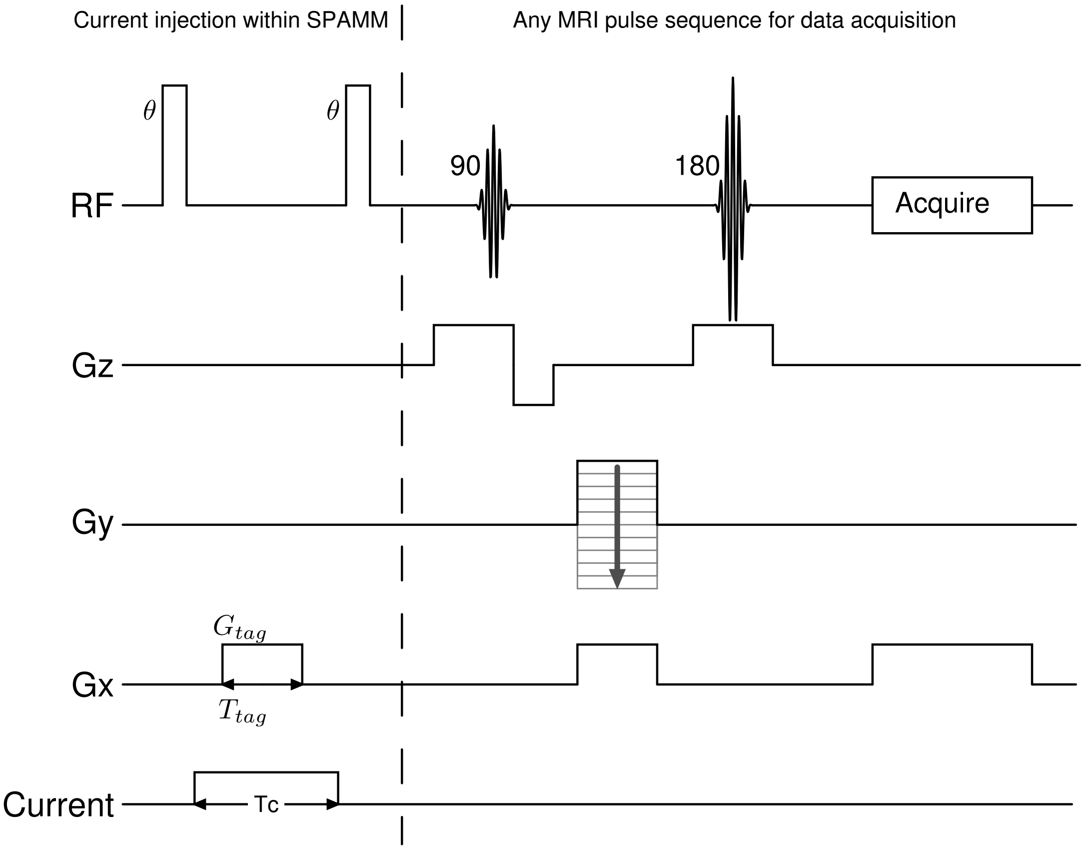

Figure 1.11: SPAMM-MREIT pulse sequence used by Sümser at al. Current is injected between the two hard RF pulses of SPAMM preparation module [32].

In their study, the concept was tested with SE and GE pulse sequences, with better performance was observed from the SE version. This method results in two signal replicas in k-space, each of them carries a current-related phase information. These two signals are transformed separately into spatial domain, and then magnetic flux density data are extracted from their phases.

A summary of MREIT pulse sequences related studies is given in Table 1.1, in chronological order. In this Table, B_0 refers to the main magnetic field strength of the used MR scanner, measured in Tesla (T). I_c refers to the amplitude of the injected current in each of the listed studies.

Table 1.1: Summary of MREIT pulse sequences found in literature, listed chronologically.

Year	1st Author	Used for	Features	PS Type	B_0	I_c	T_c	Measurement	Notes
1991	Scott [15]	MRCDI	No T2* effect	SE	2 T	30 mA	100 ms	Phantom	
2001	Mikac [22]	MRCDI	AC-CDI imaging	SE multiple 180° RF pulses	2.35 T	100 mA 50 mA	20 ms	Phantom & wood twig	
2003	DeMonte [29]	MRCDI	Reduced T_E for cardiac app.	FGRE	1.5 T	150 mA	4 ms	Phantom & animal	Post-mortem animal
2007	Park [23]	MREIT	improved SNR	SE ICNE	3 T	20 mA	*21 ms *25 ms	Simulation & phantom	Special algorithm for extracting Bz
2008	Hamamura [20]	MREIT	Reduced scan time	SS-SEPI	4 T	4 mA	29.9 ms	Phantom	More scans to Fix EPI artifacts
2009	Minhas [24]	MREIT	improved SNR	b-SSFP	-	-	-	Simulation	Sensitive to field inhomogeneities
2010	Han [26]	MREIT	improved SNR & reduced scan time	Multi echo ICNE	3 T	20 mA	*42 ms *59 ms *94 ms	Animal	
2014	Oh [30]	MREIT	improved SNR	SPMGE ICNE	3 T	10 mA	*35.2 ms *70.4 ms	Phantom	
2015	Lee [27]	MREIT	SNR& Reduced scan time	SSFP-FID & SSFP-ECHO	3 T	10 mA	10 ms	Simulation & Phantom	Pre-scans needed to find T_1, T_2, α
2016	Lee [28]	MREIT	SNR& Reduced scan time	rDESS	3 T	10 mA	10 ms	Simulation & Phantom	Pre-scan for α & short T_c
2016	Sümser [32]	MREIT	Potential for reducing scan time	SPAMM-SE & SPAMM-GE	3 T	20 mA	17 ms	Phantom	

*This value is not stated in the corresponding study, but calculated from the material presented in the study.

1.3.2 MREIT Reconstruction Algorithms

Conductivity reconstruction in MREIT is another research area of which many studies have been devoted to enhance. The first reconstruction algorithm was introduced by Zhang in 1992. In his study, Zhang proposed combining EIT and Current Density Imaging (CDI) to produce conductivity maps. Surface measurements of voltages from electrodes along with current density data collected using CDI are used to reconstruct conductivity distribution [16]. The resolution of the recovered conductivity in his simulation study was limited by the number of voltage measurements.

Another work that utilized CDI data for recovering conductivity, with no need for surface measurements, was introduced by Woo et al. in a simulation study. In the work that was published in 1994, the conductivity was recovered by employing the sensitivity relation that maps conductivity variations into changes in current density [17]. Reconstructing conductivity from current density information is known as J-based reconstruction. In J-based methods, current density distribution is found first, which requires the knowledge of all the components of current-generated magnetic flux density $\overrightarrow{B} = (B_x, B_y, B_z)$. Imaging these three components requires rotating the object being imaged inside MR scanner twice. This is because only the $\overrightarrow{B}$ component that is along the direction of the main field can be imaged. In the past two decades, several J-based algorithms have been developed, some of them require multiple voltage measurements from the object surface [33, 34, 35, 36], while others need only a single measurement [37, 38, 39, 40]. Some algorithms are iterative [33, 34, 37, 38], and others are not [35, 36, 39]. A J-based algorithm that omits the need for object rotation has also been introduced in [40], in which only one $\overrightarrow{B}$ component is used to estimate current density in an iterative manner. Then, estimated current density information is used to recover conductivity.

The other class of MREIT algorithms does not require finding current density information, but instead recovers conductivity directly from the measured magnetic flux density data. This class of algorithms is known as B-based algorithms, relying on measuring only one component of $\overrightarrow{B}$. This component is conventionally B_z; the component that is in the direction of the main magnetic field. In 1998, first B-based algorithm was introduced by Ider and Birgül. Their algorithm utilizes the sensitivity of magnetic flux density to conductivity variations [41]. This sensitivity relation was linearized for conductivity variations around an initial value, and the equations that describe this relation were formulated in a matrix form, named as sensitivity matrix. This matrix for a specific shaped object can be calculated numerically on a simulation model. This matrix along with magnetic flux measurements are then used to recover conductivity map. This method was given the name Sensitivity Matrix Method (SMM), and it has been used in several studies for recovering conductivity from simulated and experimental data [20, 32, 42, 43, 44].

Another B-based algorithm that relies only on one component of magnetic field distribution was published by Oh et al. in 2003. This method, named Harmonic Bz, utilizes the concept of layer potential integral to recover the distribution of absolute conductivity in an iterative manner [45]. The iterative nature of this method was not effective against noise presented in the measured magnetic flux density distribution. Later in 2011, a modified version of Harmonic Bz algorithm was proposed by Seo et al. in which the need for iterations was avoided in the new algorithm [46]. Beside simulation models and phantoms, Harmonic Bz algorithms have been used for reconstructing conductivity distributions of animal organs and human knee [47].

The performance of the SMM and the Harmonic Bz algorithms were compared using experimental measurements by Arpinar et al. in 2012. In their study, two current levels were used for injection: 200 μA and 5mA. Obtained results showed that SMM is more tolerant to noisy magnetic flux measurements than Harmonic Bz [19].

In all above mentioned studies, conductivity was assumed to be isotropic: meaning that it was treated as a scalar quantity, which is not true for all biological tissues. Many tissues show anisotropic conductivity that should be represented as a tensor having directional components, rather than a scalar. First anisotropic conductivity reconstruction algorithm was introduced by Seo et al. in 2004. In their simulation study, 12 electrodes were used for injecting current and obtaining multiple B_z data. The conductivity tensor in their study was assumed to have nine components. Obtained results demonstrated that this algorithm is highly sensitive to noisy data, due to the multiple spatial differentiation of B_z data [48].

In 2007, Değirmenci and Eyüboğlu proposed another algorithm for recovering conductivity tensor based on equipotential projection method. In their study, a four-component conductivity tensor was assumed for a 2D numerical phantom, and two current injection profiles were sufficient for uniquely reconstructing conductivity tensor [49]. Later on, Değirmenci adopted other isotropic conductivity reconstruction algorithms found in literature for recovering conductivity tensor. These algorithms are J-substitution, hybrid J-substitution, SMM and Harmonic Bz [50, 51].

In 2014, Kwon et al. introduced a new method for reconstruction anisotropic conductivity by utilizing the relation between conductivity tensor and water diffusion tensor. In their method, the eigenvalues of conductivity tensor were related to those of water diffusion tensor by a position-dependent scalar. Therefore, conductivity tensor can be found by first obtaining diffusion tensor using Diffusion Tensor Imaging (DTI) technique, and then this tensor is scaled by a scalar array found using MREIT [52]. The performance of this method was demonstrated using simulated and experimental measurements.

1.4 Induced-Current Based Conductivity Imaging Techniques

Another class of MR-based conductivity imaging methods utilizes electrical current induction to produce magnetic flux inside the imaging volume. The usage of current induction eliminates the need for the electrodes to be attached on the surface of the object being imaged. Although methods of this class are beyond the scope of this thesis, two of these methods are reviewed in this section. In the method named Induced Current-Magnetic Resonance Electrical Impedance Tomography (IC-MREIT), rapid switching of gradient field signals is utilized to induce eddy currents inside a conductive volume [53]. This way, there is no need for external hardware to produce current pulses, as eddy currents are induced using the built-in MR gradient coils. This method is useful for imaging application in the frequency range below 1 KHz, due to the limitation imposed by the maximum achievable slew rate of the gradient field signals. Although many studies have reported the realization of IC-MREIT experimentally [53, 54, 55, 56], its feasibility still under investigation [57, 58, 59].

Recently, a new method has been emerged to image electrical conductivity, as well as relative permittivity, using MRI at higher frequencies. This method is known as Magnetic Resonance-based Electrical Properties Tomography (MREPT), in which conductivity and relative permittivity information are recovered from the RF field generated by the RF pulses used in MR pulse sequences [60]. MREPT has been experimentally realized, and also using MREPT, electrical properties (EP) images of human brain have been obtained [61, 62]. However, this technique is limited to only the operation frequency of the used MR scanner. This means that imaging EPs at different frequencies requires using different MR scanners, and thus the freedom of selecting the frequency is very restricted. Despite this limitation, MREPT has the potential to help in monitoring the level of RF-field-introduced energy that is absorbed by body tissues during imaging. The rate of this energy absorption represents an important safety issue in high-field MR systems [60].

1.5 Thesis Objectives

The research on the area of conductivity imaging is encouraged by its potential for diagnostic applications, as well as by the need for conductivity information in the design process of some medical devices. MREIT has demonstrated the ability to provide high-resolution conductivity images for animal's organs [47, 63], and human knee [64]. However, MREIT still needs to be optimized in several issues before being introduced clinically. One issue is reducing the level of injected current to the safety level for human application, while sustaining decent quality of the obtained conductivity images. Current levels aimed to be used in MREIT for humans should not be above 100 μA [19]. Another issue is further reducing the acquisition time to avoid artifacts arising from object involuntary motion. Short scan times also reduce patient discomfort during imaging. Furthermore, SNR needs to be improved against unavoidable system noise.

This study focuses on investigating the possibility of further reducing the scan time in MREIT. Based on SPAMM-MREIT pulse sequence introduced in [32], a new pulse sequence is proposed in this study. This pulse sequence reduces the scan time to the half by collecting magnetic flux data for two current injections in one acquisition. To the best of our knowledge, all pulse sequences in the literature measure only one magnetic flux density data in each acquisition. Therefore, this is the first time in which two independent current injections are applied in the same repetition time, and validating this method represents the main objective of this thesis. Another objective for this study is to describe the mathematical foundation of the proposed pulse sequence. In this part, equations required to separate the two current-related magnetic flux density data are to be derived. The concept is then needed to be verified on simulation environment and realized using phantom experiments. Experimentally, the proposed method will be implemented on two pulse sequences: SE and GE. Extracted magnetic flux data using the proposed technique then will be used to reconstruct conductivity image by using SMM algorithm. Critical issues related to the proposed method including possible limitations, achievable spatial resolution and signal to noise ratio are also needed to be discussed.

1.6 Thesis Outline

Chapter 2 starts by explaining SPAMM theory and pulse sequence. Then, the forward problem of MREIT and its conventional pulse sequence are introduced. Afterwards, the proposed method is described along with its mathematics and its magnetic flux density extraction process. Then, considerations about spatial resolution, T_2^* effects and SNR related to the proposed technique are discussed. Finally, SMM reconstruction algorithm is explained.

In Chapter 3, numerical models and software used for simulations along with imaging objects used in experiments are described. This chapter also introduces the used MRI scanner and the pulse sequence parameters used during data acquisition process of this study. Chapter 4 presents the obtained simulation and experimental results, including phase images, magnetic flux density images, reconstructed conductivity and numerical comparisons. Finally, conclusions and future work are given in Chapter 5.

CHAPTER 2

METHODOLOGY

This chapter starts with two sections devoted to explain SPAMM and MREIT, numbered 2.1 and 2.2 respectively. Afterwards, the pulse sequences used for acquiring magnetic flux density data as well as the methods used for extracting them from MR phase images for both the conventional and the proposed techniques are described in detail in sections 2.3 and 2.4 respectively. Some issues, regarding spatial resolution, possible limitations and achievable SNR, related to the proposed method are also discussed from a theoretical prospective in subsections 2.4.3, 2.4.4 and 2.4.5 respectively. Finally in section 2.5, the inverse problem of MREIT is introduced and the used conductivity reconstruction algorithm is explained.

2.1 Spatial Modulation of Magnetization

Modulating magnetization spatially means producing a series of high and low intensity lines in MR images along a predefined spatial direction. This series of stripes are used generally for tagging purposes. In tagging, the deviation of these stripes from the uniform pattern at specific spatial locations reflects the variation of some properties associated with the magnetic fields or the imaged object. Magnetic field related properties that can be recognized using tagging include magnetic field inhomogeneity and gradient fields non-linearities, while those properties related to imaged object include fluid flow and object motion [18]. For instance, tagging has been used for perfusion measurements in which water protons in blood stream are tagged before reaching the imaged slice. As these tagged protons reach the slice of interest, MR intensity changes, and by taking the difference between this obtained intensity image and a reference image without tagging, the change in the intensity can be determined. Then, this change can be converted into quantitative measurement of perfusion using curve-fitting models [18].

Magnetization is modulated using preparation RF pulses applied before a typical imaging pulse sequence. The desired tagging pattern is controlled by gradient pulses, called tagging gradient, applied in combination with the preparation RF pulses. The simple form of SPAMM consists of a gradient lobe applied between two rectangular RF pulses, as illustrated in Figure 2.1. To mathematically explain the generation of tags, without losing generality, it is assumed that the rectangular RF pulses are applied along x axis with a flip angle of 90 degree, and only x gradient is applied between these RF pulses. Starting from an initial magnetization vector ($\overrightarrow{M}$) with a magnitude of M_0 and pointing towards z axis, the first 90° RF pulse flips the magnetization vector into the transversal plane. The three components of $\overrightarrow{M}$ are then expressed in the rotating frame as:

$$\begin{bmatrix} M_x \\ M_y \\ M_z \end{bmatrix} = \begin{bmatrix} 0 \\ M_0 \\ 0 \end{bmatrix} \tag{2.1}$$

The applied x gradient with G_{tag} amplitude and T_{tag} duration causes a phase dispersion in magnetization along x direction, with the amount of

$$\varphi(x) = \gamma x \int_0^{T_{tag}} G_{tag}(t)\, dt \tag{2.2}$$

where γ is the Gyromagnetic ratio. After the dispersion of the introduced phase, $\overrightarrow{M}$ becomes

$$\begin{bmatrix} M_x \\ M_y \\ M_z \end{bmatrix} = \begin{bmatrix} M_0 sin\varphi(x) \\ M_0 cos\varphi(x) \\ 0 \end{bmatrix} \tag{2.3}$$

Then, the second 90° RF pulse flips M_y into $-z$, and thus the longitudinal component of $\overrightarrow{M}$ at the beginning of the imaging pulse sequence becomes

$$M_z(x) = -M_0 cos\varphi(x) \tag{2.4}$$

This means that the equilibrium magnetization is no more M_0 everywhere, but rather it is spatially modulated along x axis. For instance, M_z has a value of M_0 at $x = 0$, but a value of 0 when $x = \pi/2\gamma T_{tag} G_{tag}$. The result is a periodic intensity composed of parallel stripes along y axis, as illustrated in Figure 2.2(a). The distribution of an MR signal in frequency domain is known as the k-space of the MR signal. Transforming the MR signal in (2.4) into frequency domain results the k-space shown in Figure 2.2 (b). As it is shown, the k-space is composed of two signals located symmetrically around vertical axis. This is due to the modulating term, $cos\varphi(x)$, that produces two signal replicas in the k-space centered at $-f_{tag}$ and $+f_{tag}$ respectively.

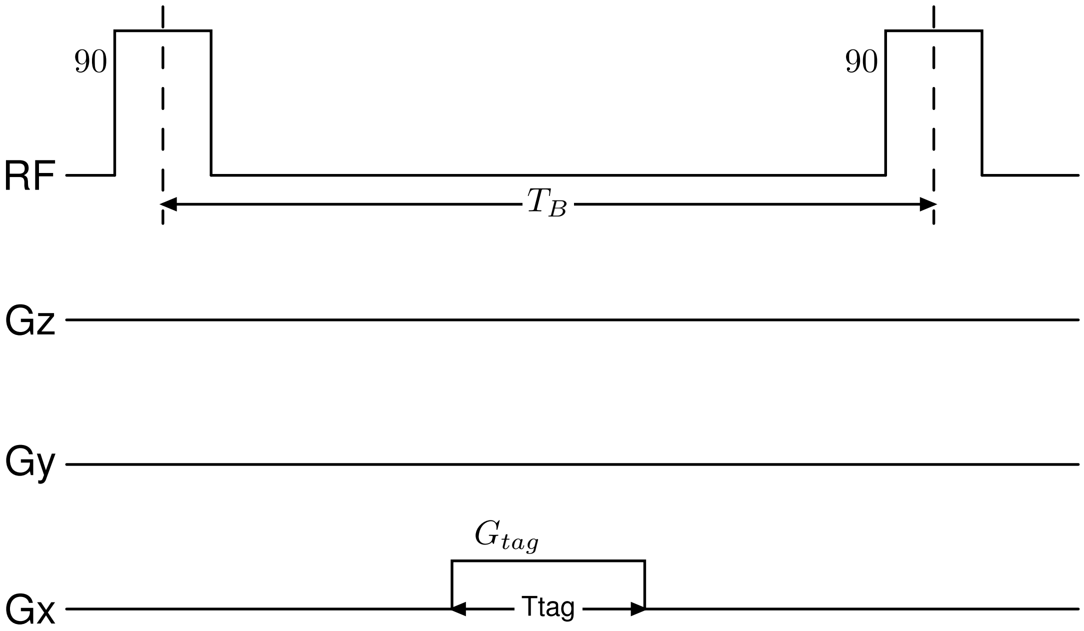

Figure 2.1: Simple SPAMM preparation module. T_B is the time gap between the two 90° RF pulses. G_{tag} and T_{tag} are the amplitude and the duration of the tagging gradient lobe.

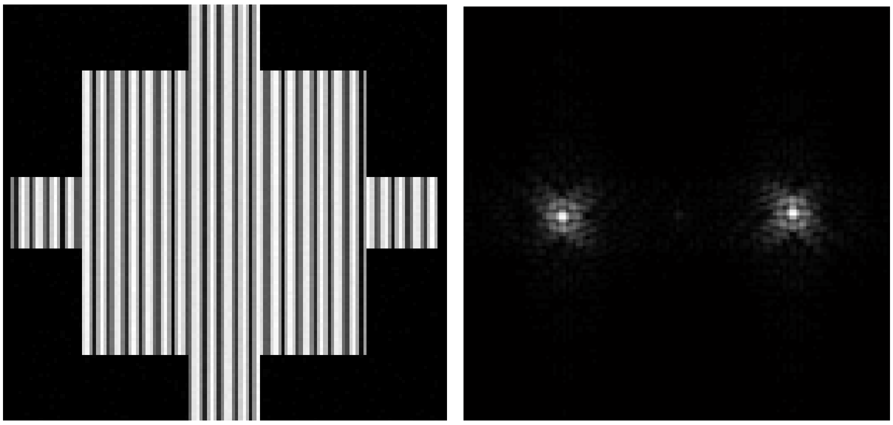

(a) (b)

Figure 2.2: Illustration of (a) the magnitude image, and (b) the magnitude of the k-space image produced using SPAMM.

Assuming a rectangular gradient pulse and integrating (2.2), this tagging frequency can be defined as

$$f_{tag} = \frac{\gamma T_{tag} G_{tag}}{2\pi} \tag{2.5}$$

This frequency identifies the locations of the two signals in the k-space. According to (2.5), increasing G_{tag} or T_{tag} increases the tagging frequency and thus the space gap between the two signal replicas.

SPAMM technique has been used generally for producing a series of parallel stripes, of which any change in their uniformity localizes the location of the underneath change in some system or object properties. However, in this study, the ability of SPAMM to produce two separated signal replicas in k-space is utilized to store different magnetic flux density data in each of these two signal replicas. This idea will be explained in detail in section 2.4.

2.2 Forward Problem of MREIT

In MREIT, electrical conductivity distribution is reconstructed from a magnetic flux density image obtained using an MR scanner. This magnetic flux is generated due to an injected current to the volume being imaged. The forward problem of MREIT describes the relation between the externally applied current and the produced magnetic flux, and how the latter can be computed from a known current density. In this section, the forward problem of MREIT is formulated for 2D isotropic medium referred to here as Ω. Such a formulation is useful for producing simulated data using numerical models. In a 2D object, the conductivity distribution $\sigma(x, y)$ can be related to the distribution of the electrical potential $\Phi(x, y)$ through Poisson's equation as

$$\nabla \cdot (\sigma(x, y)\nabla\Phi(x, y)) = 0 \quad (x, y) \in \Omega \tag{2.6}$$

At boundaries, the relation is defined as

$$\sigma(x, y)\frac{\partial\Phi(x, y)}{\partial\overrightarrow{n}} = \begin{cases} +J & on \quad D^+ \\ -J & on \quad D^- \\ 0 & elsewhere \end{cases} \tag{2.7}$$

where D^+ and D^- are the electrodes of which positive and negative currents are passing through respectively, J is the magnitude of the applied current density, and $\overrightarrow{n}$ is the outward normal unit vector [9]. For a known $\sigma(x, y)$, equations (2.6) and (2.7) can be solved numerically for $\Phi(x, y)$ on a Finite Element solver. Afterwards, the distribution of current density $\overrightarrow{J}(x, y)$ can be computed from $\Phi(x, y)$ as

$$\overrightarrow{J}(x, y) = -\sigma(x, y)\nabla\Phi(x, y) \tag{2.8}$$

This current density is then used to compute the produced $\overrightarrow{B}(x, y)$ using Biot-Savart's Law

$$\overrightarrow{B}(x, y) = \frac{\mu_0}{4\pi}\int \frac{\overrightarrow{J}(x, y)d\Omega \times \overrightarrow{r_R}}{|\overrightarrow{R}^2|} \tag{2.9}$$

where $\overrightarrow{R}$ is the distance vector pointing from the source point to the field point, $\overrightarrow{r_R}$ is the unit vector in that direction, and μ_0 is the vacuum permeability. Therefore, the forward problem of MREIT can be summarized by the following steps. For a given $\sigma(x, y)$ distribution, $\Phi(x, y)$ is obtained by solving (2.6) and (2.7) using Finite Element Method (FEM). This potential is then used to calculated $\overrightarrow{J}(x, y)$ using (2.8). Finally, (2.9) is used to calculate the introduced $\overrightarrow{B}(x, y)$.

2.3 Conventional Magnetic Flux Measurement Technique

Equations (2.8) and (2.9) express that the generated magnetic flux density $\overrightarrow{B}$ due to an injected current to an object, carries information about the electrical conductivity σ of that object. Therefore, acquiring $\overrightarrow{B}$ distribution represents the first step in the procedure of reconstructing σ distribution. This $\overrightarrow{B}$ data can be measured using MR scanner, by injecting current through the imaging object, placed inside MR scanner, in synchrony with a specific MR pulse sequence. The introduced $\overrightarrow{B}$ affects the homogeneity of the scanner main magnetic field B_0. This effect appears in the phase of MR complex image, and by comparing this phase with a reference, the phase due to current-introduced magnetic field can be extracted. However, B_0 is affected by only one component of $\overrightarrow{B} = (B_x, B_y, B_z)$ that is along B_0 direction. Conventionally, the main magnetic field is along z axis, and thus only the z component of introduced magnetic flux, B_z, affects B_0 and can be recovered. Measuring B_z is sufficient for reconstructing isotropic conductivity, which is not the case with anisotropic conductivity reconstruction that requires the knowledge of more than one component of $\overrightarrow{B}$ [65].

2.3.1 Pulse Sequence

As discussed in subsection 1.3.1, a pulse sequence that has been used in many studies of MREIT is developed based on a standard SE pulse sequence. This pulse sequence is illustrated in Figure 2.3, in which a current is injected between the 90° and the 180° RF pulses with positive polarity for a duration of $T_c/2$, and then with a negative polarity for another $T_c/2$ duration after the 180° RF pulse. Thus, the total time duration of the injected current is T_c. A typical k-space signal obtained using SE pulse sequence without current injection can be expressed as

$$S(t) = \int M(x,y)\, e^{j\phi_o}\, e^{-j\gamma(G_y T_p y + G_x t x)}\, dx\, dy \tag{2.10}$$

where $M(x,y)$ represents the magnitude of the complex magnetization in the slice being imaged, G_y and T_p are the strength and the duration of the phase-encoding gradient applied along y axis respectively, and G_x is the strength of the frequency-encoding gradient applied along x axis. The phase ϕ_o refers to the introduced phase due to the main field inhomogeneities and any other possible sources, and t refers to time. If positive current is injected as given in the description above, acquired k-space signal becomes

$$S^+(t) = \int M(x,y)\, e^{j\phi_o + j\gamma B_z(x,y)T_c}\, e^{-j\gamma(G_y T_p y + G_x t x)}\, dx\, dy \tag{2.11}$$

Therefore, the applied current introduces a magnetic flux whose z component appears as an additional phase term in (2.11) defined as $\phi_c = \gamma B_z(x,y)T_c$. This phase term is desired and should be extracted from the complex MR image. The extraction procedure is explained in the following subsection.

2.3.2 B$_z$ Extraction

Taking the 2D inverse Fourier Transform (IFT_{2D}) of $S^+(t)$ yields,

$$IFT_{2D}\{S^+(t)\} = M(x,y)e^{j\phi_o + j\phi_c} \tag{2.12}$$

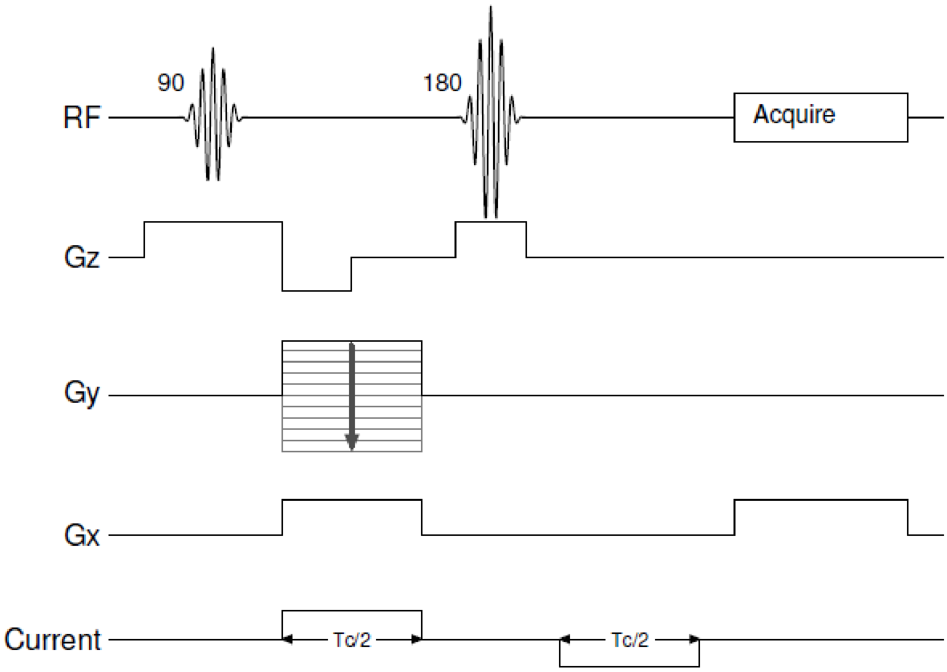

Figure 2.3: Conventional MREIT pulse sequence, based on SE pulse sequence.

which is a complex image with a magnitude of $M(x, y)$ and a phase of $\phi_o + \phi_c$. To separate the desired phase ϕ_c from the other phase term, another MR image obtained without current injection can be used as a reference. By taking the difference between the phases of the MR images obtained with and without the presence of current injection, the phase term solely due to injected current can be extracted. An alternative method for extracting ϕ_c uses the difference between the phase images obtained with positive and negative polarities for the injected current. After extracting ϕ_c, the magnetic flux density can be calculated as

$$B_z(x, y) = \frac{\phi_c}{\gamma T_c} \tag{2.13}$$

2.4 Proposed $\mathrm{B_z}$ Measurement Technique

SPAMM based MREIT pulse sequence has been recently proposed as an alternative for the conventional MREIT pulse sequence providing fast acquisition capabilities [32]. Using SPAMM, two or more signal replicas are produced in k-space. These replicas are extracted individually by windowing in k-space. In [32], current is injected into the imaging volume during the time duration T_B between the two RF pulses of the simple SPAMM described in section 2.1 and illustrated in Figure 2.1.

In this study, a novel SPAMM based technique is proposed to reduce scan time to the half, by injecting two current profiles successively within each T_R. Thus, this new pulse sequence is capable of collecting data two times faster in comparison with conventional MREIT pulse sequence. Throughout this study, this newly proposed method is referred to as Dual Current Injection-MREIT (DCI-MREIT). The proposed pulse sequence and its mathematical foundation are described in the following two subsections.

2.4.1 Pulse Sequence

In the proposed pulse sequence shown in Figure 2.4, the SPAMM module consists of three rectangular RF pulses of 90° flip angle. Between the first and the second RF pulses, x gradient lobe is applied and the first current profile is injected. This current profile can be injected through any electrodes pair: vertically, horizontally or in any possible direction. The second current profile is then applied during the duration between the second and the third RF pulses along with y gradient lobe. Then, a typical imaging pulse sequence follows; a SE for example. An illustration of the k-space signal produced by the proposed pulse sequence is shown in Figure 2.5. There are four signal replicas in the k-space as a result of the SPAMM preparation module.

In the proposed pulse sequence, two current profiles are injected during one T_R, and thus the time needed to collect data is reduced to the half. However, extracting the magnetic flux density data is not straightforward, because phases due to first and second current profiles are mixed and should be separated. The extraction procedure along with the equations needed to recover magnetic flux data due to each current injection are derived in the following subsection.

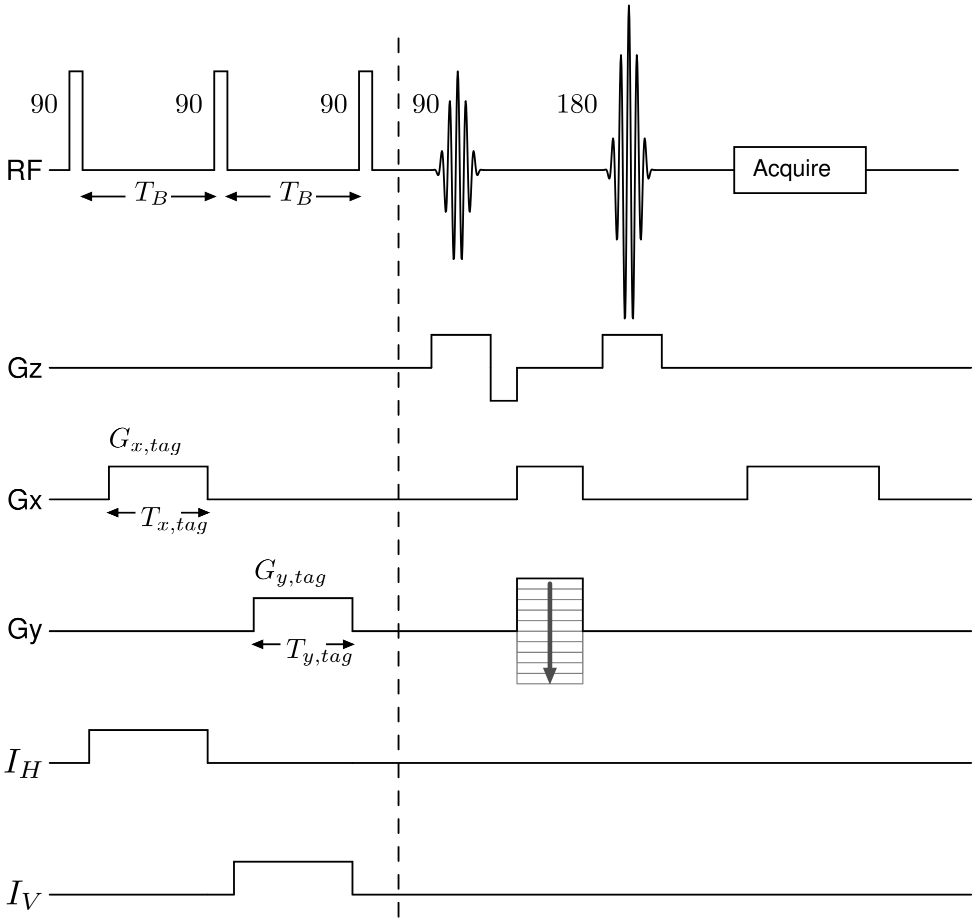

Figure 2.4: SPAMM-based proposed MREIT pulse sequence.

2.4.2 $\mathrm{B_z}$ Extraction

In order to understand how the current related phase terms should be extracted from the collected MR signal, the z component of $\overrightarrow{M}$ produced after the third rectangular RF pulse is derived first. For illustration, injected current profiles are assumed to be horizontal and vertical respectively. All rectangular RF pulses are assumed to be applied along x axis.

According to section 2.1, the magnetization vector after the second 90° RF pulse becomes

$$\begin{bmatrix} M_x \\ M_y \\ M_z \end{bmatrix} = M_0 \begin{bmatrix} sin\varphi_1(x) \\ 0 \\ -cos\varphi_1(x) \end{bmatrix} \tag{2.14}$$

where $\varphi_1(x)$ is the summation of the phase due to the applied x gradient and the phase due the horizontally injected current (ϕ_H) expressed as

$$\varphi_1(x) = \gamma T_{x,tag} G_{x,tag} x + \phi_H \tag{2.15}$$

In (2.15), tagging gradient pulse is assumed to be rectangular to simplify phase calculation. Similarly, the phase accumulated between the second and the third RF pulses can be expressed as

$$\varphi_2(y) = \gamma T_{y,tag} G_{y,tag} y + \phi_V \tag{2.16}$$

where $G_{x,tag}\ T_{x,tag}$ and $G_{y,tag}\ T_{y,tag}$ are the areas of the applied gradient lobes along x and y directions respectively. While ϕ_V is the phase due to the vertical current profile. The phase given in (2.16) causes dispersion in $\overrightarrow{M}$ expressed as

$$\begin{bmatrix} M_x \\ M_y \\ M_z \end{bmatrix} = M_0 \begin{bmatrix} sin\varphi_1(x)cos\varphi_2(y) \\ -sin\varphi_1(x)sin\varphi_2(y) \\ -cos\varphi_1(x) \end{bmatrix} \tag{2.17}$$

Finally, the third 90° RF pulse rotates magnetization once again around x axis, resulting

$$\begin{bmatrix} M_x \\ M_y \\ M_z \end{bmatrix} = M_0 \begin{bmatrix} sin\varphi_1(x)cos\varphi_2(y) \\ -cos\varphi_1(x) \\ sin\varphi_1(x)sin\varphi_2(y) \end{bmatrix} \tag{2.18}$$

As it is seen in (2.18), the z component of $\overrightarrow{M}$ is given as

$$M_z(x,y) = M_0 sin\varphi_1(x)sin\varphi_2(y) = \frac{M_0}{2}[cos(\varphi_1 - \varphi_2) - cos(\varphi_1 + \varphi_2)] \tag{2.19}$$

which is clearly composed from two independent signals, one of them carries the sum of phases (φ_1 and φ_2) and the other carries the difference. the notations of spatial coordinates in (2.19) are omitted for simplicity. The sum and difference of φ_1 and φ_2 represent two independent equations of two unknowns that can be solved. However, these two signals need to be separated first and then their arguments need to be extracted. M_z in (2.19) represents the equilibrium magnetization that is prepared using SPAMM module and will be acquired using the follow-up imaging pulse sequence. Transforming (2.19) into k-space yields

$$M_z(k_r) = \frac{M_0}{4}[\delta(k_r+(\varphi_1-\varphi_2))+\delta(k_r-(\varphi_1-\varphi_2))-\delta(k_r+(\varphi_1+\varphi_2))-\delta(k_r-(\varphi_1+\varphi_2))] \tag{2.20}$$

where k_r represents the k-space coordinates vector, and δ is the Dirac delta function. Equation (2.20) states that the k-space of M_z contains four signal replicas centered at four different locations namely: $\varphi_1 - \varphi_2$, $\varphi_2 - \varphi_1$, $\varphi_1 + \varphi_2$ and $-\varphi_1 - \varphi_2$, as illustrated in Figure 2.5. The k-space data shown in Figure 2.5 is collected using an MR system that uses x-gradient for phase-encoding. To make phase-encoding direction in this data along the conventional direction (i.e., y-axis), the k-space was rotated by -90°. Therefore, k-space coordinates in Figure 2.5 are positive in the bottom left quarter, rather than the bottom right quarter. It is also worthy to remember that each of φ_1 and φ_2 is composed itself from two components: one due to the applied gradient lobe, and the other due to the injected current. The locations of the four signal replicas are determined and controlled by the strength and duration of the applied gradient lobes, according to (2.5). Each of the four replicas presented in Figure 2.5 can be separated by a low-pass windowing, and independently transformed into spatial domain after being shifted to the center of the k-space. During this low-pass filtering process, the component due to gradient lobe is removed, and the remaining phase in the recovered complex image is ideally due to the injected current. Considering the complex image recovered from the bottom left signal replica for instance, the phase becomes

$$\varphi_{left} = \varphi_1 + \varphi_2 \approx \phi_H + \phi_V \tag{2.21}$$

Similarly, the phase of the image recovered from the lower right signal replica becomes

$$\varphi_{right} = \varphi_1 - \varphi_2 \approx \phi_H - \phi_V \tag{2.22}$$

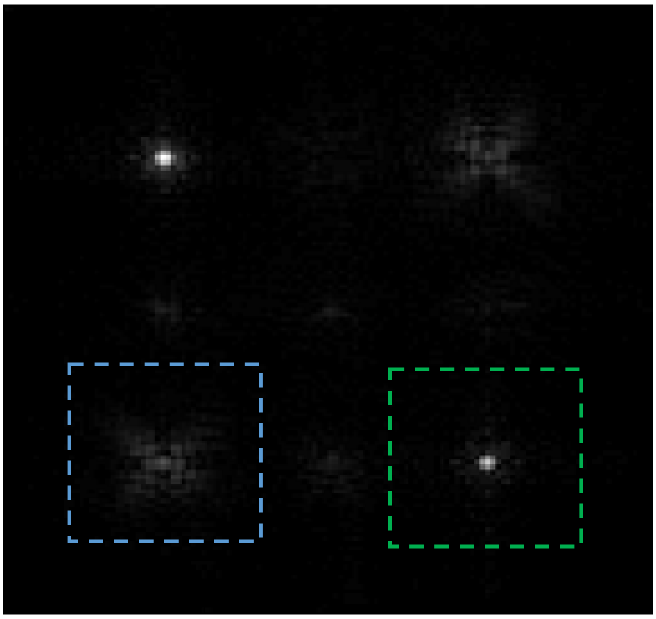

Figure 2.5: An illustration of the magnitude of the k-space image produced using the proposed MREIT pulse sequence. The bottom left and the bottom right signal replicas are indicated by blue-colored and green-colored squares respectively.

Equations (2.21) and (2.22) say that the phases due to current injections can be recovered using the phases of two signal replicas, as follows

$$\phi_H = \frac{\varphi_{left} + \varphi_{right}}{2} \tag{2.23}$$

$$\phi_V = \frac{\varphi_{left} - \varphi_{right}}{2} \tag{2.24}$$

These two equations conclude the procedure of extracting the injected-current related phases from the acquired MR image using the proposed pulse sequence. This procedure is summarized as follows: a pair of signal replicas, either the upper or the lower, are separately windowed in k-space, shifted to the center, and transformed back to the spatial domain. Then, phases due to horizontal and vertical current injections are recovered using (2.23) and (2.24) respectively. These phase images are then scaled using (2.13) to produce the corresponding magnetic flux density images.

2.4.3 Filtering and Spatial Resolution

Extracting the signal replicas from the k-space using a Low-Pass Filter (LPF) is an important preprocessing step that affects the quality of the recovered magnetic flux and conductivity distributions. The usage of a sharp LPF introduces undesired artifacts in the resultant phase images because of its oscillating spatial response. Therefore by using a LPF of smooth cut-off frequency, better phase quality could be obtained. In this study, two low pass filters are used for extracting the left and the right replicas to illustrate the effect of the filter shape. The first filter is a sharp 2D-LPF of square shape mathematically expressed as:

$$H_{square}(k_x, k_y) = \begin{cases} 1 & , |k_x|, |k_y| \leq |k_{off}| \\ 0 & , otherwise. \end{cases} \tag{2.25}$$

where k_{off} is the length of the filter side expressed in number of pixels, and k_x and k_y are the k-space coordinates along x and y axes respectively. The other filter is a

2D Gaussian filter of smooth edges given by [66]

$$Q(k_x, k_y) = e^{\frac{-(k_x^2+k_y^2)}{2\varrho^2}}$$

$$H_{gauss}(k_x, k_y) = \begin{cases} \dfrac{Q(k_x, k_y)}{\sum\limits_{|n_x| \le |k_w|} \sum\limits_{|n_y| \le |k_w|} Q(n_x, n_y)}, & |k_x|, |k_y| \le |k_w| \\ \\ 0, \quad otherwise. \end{cases} \tag{2.26}$$

where k_w is the width of the filter window and ϱ is a positive scalar representing the standard deviation of the filter distribution expressed in number of pixels.

The bandwidth of the used filter affects the spatial resolution of the recovered magnetic flux density distribution and thus the recovered conductivity. Referring to Figure 2.5, a practical filter bandwidth has to cover less than half the k-space width. This limit is chosen to avoid any possible interference from the neighbor signal replicas. In this study, the filter bandwidth is set to be one-third the width of the k-space. This reduction in frequency information affects the spatial resolution of the recovered B_z data. The relation between the spatial resolution Res and the signal bandwidth BW can be expressed as:

$$Res = \frac{1}{2\,BW} \tag{2.27}$$

The bandwidth of H_{square} can be calculated as:

$$BW_{square} = k_{off} \frac{1}{FOV} \tag{2.28}$$

where FOV refers to the width of the imaging window known as the Field Of View. For H_{gauss}, the bandwidth is defined as the frequency in which the spectrum falls to half the maximum value. Mathematically, BW_{gauss} can be calculated as:

$$BW_{gauss} = \sqrt{2\,ln(2)}\varrho \frac{1}{FOV} \tag{2.29}$$

Equation (2.27) states that reducing the bandwidth by a factor of three would result in a three-fold loss in the spatial resolution. On the other hand, the number of the phase encoded lines can be reduced to one-third of the typically acquired number, to cover only the frequencies within the filter bandwidth. This additionally reduces the scan time by a factor of three. This additional gain in speed can be spent in compensating the loss in the resolution. In more detail, collecting three times more frequency samples would increase the scan time by a factor of three, and would result a k-space that is three times wider. Using three-time larger $G_{x,tag}$ and $G_{y,tag}$, signal replicas will be located three times far away from each other. Therefore, a filter of a three-time wider bandwidth can be used, and this way the loss in spatial resolution is compensated. In total, the same spatial resolution is preserved along with the two-fold gain in speed due to dual current injection.

2.4.4 $\mathbf{T_2^*}$ Limitation

In the derivation given in section 2.4.2, only phase terms due to tagging gradients and current injections were assumed to simplify the illustration of the proposed concept. However in practice, another phase term is introduced due to T_2^* relaxation. T_2^* phase appears due to local inhomogeneities in the magnetic field that cause spin isochromats in the transverse plane to de-phase in the time period starting after excitation RF pulse and until the echo time T_E. T_2^* is known as the apparent T_2, the transverse relaxation time. These relaxation times can be related to each other as

$$\frac{1}{T_2^*} \sim \frac{1}{T_2} + \gamma \triangle B \tag{2.30}$$

where $\triangle B$ refers to the local field variations in each imaging voxel [18]. Equation (2.30) states that T_2^* value at each voxel of the object being imaged depends on both the object and the imaging system properties. Therefore, T_2^* values are usually defined for specific tissue at specific main magnetic field strength. MR images obtained using pulse sequences that do not include refocusing RF pulses, such as GE pulse sequence, are weighted by T_2^* phase dispersion. The longer T_E in these pulse sequences, the larger the loss in the obtained image SNR due to T_2^*.

In this section, T_2^* phase is considered in the derivations to describe a more realistic case. Under the assumption that the time duration between the first and the second hard RF pulses is identical to the time duration between the second and the third, identical T_2^* phase dispersions occur in these time durations, and should be included in equations (2.15) and (2.16) as

$$\begin{aligned} \varphi_1 &= \gamma T_{x,tag} G_{x,tag} x + \phi_H + \phi_{T_2^*} \\ \varphi_2 &= \gamma T_{y,tag} G_{y,tag} y + \phi_V + \phi_{T_2^*} \end{aligned} \tag{2.31}$$

Accordingly, φ_{left} and φ_{right} are rewritten as

$$\begin{aligned} \varphi_{left} &= \phi_H + \phi_V + 2\phi_{T_2^*} \\ \varphi_{right} &= \phi_H - \phi_V \end{aligned} \tag{2.32}$$

This implies that the right replica will not be affected by the T_2^* relaxation, like MR images obtained using SE pulse sequence. However, the left replica will be exposed to T_2^* relaxation and will decay quickly, similar to MR images obtained using GE pulse sequence. This can be seen in Figure 2.5, within the time duration between the first and the third RF pulses, the left replica is much quickly decayed than the right replica. Longer durations between RF pulses means more decaying of the left replica and thus more loss in its SNR. This issue puts a limitation on the length of the period between the hard RF pulses T_B, and thus the duration of the injected current T_c.

Since the duration of the injected current plays a major role in enhancing SNR [21] and thus the quality of the recovered conductivity images, possible T_2^* limitation on the proposed pulse sequence has to be investigated. This means determining an upper limit for the possible current injection duration for a specific T_2^* value that guarantees a good conductivity reconstruction. A relation between T_2^* and maximum possible current injection duration would give an insight if the proposed method is applicable or not at T_2^* values of human tissues.

2.4.5 Signal to Noise Ratio Considerations

An important criterion in the evaluation of MR imaging techniques is SNR. The ratio of the acquired MR signal power to the power of the noise presented in the imaging system gives a quantitative measure for the quality of the produced MR images. A theoretical estimation of the power of the signal acquired using the proposed method can be derived from (2.20). From this equation, it is clear that each signal replica is divided by a factor of four. This means that the power of each replica is reduced to one-sixteenth in comparison to a conventionally acquired signal. Defining the power of conventional MR signal as P_{conv}, and the power of each signal replica produced using the proposed method as $P_{replica}$, these powers can be related mathematically as

$$P_{replica} \approx (\frac{1}{4})^2 P_{conv} \tag{2.33}$$

However from SNR point of view, this loss in signal power is somehow compensated by the noise reduction happening during the low-pass filtering process of the signal replicas in k-space. Since noise power is directly related to the noise bandwidth, reducing signal bandwidth reduces noise power. Typically the bandwidth of the low-pass filter is set to be 33% of the width of the k-space, to avoid any possible aliasing from neighbor signal replicas. If this filter is a square low-pass filter, it would cover an area of one-ninth that of the signal k-space. Such a filter reduces noise power by a factor of nine, which implies that the SNR of a signal acquired using the proposed method can be related to that acquired conventionally as

$$SNR_{proposed} \approx \frac{9}{16} SNR_{conv} = 0.5625\, SNR_{conv} \tag{2.34}$$

Thus, the SNR is reduced to almost 56%. However, this can be treated as a lower bound, as SNR can be further improved by properly choosing the shape of the used low-pass filter, as well as the pulse sequence used after SPAMM preparation module. This loss can be even compensated by using short-term averaging (i.e., collecting four successive signal echoes in the same T_R), as SNR enhancement is proportionally related to the square root of the number of averaging.

2.5 Inverse Problem of MREIT

Recovering the distribution of electrical conductivity from measured magnetic flux density data is known as the inverse problem of MREIT. Reconstruction algorithms used for this inverse problem can be classified into two groups: J-based algorithms that require the knowledge of at least two $\overrightarrow{B}$ components as inputs for the algorithm [65], and B-based algorithms that need only one component of $\overrightarrow{B}$, typically B_z, as an input. The formers rely on first recovering the distribution of current density and then conductivity distribution, as described in [17]. While in B-based methods, conductivity is recovered without the need for current density data. Several B-based reconstruction methods have been developed up to today, as explained in [41, 45]. This study is conducted with SMM algorithm that utilizes the relation between the change in magnetic flux density in accordance to a change in conductivity [41]. In more detail, a perturbation in the conductivity σ of an object leads to a change in the density distribution of the injected current. As a consequence, magnetic flux density $\overrightarrow{B}$ changes. Defining the change in B_z and σ as ΔB_z and $\Delta\sigma$ respectively, these changes can be related as

$$\Delta B_z = \mathrm{S}\,\Delta\sigma \tag{2.35}$$

S represents the sensitivity matrix, from which the name of this reconstruction method came, and ΔB_z and $\Delta\sigma$ are the change vectors calculated as

$$\Delta B_z = B_z^{meas} - B_z^{init} \tag{2.36}$$

$$\Delta\sigma = \sigma^{unkown} - \sigma^{init} \tag{2.37}$$

Assuming conductivity image to have $N \times N$ dimensions, σ^{init} is the initial conductivity distribution, conventionally uniform, represented in a vector form of $N^2 \times 1$ dimensions. B_z^{init} is the corresponding magnetic flux data with similar dimensions, and B_z^{meas} is the measured B_z data after initial conductivity has been changed.

The sensitivity matrix S is calculated in a simulation environment using perturbations on an initial uniform conductivity distribution. Each column of S represents the resultant ΔB_z corresponding to a small change, approximately 0.01% of the initial value, in one element of the initial conductivity map σ^{init}. This matrix is calculated only once and then can be used for reconstructing any unknown conductivity. After calculating $\mathbf{S}$, (2.36) can be used to find ΔB_z, and then using (2.35) $\Delta\sigma$ can be obtained. Finally, by substituting of $\Delta\sigma$ in (2.37) the unknown conductivity map $\sigma^{unknown}$ can be reconstructed.

Conductivity information carried on magnetic flux density has a dependency on the pattern of the injected current. For instance, with a current being applied horizontally, conductivity variations along x-direction does not cause a change in current distribution and consequently the generated magnetic flux density [41] . Therefore, recognizing conductivity variations can be improved by utilizing multiple B_z measurements generated by different current injection patterns. Usually, two orthogonal current profiles, horizontal and vertical, are used for current injection. Each profile has its own sensitivity and thus two sensitivity matrices should be calculated separately. Defining the superscripts ^{H} and ^{V} as indicators referring to the horizontal and vertical current profiles respectively, measurements from horizontal and vertical current injections can be used to solve (2.35) as

$$\begin{bmatrix} \Delta B_z^H \\ \Delta B_z^V \end{bmatrix} = \begin{bmatrix} \mathbf{S}^H \\ \mathbf{S}^V \end{bmatrix} \quad \Delta\sigma \tag{2.38}$$

The new sensitivity matrix $\mathbf{S}^{All}$ produced by vertically concatenating the matrices $\mathbf{S}^H$ and $\mathbf{S}^V$ has the dimensions of $2N^2 \times N^2$, which is no more a square matrix and thus its inverse cannot be directly obtained. However, approximated solution for (2.38) with respect to $\Delta\sigma$ can be calculated using least square method by solving the following minimization problem

$$\widehat{\Delta\sigma} = \min_{\Delta\sigma \in \Psi^2} ||\mathbf{S}^{All}\Delta\sigma - \Delta B_z^{All}||_2^2 \tag{2.39}$$

where B_z^{All} refers to the vector obtained by vertically concatenating ΔB_z^H and ΔB_z^V vectors. Ψ refers to the range space of which the solution vector belongs to, and $||\ ||_2$ is the L2 norm. Produced sensitivity matrices $\mathbf{S}^{All}$ have been shown to have large condition numbers. For $N = 40$ and 80, the condition numbers were found to be 1168.8 and 3816×10^{17} respectively. These large condition numbers mean that the system given in (2.38) is ill-conditioned. Because of this problem as well as the noisy nature of the magnetic flux measurements, a regularization method is embedded in equation (2.39) as

$$\widehat{\Delta\sigma}(\lambda) = \min_{\Delta\sigma \in \Psi^2} ||\mathbf{S}^{All}\Delta\sigma - \Delta B_z^{All}||_2^2 + \lambda^2||L(\Delta\sigma - \Delta\sigma_0)||_2^2 \tag{2.40}$$

This regularization method is known as Tikhonov method, where λ is the parameter used for regularization and $\widehat{\Delta\sigma}(\lambda)$ is the corresponding solution [67]. $\Delta\sigma_0$ refers here to any prior knowledge about $\Delta\sigma$, while L is a constraint matrix used to emphasis or to damp the contribution of a specific region or a group of pixels. In this study, neither prior knowledge is assumed (i.e., $\Delta\sigma_0 = 0$), nor a constraint is used (i.e., L is set to be identity matrix).

The regularization parameter λ is used to control the contributions of the two terms in (2.40) into the error in the resultant solution $\widehat{\Delta\sigma}(\lambda)$. For instance, a very small λ makes the resultant error is mainly due to $||\mathbf{S}^{All}\Delta\sigma - \Delta B_z^{All}||_2^2$. While large λ emphasises the error resulting from $||L(\Delta\sigma - \Delta\sigma_0)||_2^2$. Optimal λ can be selected using the assist of several methods presented in the literature. In this work, λ is selected using L-curve method [68]. In this method, $||L(\Delta\sigma - \Delta\sigma_0)||_2^2$ is plotted against $||\mathbf{S}^{All}\Delta\sigma - \Delta B_z^{All}||_2^2$ at a wide range of λ values. The resultant curve has the shape of the letter L, from which the method got its name. The value of λ at the acute corner of the curve represents the optimal value of the regularization parameter.

To conclude SMM reconstruction, given an initial conductivity map σ^{init} the sensitivity matrix $\mathbf{S}^{All}$ is computed along with initial B_z distributions. Afterwards, ΔB_z^{All} is found by substituting experimental B_z measurements in (2.13). Then, equation (2.40) is solved for $\widehat{\Delta\sigma}$, and final conductivity is computed as $\widehat{\Delta\sigma} + \sigma^{init}$.

CHAPTER 3

SIMULATION AND EXPERIMENTAL SETUPS

Results presented in this study are obtained from measurements collected using simulation models as well as experiments. In this chapter, the methods and the tools used to produce these measurements are described in detail. First section gives information about numerical models and software used to produce simulated measurements. Simulation models required to generate B_z data are described in subsection 3.1.1. Then, the tool used to design and to simulate the proposed pulse sequence is introduced in subsection 3.1.2 along with the used imaging parameters.

In addition, the details about the objects designed for imaging experiments, known as phantoms, as well as the devices and the imaging parameters used during experiments are given in section 3.2. A brief description of the contents, the dimensions and the preparation of the experimental phantoms which are used in this study is given in subsection 3.2.1. Afterwards, the current source used to inject current pulses is described in subsection 3.2.2. The employed MR scanner to collect experimental data, and the software used to design the pulse sequences are introduced in subsection 3.2.3. Finally, pulse sequences parameters used during the imaging process are given in section 3.2.4.

3.1 Simulation Setup

Computer modeling, known as simulation, has been a useful tool to verify the applicability of concepts before realizing them in real world. Simulating the method introduced in this study goes through two steps. First, magnetic flux density distributions should be produced using a magnetic field simulator. Then, these data can be added into the main magnetic field equation of an MR pulse sequence simulator (described in subsection 3.1.2) to introduce the effect caused by current injection. Various software, models and imaging parameters used during these two steps are described briefly in the following two subsections.

3.1.1 $\mathrm{B_z}$ Data Simulation

Three simulation models are used in this study for different purposes. First, a model with uniform conductivity is needed to produce homogeneous B_z distribution. Two different B_z data are needed to be produced: with horizontal and with vertical current injection profiles. These homogeneous B_z data are used as a reference to recognize what a change could happen in B_z as a response to a change in conductivity. These data help also in predicting how experimental measurements would look like. In addition, these simulated data are needed during the reconstruction process of the SMM algorithm. For these purposes, the model illustrated in Figure 3.1 (a) is implemented using Finite Element (FE) software (COMSOL Multiphysics). The shape and the size of this model imitate the shape and the size of the phantom used in the experiments. This model has $8 \times 8 \times 8\, cm^3$ dimensions with electrodes of $2 \times 2 \times 2\, cm^3$ dimensions. Model conductivity and relative permeability are set to $0.5\, S/m$ and 1 respectively.

The second numerical model has the same dimensions of the first model, but with non-uniform conductivity distribution. The non-uniformity in conductivity is achieved by placing a rectangular prism of $1.3\, S/m$ conductivity at the center of the model, as shown in Figure 3.1 (b). The rectangular prism has a top face area of $2 \times 2\, cm^2$ and a height of $8\, cm$. Data generated using this model are useful for quantitatively evaluating the performance of the SMM reconstruction algorithm.

Another non-uniform model is implemented for evaluating the achievable resolution using the proposed pulse sequence. At the center of this model, a cylinder of $1.4\, S/m$ conductivity and $8\, cm$ height is placed, as illustrated in Figure 3.1 (c). Multiple B_z data are produced using this model with different cylinder diameter: 2, 4, 6, 8, 10 and 12 mm. Different shape and conductivity value are used for the non-uniformity object in this model to test the reconstruction algorithm at a variety of conditions.

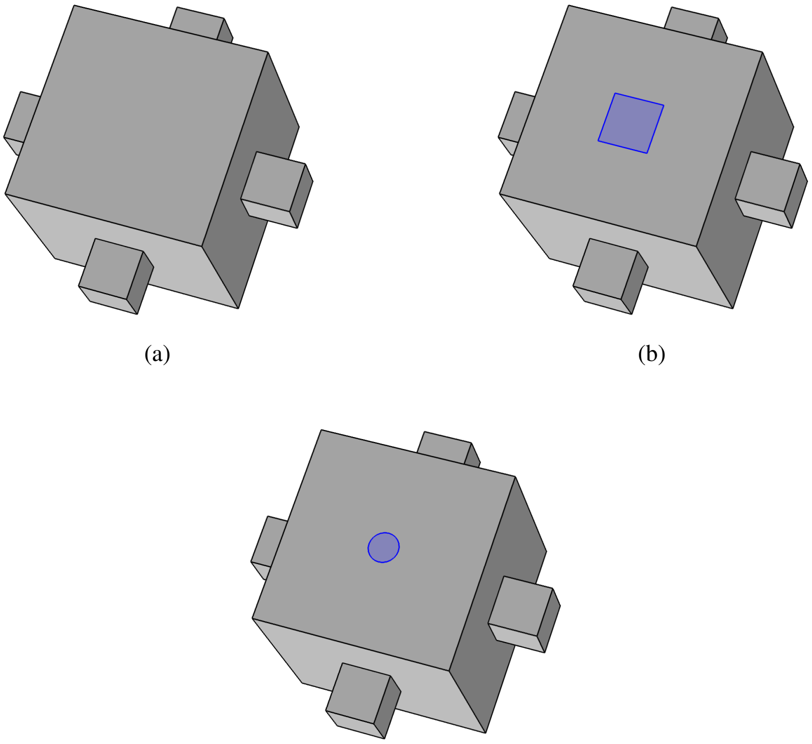

(a) (b)

(c)

Figure 3.1: Numerical models: (a) Uniform Model, (b) Non-uniform Model 1, and (c) Non-uniform Model 2.

Details about the mesh elements of each model are given in Table 3.1. Extra fine meshing was used for the third model to ensure producing much precise B_z data, such that even the conductivity change caused by an object of 2 mm diameter is recognized. Using each of these numerical models, two B_z data are produced: using horizontal and vertical current injections. These magnetic flux data are referred to as B_z^H and B_z^V, respectively.

Table 3.1: Meshing details of the used numerical models.

Parameter	Uniform Model	Non-uniform Model 1	Non-uniform Model 2
Vertex elements	40	48	48
Edge elements	468	584	1584
Surface elements	6956	8088	20878
3D elements	123540	121824	393413

3.1.2 Pulse Sequence Simulation

Before experimentally realizing the proposed pulse sequence, a simulation verification was performed using MRiLab software on MATLAB environment. MRiLab is a free-licensed open source software, running on MATLAB, that provides the ability to numerically simulate MR signal formation, acquisition, and reconstruction using interactive Graphical User Interface (GUI) [69]. MRiLab includes a toolbox for designing numerical phantoms to be used for imaging simulation. This toolbox provides the ability to specify the shape and the size of the numerical phantom, and to assign the values of the proton density, T_1, T_2 and T_2^* for each voxel in the phantom. In MRiLab, the shape and the size of the used numerical phantom are designed to match those of the COMSOL model, such that the produced B_z data using COMSOL is registered without errors on the MRiLab phantom. However, for memory usage and run time considerations the depth of the MRiLab phantom is reduced to 2 cm, which is the side length of the recessed electrodes. In addition, uniform values for proton density, T_1, T_2 and T_2^* were used in this numerical phantom: 1, 1 s, 95 ms, and 46.6 ms respectively. These relaxation times were set to the average of those measured in human brain tissues at 3T, given in [70].

Another toolbox in MRiLab is dedicated for designing pulse sequences, giving the ability to construct a pulse sequence using prepared RF and gradient pulses available in the toolbox library, or using customized pulses specified in a MATLAB file. Besides, this toolbox gives the chance to modify the magnetization data at any specific instant using external MATLAB code file. This facility is used in this part of the study to incorporate the effect of injected current into the produced MRI image. This is done by externally adding the simulated B_z data to the signal equation of MRiLab for a predefined time duration, according to (2.11). This time duration reflects the duration of the injected current pulses, and can be controlled using external flags.

Figure 3.2 illustrates the diagram of the proposed pulse sequence designed using MRiLab. The first three lines in the diagram, namely: rfAmp, rfPhase and rfFreq, describe the RF pulses used in the pulse sequence. These lines illustrate the amplitude, the phase and the frequency of the RF pulses, respectively. Next three lines are named GzSS, GyPE and GxR respectively. These lines illustrate the shape, the

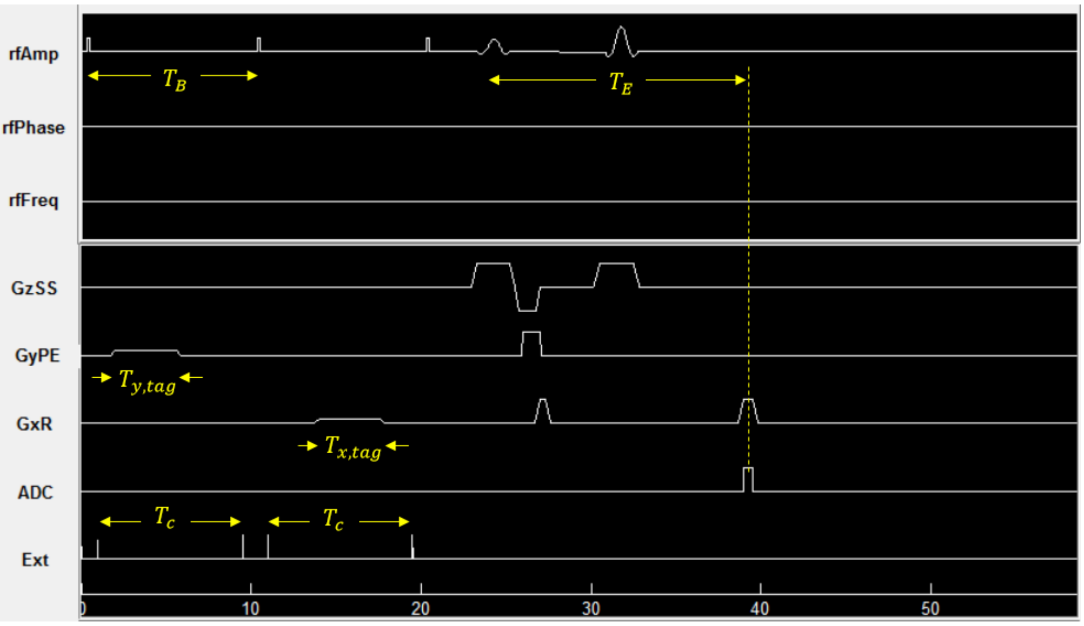

Figure 3.2: A diagram of the proposed pulse sequence implemented using MRiLab. The unit of the time line at the bottom of the diagram is $[ms]$.

strength and the duration of each gradient pulse applied in the slice-selection, the phase-encoding, and the frequency-encoding gradients, respectively. The next line is named ADC, and it is used to illustrate the time in which the k-space signal is collected. While in the last line, named Ext, flags are used to indicate the time instants in which external codes (if any) are executed.

As shown in Figure 3.2, the DCI-MREIT pulse sequence is implemented on a SE-based pulse sequence. SPAMM module, consisting of three 90° hard RF pulses and two gradient pulses, is inserted before the SE pulse sequence. The time gap between each successive hard pulses is T_B. B_z^H data is added to the magnetization phase component for a duration of T_c between the first and the second hard RF pulses using external MATLAB code. This duration is marked in the given diagram using the first pair of flags in the Ext line. Similarly, B_z^V data is added for a duration of T_c between the second and the third hard RF pulses. The pulse sequence parameters used in MRiLab are summarized in Table 3.2. N_{Ph} and N_{Fr} in Table 3.2 refer to the number of the collected phase-encoding and frequency-encoding lines respectively. While $N_{Ph,w}$ refers to the number of the phase-encoding lines covered by the filter window used to extract signal replicas from the k-space signal. MRiLab is also able to add

Table 3.2: DCI-MREIT pulse sequence parameters used in MRiLab.

Parameter	Value
Slice thickness $[mm]$	5
FOV $[mm]$	120
N_{Ph}	120
$N_{Ph,w}$	40
N_{Fr}	120
Averaging number (NEX)	4
T_E $[ms]$	15
T_R $[ms]$	500
$G_{x,tag} = G_{y,tag}$ $[mT/m]$	2
$T_{x,tag} = T_{y,tag}$ $[ms]$	3.6
T_B $[ms]$	10
T_c $[ms]$	9

zero-mean Gaussian noise with specific standard deviation to the resultant k-space data. In this study, the standard deviation of the added noise is set to be 11.78.

To evaluate the spatial resolution of the proposed pulse sequence in comparison with the conventional MREIT pulse sequence, the latter is also implemented in MRiLab. As shown in the diagram given in Figure 3.3, B_z data is added to the MRiLab in the time gap between the 90° and the 180° RF pulses for a duration of $T_c/2$, and then with a reversed sign for another $T_c/2$ duration after the 180 RF pulse. This is done individually for each of B_z^H and B_z^V respectively. The simulation is repeated for each B_z^H and B_z^V obtained using the second non-uniform model with different cylinder diameters, as mentioned before. The simulation is also repeated using the proposed pulse sequence for each B_z data set (B_z^H and B_z^V) obtained in correspond to different cylinder diameters in the second non-uniform model. Parameters of the pulse sequences used in the simulations of this part are given in Table 3.3.

3.2 Experimental Setup

A standard MREIT experiment requires phantoms to be imaged, a current source to inject current pulses, an MR scanner, and designing pulse sequences that are compatible with the MR scanner being used. These elements are described in the following subsections.

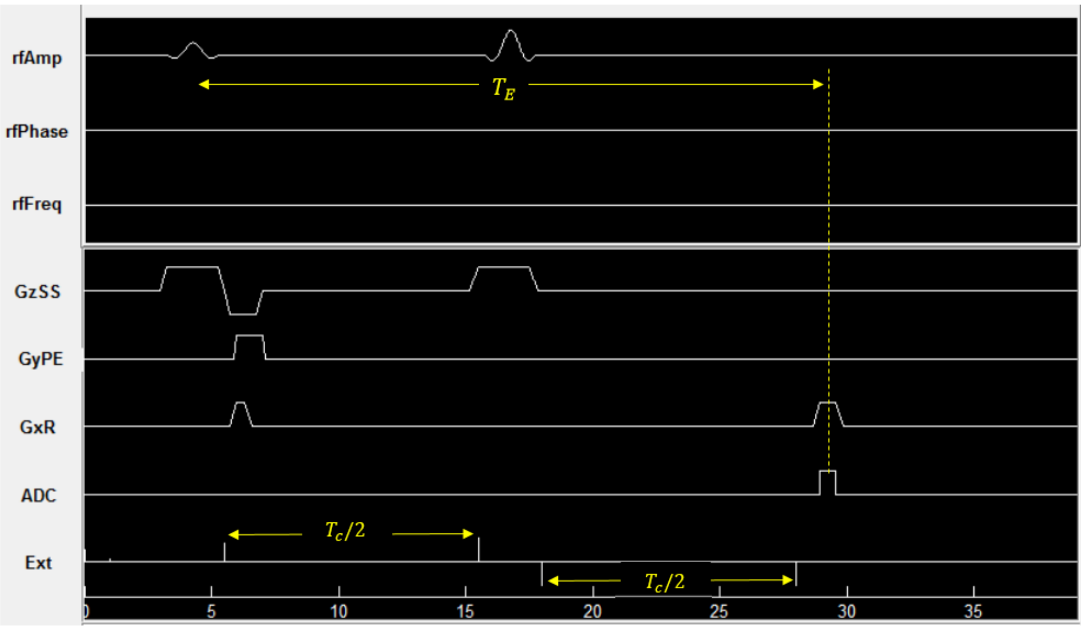

Figure 3.3: A diagram of the conventional MREIT pulse sequence implemented using MRiLab. The unit of the time line at the bottom of the diagram is $[ms]$.

Table 3.3: Pulse sequences parameters used in MRiLab to collect the data used for evaluating the spatial resolution.

Parameter	Standard SE	Proposed
N_{Ph}	60	-
$N_{Ph,w}$	-	20
$G_{x,tag} = G_{y,tag}\ [mT/m]$	-	1
$T_{x,tag} = T_{y,tag}\ [ms]$	-	3.6
N_{Fr}	60	
Slice thickness $[mm]$	5	
FOV $[mm]$	120	
Averaging number (NEX)	4	
$T_E\ [ms]$	25	
$T_R\ [ms]$	500	
$T_c\ [ms]$	20	

3.2.1 Experimental Phantoms

In this study, two physical phantoms were prepared for experiments to illustrate the cases of uniform and non-uniform conductivity distributions. The container of both phantoms is depicted in Figure 3.4. Its cavity has the dimensions of $8 \times 8 \times 8\,cm^3$, and its walls made from Plexiglas; an MR non-active material. Four Copper electrodes are recessed on rectangular-shaped cavities of $2 \times 2 \times 3\,cm^3$ size extruded from the center of each interior face of the phantom container. These electrodes are connected using coaxial cables to the current source that will be described in subsection 3.2.2.

The first phantom shown in Figure 3.5 was filled with saline solution having a conductivity value of 0.5 S/m. The saline solution is prepared from mixing Pure Water: NaCl: CuSO4 with the ratios 100 ml: 0.25 g: 0.1 g respectively. The conductivity of the prepared solution was measured using Cond 3310 conductivity meter (WTW, Germany). This phantom is used for measuring uniform B_z data as well as for acquiring magnitude images needed for SNR, T_2^* and minimum measurable current calculations.

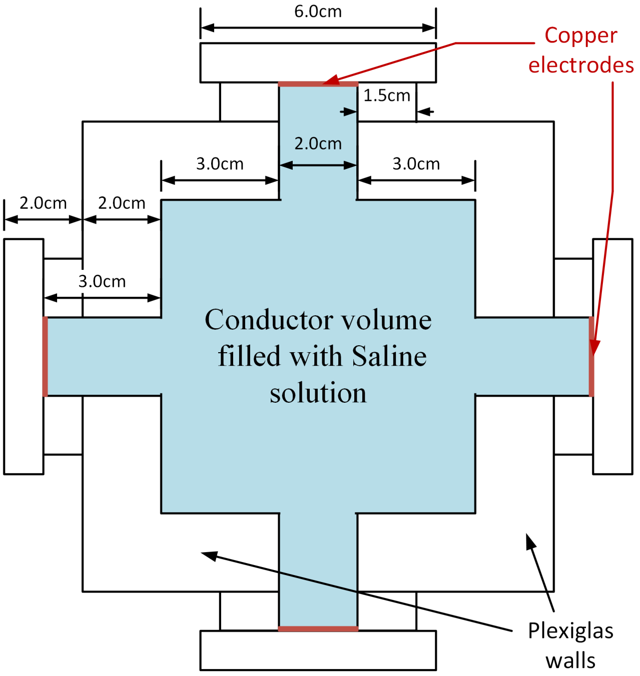

Figure 3.4: 2D sketch of the used experimental phantom at the plane passing through the center of all the electrodes.

The second phantom shown in Figure 3.6 was prepared to demonstrate a non-uniform conductivity distribution that can be imaged using the proposed pulse sequence.

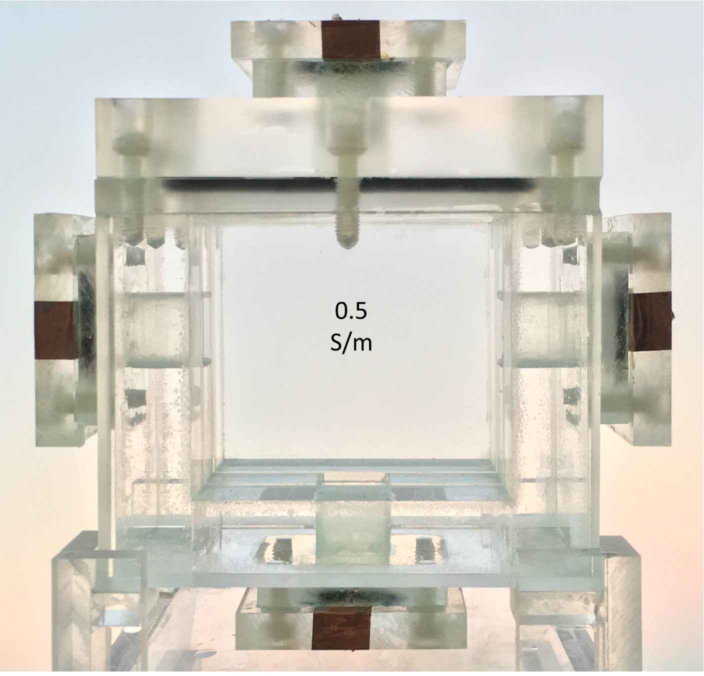

Figure 3.5: Phantom 1 has a uniform conductivity of $0.5\,S/m$.

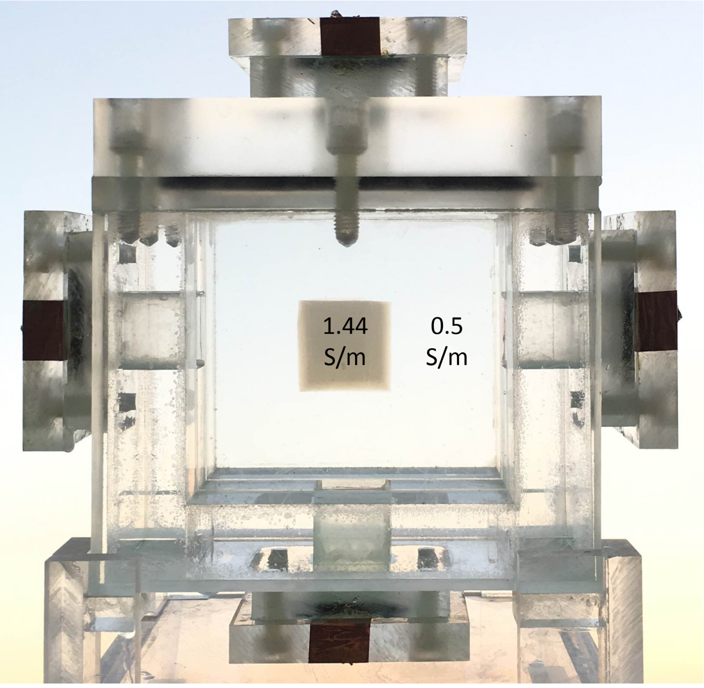

Figure 3.6: Phantom 2: An object with $\sigma = 1.44\,S/m$ is placed at the center of the phantom to produce a variation in conductivity distribution.

The non-uniformity was made by placing a square-shaped object that has a different conductivity value at the center of the phantom container, as illustrated in Figure 3.6. The dimensions of this object are $2.5 \times 2.5 \times 2\,cm^3$. In order to prevent dissolving the object inside the background solution it was solidified by adding agar material to its mixture with a ratio of 1 g for each 100 ml of pure water. Conductivity values in this phantom were varied by changing the ratio of NaCl in the mixtures, as described in Table 3.4. To prepare the Agarose object, the mixture should be heated for a couple of minutes while mixing. When agar is completely dissolved, solution becomes transparent, and at that moment heating has to be stopped. This process takes less than 30 minutes. The prepared solution is then poured into a mold and it takes half an hour for the mixture to become solid.

Table 3.4: Conductivity values and NaCl ratios in Phantom 2.

	Background	Object
σ [S/m]	0.5	1.44
NaCl [g] for 100 ml water	0.25	0.75

3.2.2 Current Source

During experiments, current was injected using the current source designed by Eroğlu [71]. This current source is programmable, providing the ability to adjust the amplitude and the duration of the current pulses to be injected. This device has four current injection channels, of which one or more of these channels can be selected for current injection. However, in this study current is needed to be switched between two channels automatically and immediately after the execution of the second hard RF pulse in the proposed pulse sequence. Therefore, an external switching circuit was designed and implemented such that it is capable of switching the injected current between two separated channels in a response to a command from the current source Micro-Controller Unit (MCU).

A schematic diagram for this circuit is shown in Figure 3.7. It is basically composed of four parallel blocks, each of them contains an operation amplifier in voltage follower configuration and a Solid State Relay (SSR). Blocks of each pair (either upper

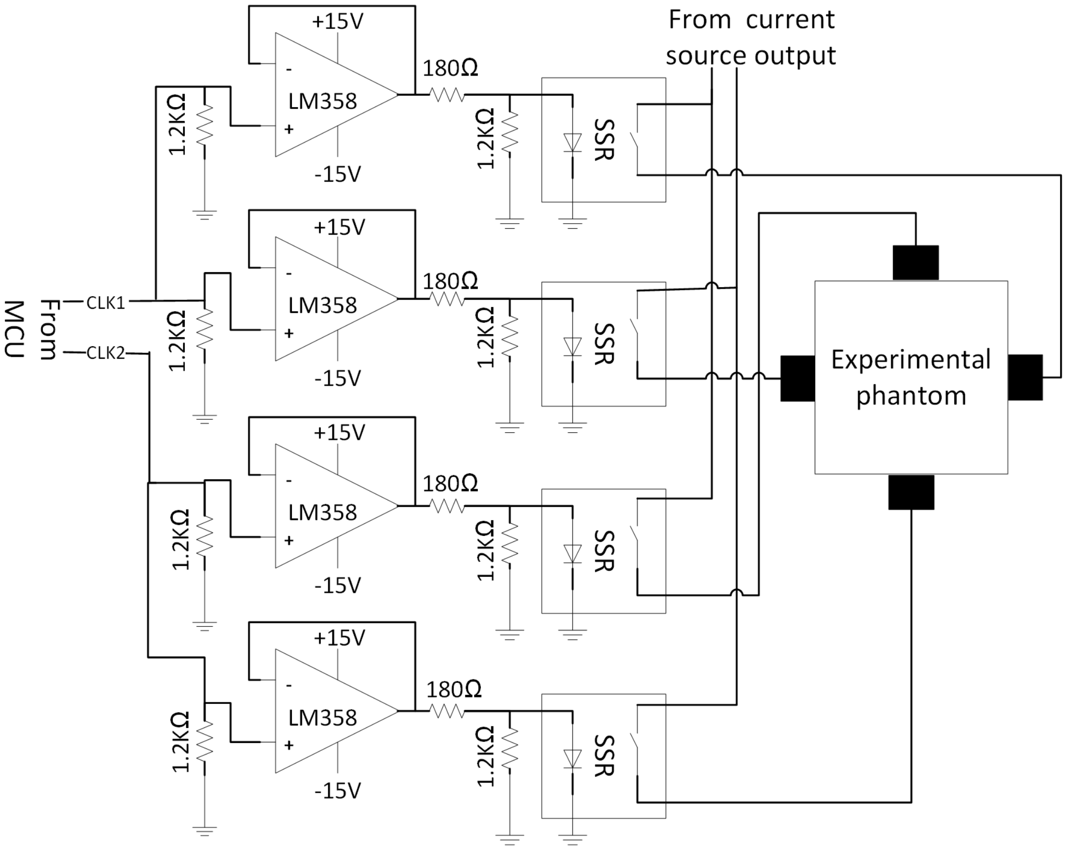

Figure 3.7: Schematic diagram of external current switching circuit.

or lower pair) are controlled by the same MCU signal to make a closed loop for the injected current. In this circuit, photo-voltaic relays PVX6012 are used to isolate the MCU from high voltages supplied to SSRs. PVX6012 relays have $1.2\ V$ on-state voltage drop and a maximum driving current of $25\ mA$ [72]. Switching speed of this relay is directly proportional to the amplitude of the driving current. Therefore to ensure fast operation of the relay, a sufficiently large controlling current I_{SSR} is derived by the chosen values of resistors. Since the voltage coming from MCU is $5\ V$, a current of $20\ mA$ can be obtained using resistors values of $180\ \Omega$ and $1.2\ K\Omega$ as follows:

$$I_{SSR} = \frac{5V - 1.2V}{180\Omega} - \frac{1.2V}{1.2K\Omega} = 20mA \tag{3.1}$$

3.2.3 MRI Scanner and Pulse Sequence Design

Experimental data presented in this thesis are acquired using 3T MR scanner MAGNETOM Trio (Siemens, Germany) located in National Magnetic Resonance Research Center of Bilkent University. Data acquisition was done using the single-channel built-in whole body RF coil of the scanner. Pulse sequences used to obtain data are designed using IDEA software (Siemens, Germany). Two versions of the proposed pulse sequence are designed: SE-based and GE-based. In the next chapters, These two pulse sequences are referred to as SE DCI-MREIT and GE DCI-MREIT respectively.

3.2.4 Imaging Parameters

During this study, several MR data were collected for different purposes. The first group of data was acquired for performing SNR analysis and determining minimum current level that can be measured. This group includes 18 MR images obtained using three pulse sequences: Conventional SE MREIT, SE DCI-MREIT, and GE DCI-MREIT. Using each of these pulse sequences, two similar MR images were obtained with different number of averaging (NEX): 1, 4 and 8. Imaging parameters used for collecting these data are listed in Table 3.5.

The second group of data contains four standard GE images of four different echo times, collected to estimate T_2^* relaxation time of the phantom being used in the experiments at 3T. Imaging parameters used in this experiment are given in Table 3.6. Long T_R and small flip angle were used to ensure full longitudinal recovery of magnetization.

The third group of data was collected to obtain an upper limit for the duration of the injected current that can be used with the proposed pulse sequence without significant loss in the acquired signal. In this group, there are eight images obtained using SE DCI-MREIT, with the parameters listed in Table 3.7. These eight images composed of four sets obtained with four different T_c durations. Each set contains two images obtained with positive and negative current respectively.

Table 3.5: Imaging parameters used in collecting the data used for SNR and minimum measurable current calculations.

Parameter	Conventional SE	SE DCI-MREIT	GE DCI-MREIT
T_E $[ms]$	22	15	5
$G_{x,tag} = G_{y,tag}$ $[mT/m]$	-	3	
$T_{x,tag} = T_{y,tag}$ $[ms]$	-	1	
T_B $[ms]$	-	10	
FOV $[mm]$	256		
$N_{Ph} = N_{Fr}$	128		
NEX	1, 4 and 8		
Slice thickness $[mm]$	5		
T_R $[ms]$	500		

Table 3.6: T_2^* measurement imaging parameters.

Parameter name	Value
T_E $[ms]$	5, 10, 20 and 50
T_R $[ms]$	5000
Flip angle $[deg]$	15
NEX	2
N_{Ph}	64
N_{Fr}	64
FOV $[mm]$	128
Slice thickness $[mm]$	5

Table 3.7: Imaging parameters used in estimating maximum usable T_c.

Parameter name	Value
T_E $[ms]$	15
T_R $[ms]$	500
NEX	2
N_{Ph}	256
N_{Fr}	256
FOV $[ms]$	256
Slice thickness $[mm]$	5
$G_{x,tag} = G_{y,tag}$ $[mT/m]$	6
$T_{x,tag} = T_{y,tag}$ $[ms]$	1
$I_H = I_V$ $[mA]$	20
T_c $[ms]$	13, 15, 17 and 19
T_B $[ms]$	14, 16, 18 and 20

CHAPTER 4

RESULTS AND COMPARISONS

Simulation and experimental measurements of this study, along with obtained results from these measurements are shown in this chapter. The first section, 4.1, contains all results belonging to computer models and simulated pulse sequence, including simulated and recovered magnetic flux density data, reconstructed conductivity and error measurements. While results obtained from experiments are presented in section 4.2, including extracted magnetic flux density data, conductivity distributions, as well as SNR, minimum measurable current, and T_2^* measurements.

4.1 Simulation Results

As described before, two numerical models are used to illustrate the uniform and the non-uniform conductivity distributions. The results of the uniform model are given in subsection 4.1.1, while those of the non-uniform model are given in subsection 4.1.2.

4.1.1 Uniform Model

The numerical model illustrated in Figure 3.1(a) has a uniform conductivity of 0.5 S/m everywhere. This model is used to produce two B_z data, B_z^H and B_z^V, in corresponding to two current injection profiles: horizontal and vertical, respectively. For the first current profile, a current of 20 mA is applied between the left and the right electrodes in the horizontal direction. While for the vertical profile, current is injected using the top and the bottom electrodes. The z-component of the generated magnetic flux density for both current profiles are shown in Figure 4.1. As it is seen, obtained magnetic flux density distributions are symmetric but with opposite sign around the direction of injected current. For instance in B_z^H, values in the upper half of the distribution have the same pattern of those in the lower half but with reverse sign. This is due to the rotation of the generated magnetic flux around the direction of current, in accordance with the right-hand rule. Also, with 20 mA current the obtainable magnetic flux density is in μT level varying within a range of almost 0.5 μT. These B_z data are then included in the signal equation of the pulse sequence simulator as described in section 3.1.2.

The proposed pulse sequence is simulated in MRiLab with the imaging parameters given in Table 3.2, and the output of the simulator is the k-space data shown in Figure 4.2. In section 2.3.1, it is stated that another data acquisition is needed as a reference, without current injection or with opposite current polarity, to eliminate unwanted phase components. In this study, the reference data is obtained using negative current injection. However, through this chapter only the data obtained using positive current are shown, because those obtained using negative current are similar and there is no significance for showing them. Since the aim of this study is reducing the scan time in MREIT, the needed time for measurement has to be stated quantitatively. However, the time spent by the MRiLab simulator to generate k-space data depends mainly on allocated computational power. Therefore, the effective scan time needed to collect a k-space signal using any pulse sequence is used here for comparisons. This time is

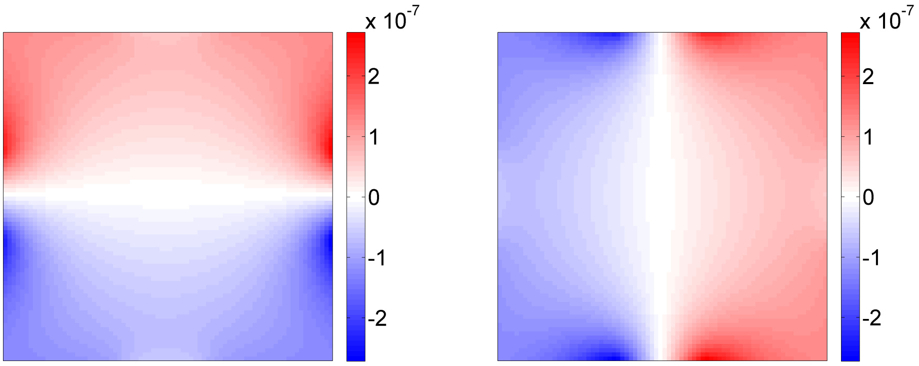

(a)

(b)

Figure 4.1: Uniform model results: (a) B_z^H, and (b) B_z^V generated by injecting current horizontally and vertically respectively. Shown data are given in unit of [T].

calculated as:

$$T_{S,Conv} = 4\,T_R\,N_{Ph}\,NEX \tag{4.1}$$

A factor of 2 is included in (4.1) to account the time needed for the reference acquisition with negative current. Another factor of 2 is included to account for the time needed to collect two data sets with two current profiles. However, this factor is omitted in the calculation of the scan time of the proposed pulse sequence, because the two profiles are applied in the same T_R.

$$T_{S,Prop} = 2\,T_R\,N_{Ph,w}\,NEX \tag{4.2}$$

Using the imaging parameters given in Table 3.2, $T_{S,Conv}$ and $T_{S,Prop}$ are found to be 16 minutes and 2.6 minutes respectively. Clearly, the time needed for collecting data using the proposed pulse sequence is six times shorter.

Figure 4.2 shows the expected four signal replicas centered near the corners of the k-space. It is noticeable that signal replicas along the secondary diagonal (i.e., the top right and the bottom left replicas) are not showing a T_2^*-related phase dispersion as described in section 2.4.4. This is because MRiLab simulator expresses T_2^* effect as an exponential decay that affects only the magnitude of MR data but not the phase. This approximation does not fully simulate the physical mechanism of T_2^* relaxation. Another issue about Figure 4.2 is the presence of additional small signals in between each of the signal replica pairs. These signals arise from the remnant unspoiled magnetization components at the end of the SPAMM preparation module. These unwanted signals can be eliminated by filtering them in spatial frequency domain, as it is done in this study.

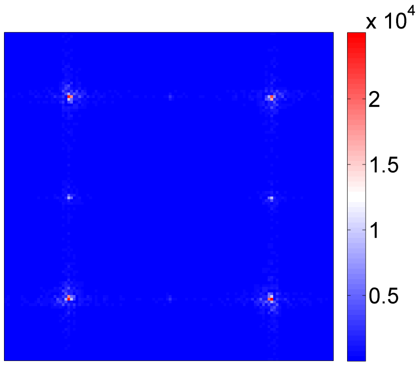

Figure 4.2: The magnitude of the k-space data obtained using MRiLab.

Recovering magnetic flux data can be done either from the top or from the bottom pair of signal replicas. Here, the bottom pair of replicas are used for this purpose. Each of the left and the right replicas has to be filtered using a LPF, shifted to the center, and transformed into spatial domain. Afterwards, undesired phase components are eliminated by taking the difference between the phase images of signal replicas obtained with positive and negative current injections.

The resultant phases of the two images obtained from the left and the right replicas are shown in Figure 4.3. Comparing the patterns of these phases with those in Figure 4.1, indicates that these phase data are neither due to the horizontal nor the vertical current profiles. This is expected, because each of these phase images are composed of the data of the both current profiles. In more detail, ϕ_{left} is the sum of the phases due to both horizontal and vertical currents, and ϕ_{right} is their difference, as expressed in (2.21) and (2.22) respectively. Current related phases, ϕ_H and ϕ_V, are then recovered using equations (2.23) and (2.24). These phase images are illustrated in Figure 4.4, which have similar patterns to those in Figure 4.1. These results prove the concept behind the pulse sequence introduced in this thesis and support the realizability of acquiring two independent B_z data in one acquisition.

In MREIT, obtained phase data are not always in the range of [-π, +π], and those data values out of this range are wrapped down into the same range by the fact of phase circularity. These wrapped values appear as sharp transitions in the phase data

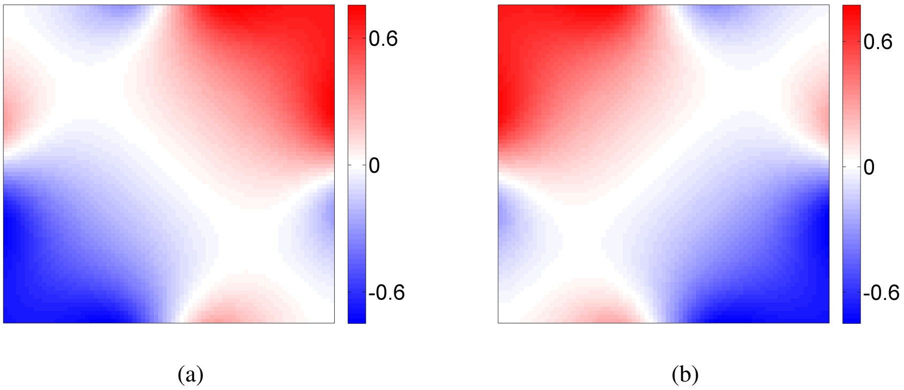

Figure 4.3: Uniform model results: (a) ϕ_{left} and (b) ϕ_{right} obtained form the left and the right replicas respectively. The unit of the shown phase data is radian (rad).

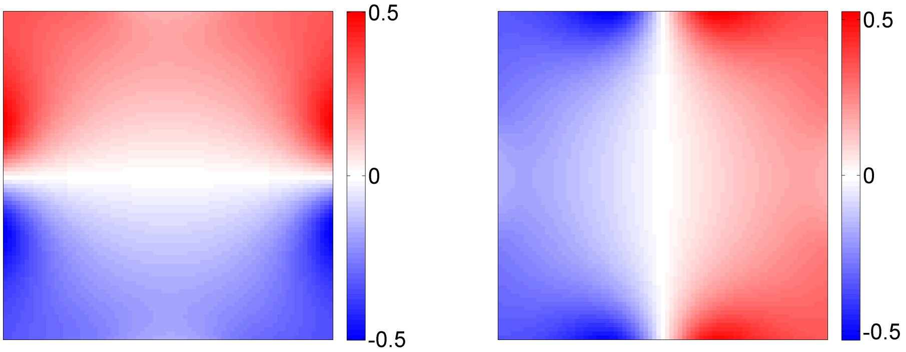

(a) (b)

Figure 4.4: Uniform model results: (a) ϕ_H and (b) ϕ_V introduced by the horizontal and the vertical current injections respectively, shown in unit of [rad].

(i.e., an abrupt change from -π to π or vice versa), which are not presented in the actual magnetic flux data. Therefore, these wraps have to be removed before any further processing of acquired phase data. To solve this issue, several unwrapping algorithms have been developed and used in many studies [73]. In this work, the algorithm developed by Spottiswood in [74] is used for unwrapping phase data. This method is named Phase Quality Guided algorithm, in which the variance of a phase image derivatives is used as a quality map. In this algorithm, priority is given to the phase pixels of highest quality, meaning that during unwrapping process regions of higher quality are unwrapped first, and those of worse quality are left to the end after most of the phase pixels are already unwrapped.

4.1.2 Non-uniform Model

Using the model shown in Figure 3.1(b) another set of B_z data (i.e., B_z^H and B_z^V) was simulated. The conductivity of this model is shown in Figure 4.5, which is not uniform as described before. Produced B_z^H and B_z^V using this model are shown in Figure 4.6. By comparing these B_z data with those obtained using the uniform model, the differences can be observed around the location of the square object at the center of the model. Changes in the density of B_z^H are observed at the positions of the horizontal edges of the square object, while changes in B_z^V are seen at the locations of the vertical edges. This implies that recognizing conductivity variation depends on

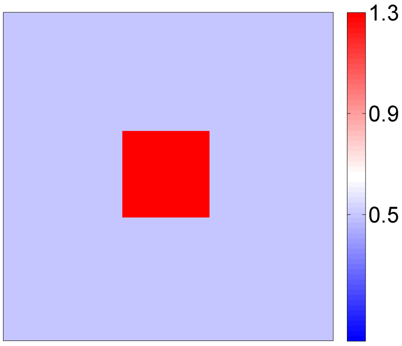

Figure 4.5: Conductivity distribution [S/m] inside the non-uniform model.

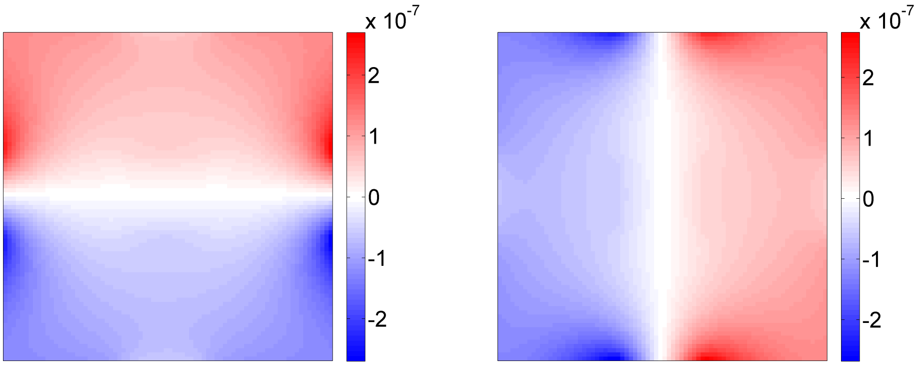

(a)

(b)

Figure 4.6: Non-uniform model results: (a) B_z^H and (b) B_z^V obtained using the non-uniform model. Shown data are given in unit of [T].

the direction of the injected current. Therefore, obtaining more B_z data using more current injection patterns captures more information about the unknown conductivity distribution, and thus improves the quality of the reconstructed conductivity.

These B_z data were added to the pulse sequence simulator as explained in the previous subsection, and the corresponding k-space signal was generated by the pulse sequence simulator. The bottom left and the bottom right replicas of this k-space signal were filtered and transformed to the spatial domain to extract their phases. These phases are used to recover B_z^H and B_z^V that are required for conductivity reconstruction.

As discussed in subsection 2.4.3, the selection of the filter shape affects the quality of recovered magnetic flux and conductivity distributions. Filters with sharp edges introduce undesired distortions in the resultant phase images because of their oscillating spatial response. This can be avoided by using a LPF of relaxed edges. For illustration, two 2D low pass filters are used in extracting the left and the right replicas: Square and Gaussian. The equations that describe these two filters are given in (2.25) and (2.26) respectively. 3D visualizations of these filters with $k_{off} = 23$ and $\varrho = 20$ are shown in Figure 4.7 (a and b). The values of k_{off} and ϱ are chosen to set the width of the filter window to 33% of the k-space width, according to (2.28) and (2.29). Employing these two filters in the procedure of extracting ϕ_H and ϕ_V gives the results shown in Figure 4.7 (c -f).

The results in the left column of Figure 4.7 are corresponding to the case where H_{square} filter was employed, while those in the right column are corresponding to H_{gauss} filter. B_z^H and B_z^V shown in Figure 4.7 are obtained from ϕ_H and ϕ_V respectively by using equation (2.13). Conductivity images shown in Figure 4.8 (a and b) are reconstructed using the SMM algorithm described in section 2.5 with $N = 40$. These results show that the usage of an LPF with sharp edges introduces background oscillating artifacts that influence the reconstructed conductivity. These artifacts are not appearing in the data processed using H_{gauss}.Thus, better magnetic flux data and better conductivity map are obtained. The quality of the recovered conductivity can be evaluated quantitatively using statistical measures. This will be discussed in the next subsection.

4.1.3 Performance Evaluation of Conductivity Reconstruction

A widely used measure to evaluate reconstruction algorithms is the Mean Square Error (MSE) expressed as:

$$MSE = \sqrt{\frac{1}{N_i N_j} \sum_{i=1}^{N_i} \sum_{j=1}^{N_j} \frac{(\sigma_T(i,j) - \sigma_R(i,j))^2}{\sigma_T^2(i,j)}} \times 100\% \tag{4.3}$$

where $\sigma_T(i,j)$ and $\sigma_R(i,j)$ are the true and the reconstructed conductivity values respectively of the pixel located in the i^{th} row and the j^{th} column [65]. N_i and N_j are the number of rows and columns in the conductivity image, respectively. This formula can be applied to the whole conductivity image to find a global value of MSE, and for individual conductivity levels (i.e., the center object and the background regions of the non-uniform phantom) separately to find local values of MSE.

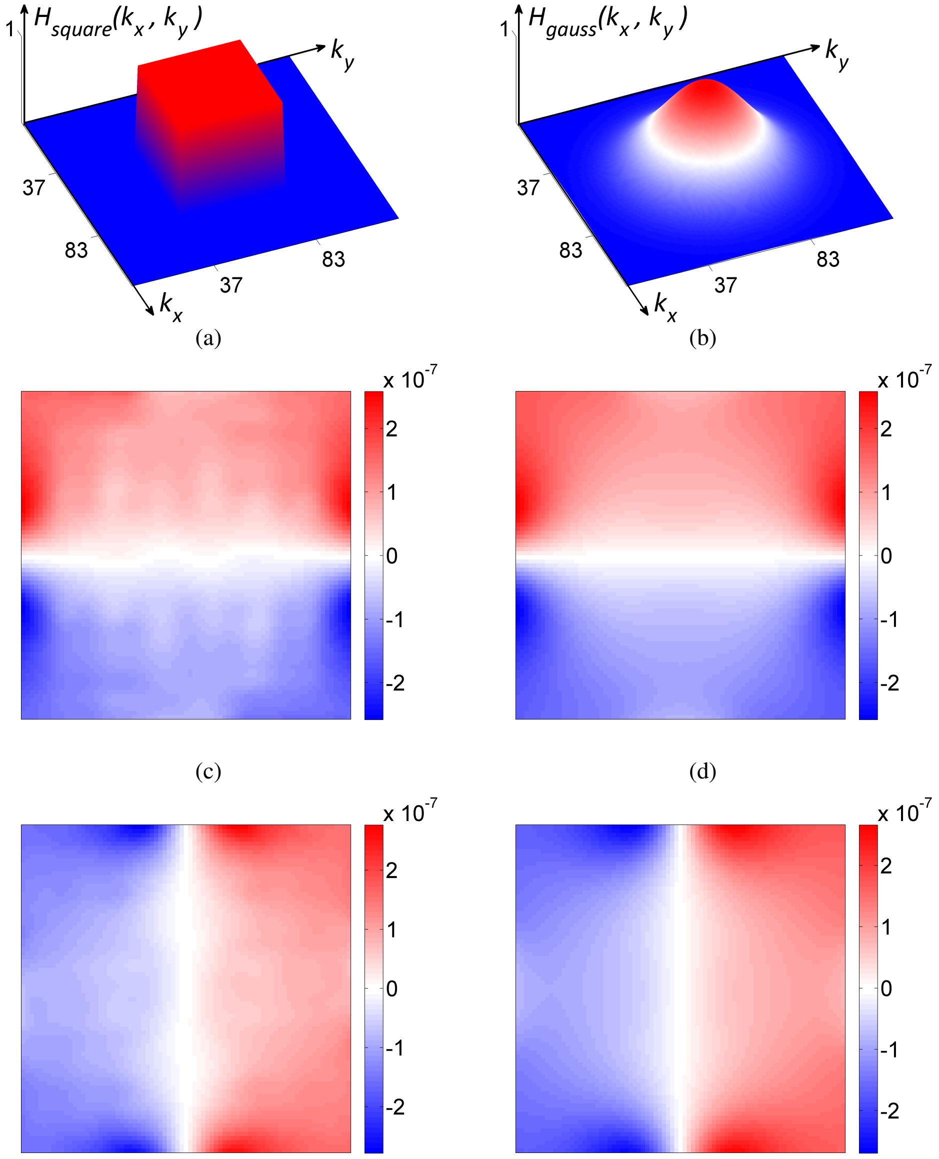

(a) (b)

(c) (d)

(e) (f)

Figure 4.7: Non-uniform model results: 3D view of spatial frequency low pass filters (a) Square filter H_{square}, and (b) Gaussian filter H_{gauss}. Recovered (c) B_z^H and (e) B_z^V using H_{square}. Recovered (d) B_z^H and (f) B_z^V using H_{gauss}. The unit of the shown magnetic flux density data is [T].

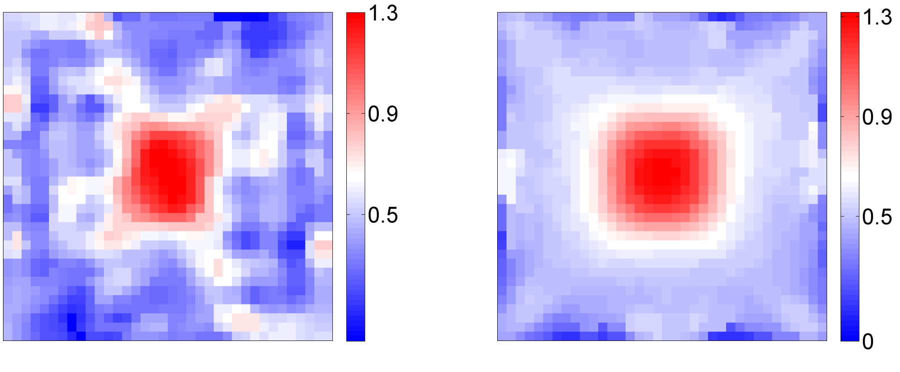

(a)

(b)

Figure 4.8: Non-uniform model results: Reconstructed (a) σ_{square} and (b) σ_{gauss} from data filtered with H_{square} and H_{gauss} respectively. The unit is [S/m].

Beside the reconstructed conductivities obtained from the data produced using MRiLab and shown in Figure 4.8(a and b), conductivity map is also reconstructed directly from simulated B_z data. This conductivity image is shown in Figure 4.9 and it has a better perceptual quality as it is recovered directly from the simulated B_z data and thus not suffering from the artifacts or errors related to MRiLab simulation and filtering process. MSE is calculated for each of these three conductivity images and the obtained results are given in Table 4.1.

In Table 4.1, σ_{square} and σ_{gauss} are used to refer to the reconstructed conductivities shown in Figure 4.8(a) and Figure 4.8(b) respectively. While σ_{direct} is the conductivity image shown in Figure 4.9. MSE_{obj} is the error calculated in the area of the center object whose true conductivity is 1.3 S/m, while MSE_{bg} is calculated in the remaining background area in which the true conductivity value is 0.5 S/m. Error calculated over the whole area is given as MSE_{global}. In all MSE calculations given in Table 4.1, the conductivity image shown in Figure 4.5 is used as the true conductivity, σ_T. Results given in Table 4.1 indicate that minimum MSE is observed in σ_{direct}. This is expected because σ_{direct} is reconstructed directly from the simulated B_z data without the effects of the noise, the pulse sequence simulator, and the frequency filtering process. MSE values of σ_{gauss} are also lower than those of σ_{square} due to the effect of the used filter shape. The amount of error in σ_{square} is larger in the background because of the undesired oscillations propagated from the B_z data.

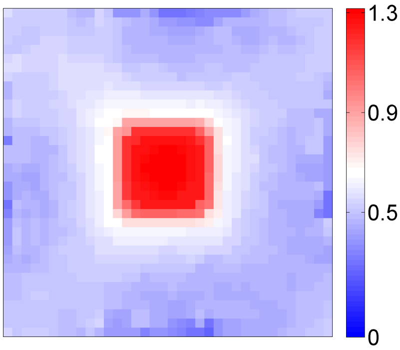

Figure 4.9: $\sigma_{direct}[S/m]$ recovered directly from simulated B_z data.

Table 4.1: MSE [%] in reconstructed conductivity images from simulated data.

	σ_{direct}	σ_{square}	σ_{gauss}
MSE_{obj}	9.15	13.15	12.87
MSE_{bg}	14.93	24.96	20.94
MSE_{global}	14.60	24.32	20.48

4.1.4 Evaluation of Spatial Resolution

Filtering is a necessary step to individually extract the signal replicas from the k-space. This however impacts the spatial resolution of the recovered conductivity images as a consequence of the inverse proportional relation between the signal bandwidth and the spatial resolution. In this subsection, the obtainable resolution using the proposed pulse sequence is investigated and compared to that of the standard MREIT pulse sequence. In this part, a series of simulations was performed using the non-uniform model with single object but with different values for the object diameter, as described in subsection 3.1.2. B_z data obtained using these simulations are added individually to MRiLab. Using MRiLab, k-space signals are produced by the proposed pulse sequence and the standard MREIT pulse sequence with the imaging parameters listed in Table 3.3. Using these parameters, the needed scan times for these two pulse sequences are found to be $T_{S,Conv}$= 8 minutes and $T_{S,Prop}$= 1.3 minutes. Conductivity images are then reconstructed using the B_z data sets extracted from these k-space data as described before. These conductivity images are shown in Figure 4.10. For filtering, only the H_{guass} filter was used, as the simulation results discussed in section 4.1 were demonstrated that better quality can be achieved using this filter.

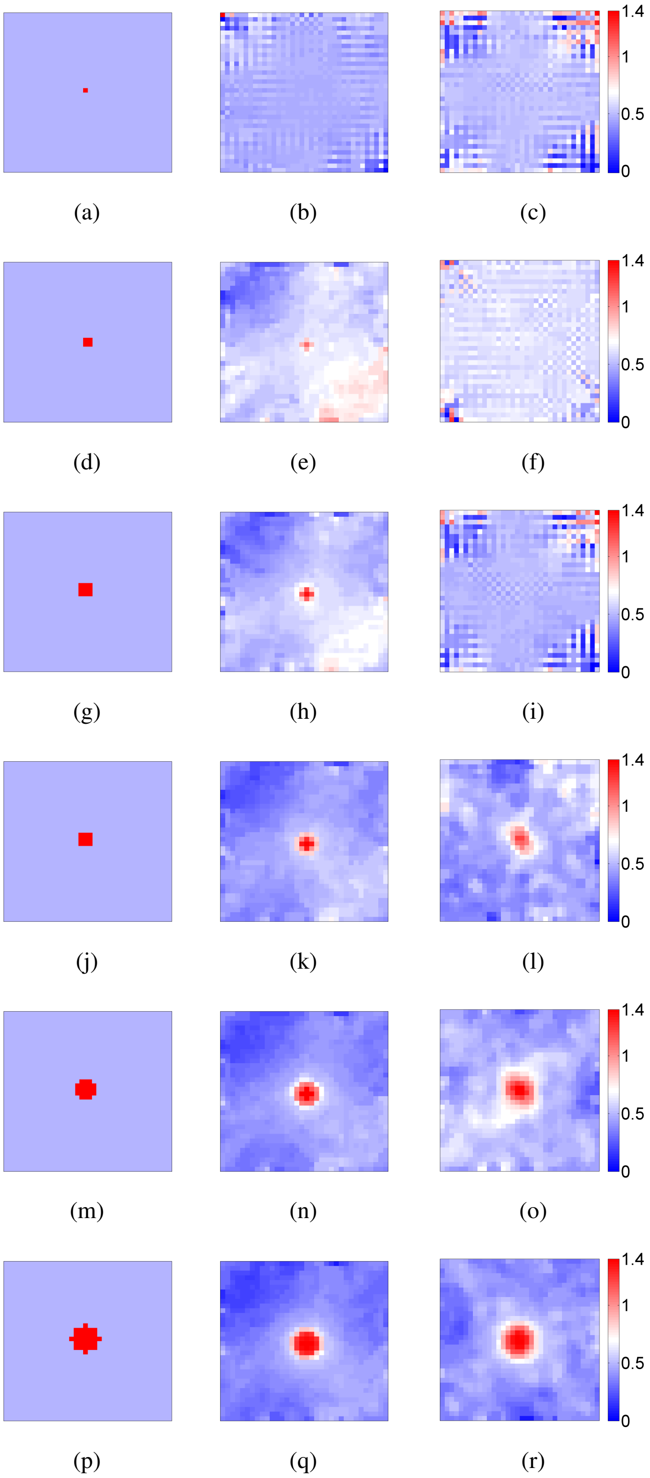

(a) (b) (c)

(d) (e) (f)

(g) (h) (i)

(j) (k) (l)

(m) (n) (o)

(p) (q) (r)

Figure 4.10: Resolution test data: Conductivity $[S/m]$ images in the left column illustrate the distributions used in the simulations. Conductivities in the middle and the right columns are reconstructed from B_z data collected using the standard and the proposed pulse sequences respectively. Six images are given in each column in correspondence to different object diameters: 2, 4, 6, 8, 10 and 12 mm respectively.

True conductivity distributions used in the simulations are shown in the left column of Figure 4.10, while those reconstructed from the data collected using the standard and the proposed pulse sequences are shown in the middle and right columns respectively. The pixel side-length in these images and in the used B_z data is 2 mm. Results in Figure 4.10 illustrate that the SMM algorithm was able to recognize the object conductivity if its diameter is at least 4 mm, which is twice the pixel side-length. However, only objects with 8 mm diameter and larger are recognizable in the data collected using the proposed pulse sequence. This loss in resolution is due to the filtering process used to extract signal replicas. For the imaging parameters used in MRiLab to obtain the k-space data used in this part, the bandwidth of the simulated k-space signals is $250\,m^{-1}$. Thus according to (2.29), the filter bandwidth is about $75\,m^{-1}$. A resolution of 2 mm requires a bandwidth of $250\,m^{-1}$, which is clearly larger than the filter bandwidth. This explains why the object in Figure 4.10 (a) is not recovered in Figure 4.10 (c). Similarly, the bandwidths needed for 4 mm and 6 mm resolution are $125\,m^{-1}$ and $83.3\,m^{-1}$ respectively. These bandwidths are also larger than the filter bandwidth. However, a resolution of 8 mm requires a bandwidth of $62.5\,m^{-1}$, which is within the filter bandwidth and thus the object of 8 mm diameter is recognized in Figure 4.10 (l). The loss in resolution can be compensated by collecting more frequency samples, as described in subsection 2.4.3. Assuming that the $N_{Ph,w}$ is increased three folds (up to 60) to enhance resolution by a factor of three, the needed scan time becomes $T_{S,Prop}$ = 4 minutes, which stills less than $T_{S,Conv}$ by the half. Therefore, the same resolution of the standard MREIT pulse sequence is achievable using the proposed pulse sequence with at least two folds gain in imaging speed.

4.2 Experimental Results

Results obtained experimentally during this study are presented in this section. Extracted B_z images of the uniform and the non-uniform phantoms are given in subsections 4.2.1 and 4.2.2 respectively. The latter also includes the reconstructed conductivity images of the non-uniform phantom. Afterwards, results related to SNR and minimum measurable current are given in subsections 4.2.3 and 4.2.4, respectively. Finally, the experiment done to investigate T_2^* issue is discussed in subsection 4.2.5.

4.2.1 Uniform Phantom

The SE and the GE versions of DCI-MREIT pulse sequence are used to image the magnetic flux density distribution inside the uniform phantom illustrated in Figure 3.5. Imaging is done using parameters similar to those listed in Table 3.7, with T_c and T_B being set to 9 ms and 10 ms respectively. A current of 20 mA amplitude is injected to the phantom using the current source described in subsection 3.2.2. The horizontal profile of the current is achieved by injecting current between the left and the right electrodes, while the vertical profile is achieved by using the top and the bottom electrodes. Acquired k-space signals of the two pulse sequences are shown in Figure 4.11 (a and b). Although during experiments full k-space data were collected (i.e., 256 phase-encoding lines) for analysis purposes, in practice partial acquisition can be used to reduce scan time, as only 85 phase-encoding lines are sufficient to extract B_z information.

In Figure 4.11 (a and b), the bottom left (and the top right) signal replica is dispersed due to the T_2^* relaxation discussed in subsection 2.4.4. By comparing the k-space data shown in Figure 4.11 (a and b), it is seen that the signals resulting from the unspoiled transverse components of $\overrightarrow{M}$ are more apparent in the k-space data obtained using GE-based pulse sequence. This is because T_2^* relaxation is larger in GE in comparison with SE, in which T_2^* relaxation is eliminated during T_E period by a 180° RF pulse. The bottom pair of signal replicas of both k-space data are filtered using H_{guass} filter, centered and transformed to spatial domain. Extracted B_z data from each k-space data are illustrated in Figure 4.11 (c-f). These experimentally obtained B_z data have similar distributions to those obtained using simulation, shown in Figure 4.4.

4.2.2 Non-uniform Phantom

Another experiment is done using a phantom of non-uniform conductivity distribution. The non-uniformity is formed by placing a square object at the center of the phantom whose conductivity differs from the background solution, as illustrated in Figure 3.6. With a similar procedure to that described in the previous subsection, two data sets of magnetic flux density are obtained using two pulse sequences: SE-based and GE-based DCI-MREIT. Extracted B_z images corresponding to the horizontal and the vertical current profiles are shown in Figure 4.12 (a-d). These data are then used to reconstruct conductivity using SMM. Recovered σ images are shown in Figure 4.12 (e and f).

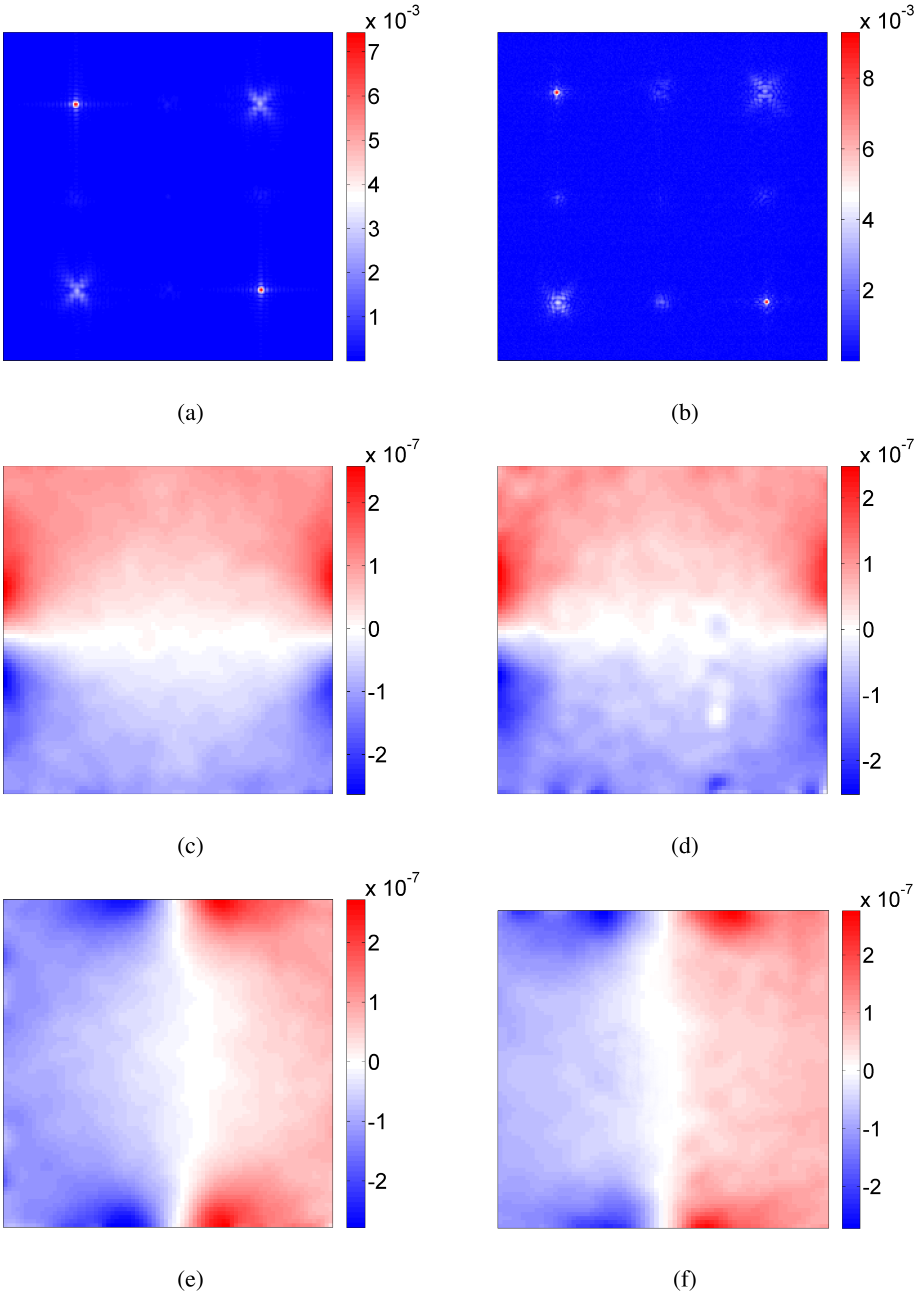

Figure 4.11: Uniform phantom data: k-space data obtained using (a) SE DCI-MRIET and (b) GE DCI-MRIET pulse sequences. Imaged (c) B_z^H and (e) B_z^V data using SE version of DCI-MRIET pulse sequence. Imaged (d) B_z^H and (f) B_z^V data using GE version of DCI-MRIET pulse sequence. B_z data are shown in [T].

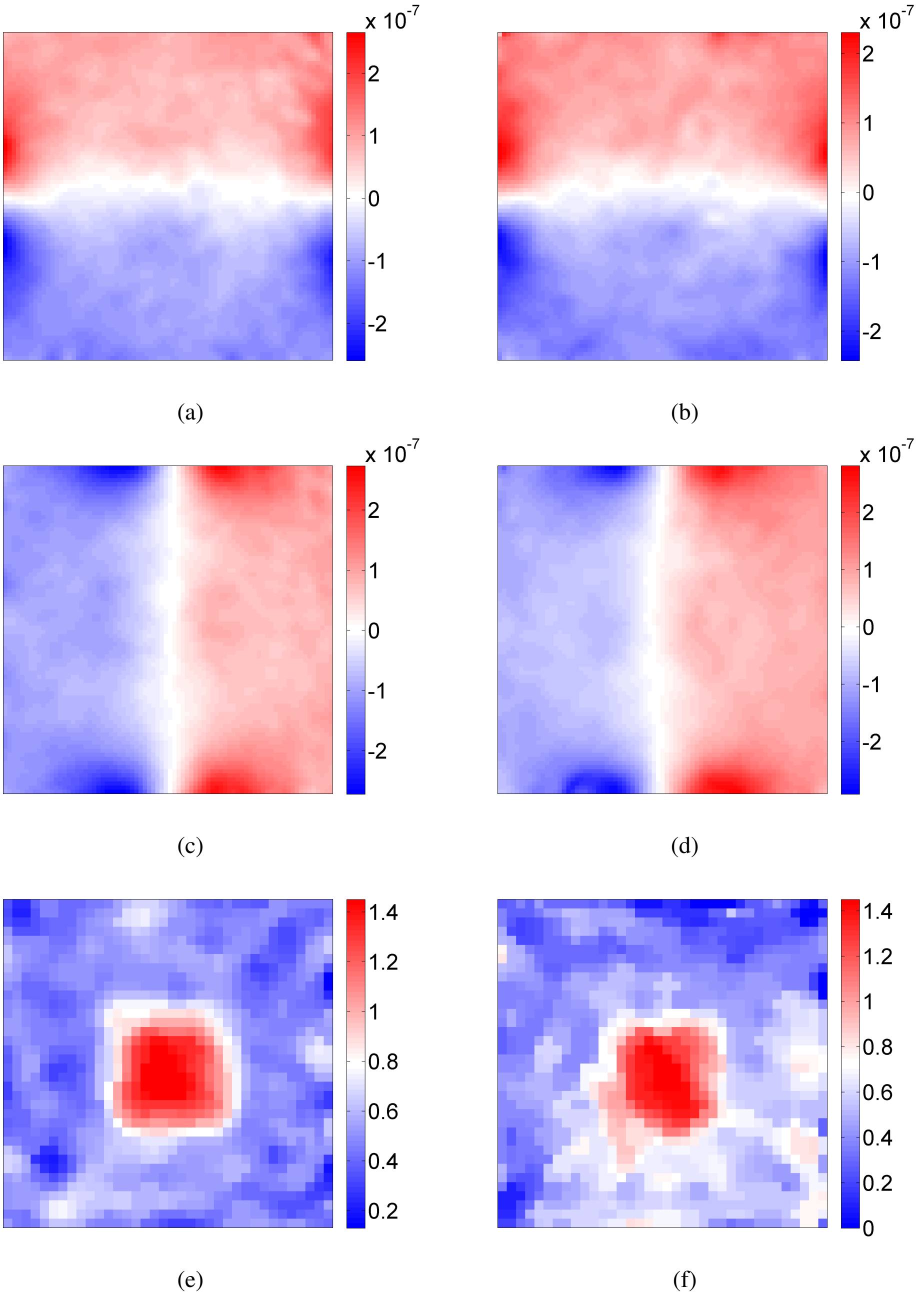

(a) (b)

(c) (d)

(e) (f)

Figure 4.12: Non-uniform phantom data: (a) B_z^H and (c) B_z^V data obtained using SE DCI-MRIET pulse sequence. Imaged (b) B_z^H and (d) B_z^V data using GE DCI-MRIET pulse sequence. (e) σ_{SE} and (f) σ_{GE} reconstructed from the data obtained using SE and GE versions of DCI-MRIET pulse sequence, respectively.

Recovered B_z data have similar distributions and range of values to those simulated shown in Figure 4.6. Qualitatively, reconstructed conductivity from B_z data obtained using SE DCI-MREIT pulse sequence has better quality than that obtained using GE

DCI-MREIT. This is also observed quantitatively from MSE values given in Table 4.2. σ_{SE} and σ_{GE} in Table 4.2 refer to the reconstructed conductivity from the B_z data obtained using SE and GE versions of the proposed pulse sequence, respectively.

Table 4.2: MSE [%] in reconstructed conductivities of the non-uniform phantom.

	σ_{SE}	σ_{GE}
MSE_{obj}	21.64	28.20
MSE_{bg}	21.94	33.79

4.2.3 Signal to Noise Ratio Measurements

The quality of measured MR signals are generally evaluated by looking to their SNR. Higher SNR value means either a stronger signal level is acquired, or a smaller noise level presented in the acquired MR signal. In the literature, several SNR calculation methods have been introduced for evaluating the performance of MR signals. In this study, two SNR formulas are used to calculate SNR level using a single signal acquisition, as described in [75]. Both formulas depend on defining a Region of Interest (ROI), referred to as ROI_s, for calculating the mean value m_s of the desired signal, and a region in the image background air, ROI_n, to estimate the mean value m_n and the standard deviation value ϱ_n of the noise. Then, SNR can be calculated as

$$SNR_{mean} = \frac{m_s}{\sqrt{\frac{2}{\pi}} m_n} = \frac{\underset{i,j \in ROI_s}{mean}\left(M(i,j)\right)}{\sqrt{\frac{2}{\pi}} \underset{i,j \in ROI_n}{mean}\left(M(i,j)\right)} \tag{4.4}$$

where $M(i,j)$ refers to the (i,j) pixel value in the magnitude of an MR image. $mean()$ is a function that calculates the mean value over a specified number of image pixels. Alternatively, noise standard deviation can be used in calculating SNR as

$$SNR_{stdv} = \frac{m_s}{\sqrt{\frac{2}{4-\pi}} \varrho_n} = \frac{\underset{i,j \in ROI_s}{mean}\left(M(i,j)\right)}{\sqrt{\frac{2}{4-\pi}} \underset{i,j \in ROI_n}{stdv}\left(M(i,j)\right)} \tag{4.5}$$

where $stdv()$ is a function that calculates the standard deviation of the values within a defined region. These formulas are used to determine SNR values of MR images obtained using Conventional SE pulse sequence and the two versions (SE and GE) of the proposed pulse sequence with different number of averaging (NEX): 1, 4 and 8. These data were collected using the imaging parameters given in Table 3.5. The left signal replica was used in calculating SNR values. Obtained results are listed in Table 4.3. Bandwidths of the both LPFs used in processing these data were set to be equal to one-third of the k-space bandwidth. A general impression from Table 4.3 is that both SNR calculation methods, SNR_{mean} and SNR_{stdv}, give somehow similar values with maximum standard deviation of ± 31. Besides, SE-based implementation of proposed pulse sequence provides a gain in SNR of 1.21 ± 0.16, in comparison with GE-based implementation. This is due the fact that SE-based pulse sequences avoid signal loss occurring in the duration between excitation RF pulse and echo time due to T_2^* relaxation. Another impression is that employing smooth-edged filters rather than sharp filters improves resultant SNR by a factor of 1.58 ± 0.18. By comparing SNR values in the third and the forth columns of Table 4.3, SNR values of images obtained using GE-based DCI-MREIT pulse sequence are lower by a factor of 0.58 ± 0.05 from those obtained using conventional MREIT pulse sequence. This coincides with the theoretical estimation given in (2.34) and calculated by considering a filter bandwidth covering 33.33% of the k-space width. Also, results show that the SNR of the proposed method can be enhanced by using a SE pulse sequence after the SPAMM preparation module. Further improvement can be obtained if H_{gauss} is used in the filtering. Last column in Table 4.3 shows that the SNR values of the images obtained using the SE-based pulse sequence and filtered using H_{gauss} are slightly better than those obtained using the conventional SE MREIT pulse sequence.

Table 4.3: SNR values of magnitude images obtained by 3 different pulse sequences.

NEX	Method	Conv. SE	GE DCI-MREIT		SE DCI-MREIT	
			H_{square}	H_{gauss}	H_{square}	H_{gauss}
1	SNR_{mean}	218.24	139.61	208.29	157.94	229.99
	SNR_{stdv}	220.47	135.03	190.52	149.12	232.33
4	SNR_{mean}	421.86	248.35	361.58	300.72	427.78
	SNR_{stdv}	399.21	243.20	402.12	280.88	421.42
8	SNR_{mean}	540.28	307.44	530.00	416.30	636.70
	SNR_{stdv}	527.59	263.16	520.57	430.02	677.92

4.2.4 Minimum Measurable Current

For a current to be measurable in MREIT, the standard deviation of the magnetic flux density produced by the injected current must be greater than that produced by the noise presented in the imaging system. Therefore, an estimation for the minimum measurable current level in any MR system can be done by knowing the level of noise in that system. One way to measure the noise level is by obtaining two MR phase images using the pulse sequence being investigated without injecting current. The phase difference of these two phase images reflects the noise presented in the magnetic flux density data measured using MREIT. This noise data is treated as a magnetic flux density data that is used to reconstruct current density image. After recovering x and y components of current density, total current density J_t is obtained as the absolute of these two components. Then, minimum current density J_{min} that can be measured using this imaging system is calculated as the root mean square of J_t [76]. From J_{min}, minimum current I_{min} that should be applied through the electrodes can be calculated by integrating the current density over the surface area of the electrode. During the experiments of this study, the surface area of the used electrodes was $2 \times 2\,cm^2$. Since noise level decreases by increasing the number of averaging, the experiment was repeated to see the achievable I_{min} at 1, 4 and 8 averaging respectively. Imaging parameters used in this part are listed in Table 3.5, and obtained results are summarized in Table 4.4. Calculated J_{min} and I_{min} of the conventional SE pulse sequence are similar to those reported in [32] with a deviation of ± 0.12. Table 4.4 shows that the amount of current to be measurable using GE-based pulse sequence is almost twice larger than the current level which is needed in the conventional SE. However, this is not the case for SE-based pulse sequence, as it is able to measure current levels similar to those measurable with conventional SE.

Table 4.4: $J_{min}[A/m^2]$ and $I_{min}[mA]$ of 3 different MREIT pulse sequences.

	Conventional SE		GE DCI-MREIT		SE DCI-MREIT	
NEX	J_{min}	I_{min}	J_{min}	I_{min}	J_{min}	I_{min}
1	1.04	0.42	1.75	0.69	1.01	0.40
4	0.60	0.24	0.97	0.39	0.55	0.22
8	0.42	0.17	0.86	0.34	0.38	0.15

4.2.5 $\mathbf{T_2^*}$ Measurement and Limitation

T_2^* relaxation time affects the quality of the acquired MR signal and puts a limitation on the time duration of the injected current, as discussed in section 2.4.4. To predict this limitation, an experiment is done to measure T_2^* of the phantom being used at 3T magnet strength. In this experiment, four GE images with four different echo times were collected. Imaging parameters are given in Table 3.6. Long T_R and small flip angle were used to ensure full longitudinal recovery of magnetization.

Under these conditions, the magnitude of the acquired k-space signal peak at T_E, $S_p(T_E)$, can be related to the peak value at zero time $S_p(0)$ through an exponential relation as [77]

$$S_p(T_E) = S_p(0)e^{\frac{-T_E}{T_2^*}} \tag{4.6}$$

With two different echo times substituted in (4.6) and taking the division,

$$\frac{S_p(T_{E,2})}{S_p(T_{E,1})} = e^{\frac{T_{E,1}-T_{E,2}}{T_2^*}} \tag{4.7}$$

Taking the natural logarithm of both sides of (4.7), T_2^* can be calculated as

$$T_2^* = \frac{T_{E,1} - T_{E,2}}{ln(\frac{S_p(T_{E,2})}{S_p(T_{E,1})})} \tag{4.8}$$

Using (4.8), T_2^* is calculated for each possible combination of the acquired GE signals, as listed in Table 4.5. Obtained T_2^* values swing about the average value given at the end of the table. In addition, equation (4.7) can be used to plot the exponential curve after normalizing signals peaks by the peak value of $T_{E,1} = 5$ ms. This exponential curve is shown in Figure 4.13 in red-colored solid-line. Using curve-fitting, a curve that best fits the exponential curve connecting the peak values of the acquired signals was obtained using a value of $T_2^* = 14.6$ ms. This curve is shown in Figure 4.13 using blue-colored dashed-line. T_2^* value obtained by curve-fitting is near the average value listed in Table 4.5. Therefore, the value of T_2^* of the solution used in the phantom at 3T can be taken as 14.6 ms.

The second part of this experiment involves estimating an upper limit for the possible duration of injected current that guarantees minimal loss in B_z data. For this purpose, several data are collected using the SE version of the proposed pulse sequence, with different T_B times: 14, 16, 18 and 20 ms. These data were collected using the SE version of DCI-MREIT pulse sequence, as this pulse sequence demonstrated better performance in comparison to the GE version. Imaging parameters used to collect data are given in Table 3.7. Possible T_2^* limitation is focused at the bottom left (and the top right) signal replica of the k-space, which suffers T_2^* decay. In Figure 4.14 (a, c and e), zoomed views of this signal replica are shown at T_B of 14, 18 and 20 ms respectively. The corresponding B_z^H data recovered from these measurements are shown in Figure 4.14 (b, d and f) respectively.

Figure 4.14(a, c and e) demonstrate the T_2^* decay of the left signal replica as the time gap between RF pulses, T_B, increases. It spreads over the k-space with time, and if

Table 4.5: Calculated T_2^* values for different pairs of echo times.

$T_{E,1}[ms]$	$T_{E,2}[ms]$	$T_2^*[ms]$
5	10	13.34
5	20	14.65
5	50	14.82
10	20	15.41
10	50	15.03
20	50	14.90
Average		14.69

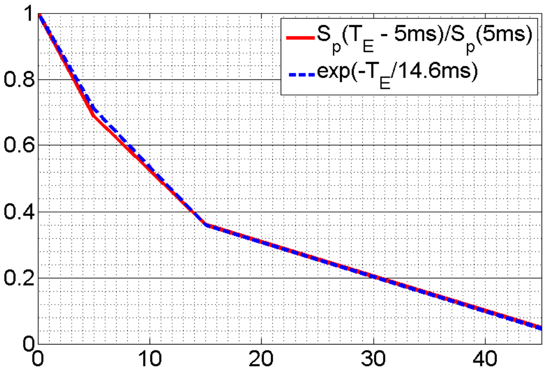

Figure 4.13: A plot of the curve that connects the peak values of acquired GE signals is given in red-colored solid-line. A plot of an exponential curve that fits the values of the red-colored curve is given in blue-colored dashed-line.

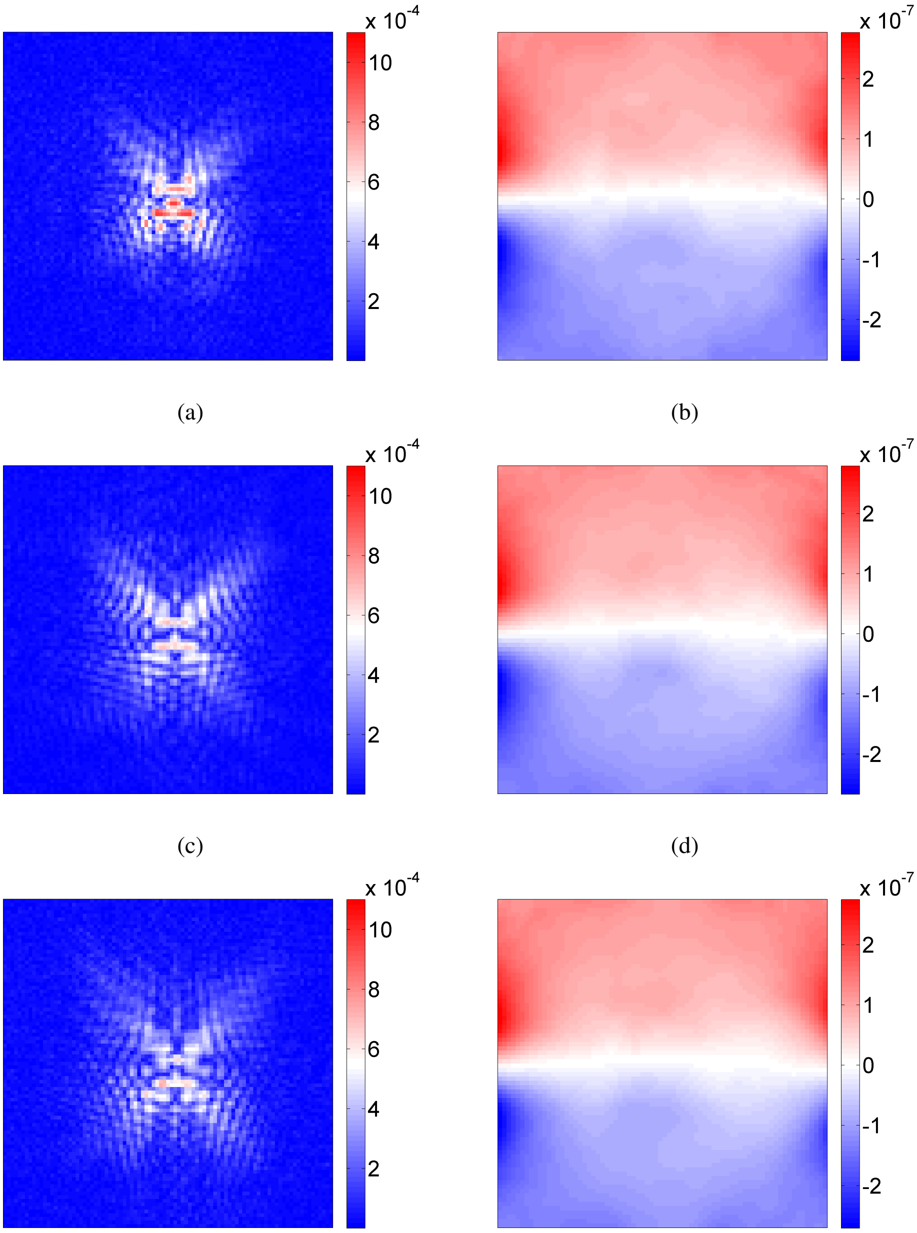

(a) (b) (c) (d) (e) (f)

Figure 4.14: Zoomed view of the bottom left signal replica cropped from the k-space data obtained with T_B of (a) 14, (c) 18, and (e) 20 ms. Recovered B_z^H data in corresponding to the data acquired with T_B of (b) 14 ,(d) 18 ,and (f) 20 ms. The unit of the shown magnetic flux density data is [T].

this spread continues, parts of this signal become out of the filter window. The larger the parts out of the window, the larger the loss in the magnetic flux density data stored in this signal. To quantitatively evaluate this loss, the energy of the bottom left signal replica is calculated at each T_B using

$$E = \sum_{k_x \in W} \sum_{k_y \in W} |S(k_x, k_y)|^2 \tag{4.9}$$

where W refers to the group of the k-space coordinates (k_x, k_y) within the filter window. Calculated signal energy values are given in Table 4.6. The percentage loss in energy calculated with respect to the signal energy obtained with $T_B = 14\,ms$ are also listed in Table 4.6. These results state that almost 9% of signal energy is lost when T_B is increased from 14 ms to 20 ms.

On the other hand, with perceptually evaluating the results illustrated in Figure 4.14 (b, d and f), no apparent differences are observed in the B_z data obtained using different T_B times. Assuming the duration of 19 ms as an upper limit for the duration of the injected current for each profile, this limit is almost 130% of the calculated T_2^* value. On the other hand, T_2^* relaxation of human brain tissues have been experimentally estimated, in 3T imaging system, to be in the range between 41.6 ms - 51.8 ms [70]. Accordingly, a current of at least 54 ms duration (130% of 41.6 ms), for each profile, can be used for injection with the proposed MREIT pulse sequence in 3T MR system. This duration is acceptable and comparable with the durations of current pulses used in literature with 3T scanners, as can be seen in Table 1.1. Thus, T_2^* relaxation does not impede the applicability of the proposed pulse sequence.

Table 4.6: Calculated signal energy and percentage loss at different T_B durations.

$T_B[ms]$	E	Energy loss w.r.t. the signal of $T_B = 14\,ms$
14	1.37×10^{-04}	–
16	1.32×10^{-04}	3.69%
18	1.26×10^{-04}	7.98%
20	1.25×10^{-04}	9.00%

CHAPTER 5

CONCLUSIONS

In MRI, the time needed for acquiring MR signals depends on the employed concept in the pulse sequence used to operate the MR scanner. Minimizing this time has been always an attractive research area for scientists. This is because long imaging time discomforts patients. Although the time needed to obtain a cross-sectional image is bearable in most pulse sequences, many MR applications rely on obtaining 3D images, which makes scan time too long. This time becomes long also if it is aimed to improve the quality of the acquired signal by averaging. Long acquisition time also makes MR images vulnerable to distortions arising from patient involuntary movements. Furthermore in functional imaging applications, images should be obtained rapidly to recognize any changes due to activities happening within short time periods. Therefore, reducing imaging time improves the temporal resolution in functional images.

MREIT pulse sequences typically have a long scan time, because of the need to inject current within the imaging time. Furthermore, the used time for current injection has to be sufficiently long to produce current-related magnetic field of decent quality. In addition, multiple current injection patterns are typically used to recognize more details about the conductivity distribution of the imaged object. However, to avoid the above mentioned issues of long imaging time, several studies have proposed techniques to reduce scan time in MREIT. One way is to use a single-acquisition based pulse sequence for MREIT. Another way is to use GE based pulse sequence with low flip-angle. The latter however reduces the SNR of the acquired image.

In this thesis, a new MREIT pulse sequence is proposed providing the ability to reduce the scan time to the half. This reduction in time is achieved by injecting two current profiles in a single acquisition, by utilizing SPAMM technique. SPAMM is used to split the MR signal in k-space into two signals before the beginning of the actual imaging pulse sequence. Magnetic flux density information of the two injected current profiles are stored in these two k-space signals. Then, the actual imaging pulse sequence collects these signals. In the proposed pulse sequence, considerable time is also saved by avoiding the time needed for manually switching the current channels for each injection profile.

This concept was tested using pulse sequence simulator, MRiLab. Simulation results showed the validity of the proposed method. Obtained results demonstrated also the importance of selecting the type of the used LPF in the quality of the reconstructed conductivity. Smooth filters reduce the amount of error in the recovered conductivity map, in comparison with sharp filters. MSE values in the results obtained by employing a Gaussian filter are 3.84% lower than those obtained using a square filter.

However, employing filters for extracting signal replicas affects the spatial resolution of the recovered conductivity images. Compensating the loss in the resolution can be done by collecting a wider range of spatial frequencies. This will increase the scan time, but the overall time will not exceed half the time needed by the standard pulse sequence. In other words, the proposed pulse sequence is able to obtain the same spatial resolution but twice faster, in comparison with the standard pulse sequence.

Physical phantoms are also used to evaluate the proposed pulse sequence experimentally. Two versions of the proposed pulse sequence were designed: one based on SE, and the other based on GE pulse sequence. Better performance was observed using the SE-based pulse sequence. SNR of images obtained using SE version were generally 21% larger than those obtained using GE version. Error values in the reconstructed conductivities were also lower by 6.56% in the results obtained using SE version. Results have demonstrated also that the SE version is able to measure current of almost 46% lower amplitude level in comparison with the GE version. This superiority of the SE-based version over the GE-based comes from the reduced T_2^*-related signal decay in the data collected using the SE-based pulse sequence.

On the other hand, the performance of the SE-based DCI-MREIT pulse sequence in comparison with the conventional MREIT pulse sequence were also investigated. The SNR and the minimum measurable current values of these two pulse sequences were found to be comparable. The SNR values obtained using the SE-based DCI-MREIT pulse sequence are 5-15% higher than those obtained using the standard SE MREIT pulse sequence. In addition, the SE-based DCI-MREIT pulse sequence is able to measure current of 5-11% lower level depending on the number of averaging used during the measurements. This slightly better performance observed with the SE-based DCI-MREIT over the conventional MREIT is due to the reduction of noise during filtering.

Furthermore, a part of this study was dedicated to investigate the possible limitation of the inherited T_2^* effect on the realization of the proposed pulse sequence. If T_2^* relaxation would allow only a very short duration for current injection, this would make the proposed method infeasible. However, experimental results showed that a current of duration up to 54 ms can be used with the SE-based DCI-MREIT pulse sequence at 3T system, which is acceptable and comparable with the current durations used in the literature.

To conclude, in the new MREIT method proposed in this study, two current injection patterns can be applied within each T_R, allowing 50% reduction in the required acquisition time. The concept of this method was verified using simulations and experiments. In experiments, the concept was implemented on SE and GE based pulse sequences. However, taking full advantage of this method would be by implementing the concept on a fast single-shot pulse sequence. Such a pulse sequence has the advantage of collecting many phase-encoding lines in each T_R, which reduces the scan time extremely. Another advantage of using this type of pulse sequences is that the number of times needed to inject current is also reduced. Rather than injecting current for each phase-encoding line, several lines will be collected with only one current injection. This way the number of current injection is reduced, as well as the time gap between successive current injections is prolonged. This in total reduces patient discomfort and current injection hazards, as patient will be exposed to a fewer number of current pulses and the time gap between these pulses will be much longer.

Among possible fast implementations, a better performance is expected from using SE-based fast imaging pulse sequences, as these are more immune towards T_2^* relaxation. Examples of these pulse sequences include Fast Spin-Echo (FSE) and Turbo-Gradient Spin-Echo (TGSE). An alternative way to get full benefit from the proposed method is by collecting multiple echoes within the same repetition time T_R. This way, a gain in speed is achieved by excluding the time needed for averaging.

Realizing these two options form the outline of the planned future work. The proposed method has to be implemented on an FSE based pulse sequence as well as a multi-echo pulse sequence. These two versions have to be tested experimentally, looking for better performance and any possible practical issues. Besides, further study should be devoted to optimize the shape of the filter used for k-space signals extraction. In this study, two filter types were used to demonstrate the impact of the filter shape on the quality of the recovered conductivity data. However, more sophisticated filters may guarantee much better quality. Therefore, it is worthy to investigate this side in more detail.

In addition, optimizing the proposed pulse sequence itself is another important part of the future work. Although, the recent form of DCI-MREIT has been proved of being able to reduce the scan time by a factor of two, another forms may provide much shorter scan time or much better quality. Using the recent form of DCI-MREIT, the quality of the signal recovered from the left replica differs from that extracted from the right replica. This is because the left replica is exposed to T_2^* relaxation while the right replica is not.

One possible modification suggests placing a 180° hard RF pulse at the middle between the first and the second RF pulses of the SPAMM module. This will transfer half of the T_2^* relaxation to the right replica, which reduces the T_2^* effect on the left replica to the half and makes the quality of both replica much similar. However, this increases the number of RF pulses and thus the overall complexity of the pulse sequence. Analytical study of this issue might incorporate the effect of the additional 180° RF pulse but with much simple design.

Furthermore, since the ultimate goal of MREIT studies is making it feasible clinically, the performance of DCI-MREIT has to be investigated with low current levels.

Results illustrated in this study was obtained using 20 mA current, which is above the safety limit ($100\ \mu A$). Evaluating the proposed method at lower current levels should be aimed in future studies. Results presented in subsection 4.2.4 state that a current of 150 μA is measurable using the SE version of the proposed pulse sequence with 8 averaging. This current amplitude is slightly lower than the measurable current using the conventional MREIT pulse sequence (170 μA).

REFERENCES

[1] L. A. Geddes and L. E. Baker. The specific resistance of biological material—a compendium of data for the biomedical engineer and physiologist. *Medical and Biological Engineering*, 5(3):271–293, 1967.

[2] C. Gabriel, S. Gabriel, and E. Courhout. The dielectric properties of biological tissues: I. literature survey. *Physics in Medicine and Biology*, 41(11):2231, 1996.

[3] R. H. Bayford. Bioimpedance tomography (electrical impedance tomography). *Annual Review of Biomedical Engineering*, 8:63–91, 2006.

[4] A. McEwan, A. Romsauerova, R. Yerworth, L. Horesh, R. Bayford, and D. Holder. Design and calibration of a compact multi-frequency EIT system for acute stroke imaging. *Physiological Measurement*, 27(5):S199, 2006.

[5] I. Hancu, J. C. Roberts, S. Bulumulla, and S. K. Lee. On conductivity, permittivity, apparent diffusion coefficient, and their usefulness as cancer markers at MRI frequencies. *Magnetic Resonance in Medicine*, 73(5):2025–2029, 2015.

[6] J. P. Morucci and B. Rigaud. Bioelectrical impedance techniques in medicine. part iii: Impedance imaging. third section: medical applications. *Critical Reviews in Biomedical Engineering*, 24(4-6):655–677, 1995.

[7] K. A. Awada, D. R. Jackson, S. B. Baumann, J. T. Williams, D. R. Wilton, P. W. Fink, and B. R. Prasky. Effect of conductivity uncertainties and modeling errors on EEG source localization using a 2-D model. *IEEE Transactions on Biomedical Engineering*, 45(9):1135–1145, 1998.

[8] Y. Kim, J. B. Fahy, and B. J. Tupper. Optimal electrode designs for electrosurgery, defibrillation, and external cardiac pacing. *IEEE Transactions on Biomedical Engineering*, (9):845–853, 1986.

[9] B. M. Eyüboğlu. Magnetic resonance current density imaging. *Wiley Encyclopedia of Biomedical Engineering*, 2006.

[10] R. M. Gulrajani. *Bioelectricity and biomagnetism.* J. Wiley, 1998.

[11] R. P. Henderson and J. G. Webster. An impedance camera for spatially specific measurements of the thorax. *IEEE Transactions on Biomedical Engineering*, (3):250–254, 1978.

[12] A. D. Seagar, D. C. Barber, and B. H. Brown. Electrical impedance imaging. *IEE Proceedings A-Physical Science, Measurement and Instrumentation, Management and Education-Reviews*, 134(2):201–210, 1987.

[13] B. H. Brown. Electrical impedance tomography (EIT): a review. *Journal of Medical Engineering & Technology*, 2009.

[14] M. Bodenstein, M. David, and K. Markstaller. Principles of electrical impedance tomography and its clinical application. *Critical Care Medicine*, 37(2):713–724, 2009.

[15] G. C. Scott, M. L. G. Joy, R. L. Armstrong, and R. M. Henkelman. Measurement of nonuniform current density by magnetic resonance. *IEEE Transactions on Medical Imaging*, 10(3):362–374, 1991.

[16] N. Zhang. Electrical impedance tomography based on current density imaging. Master's Thesis, University of Toronto, Canada, 1992.

[17] E. J. Woo, S. Y. Lee, and C. W. Mun. Impedance tomography using internal current density distribution measured by nuclear magnetic resonance. In *SPIE's 1994 International Symposium on Optics, Imaging, and Instrumentation*, pages 377–385. International Society for Optics and Photonics, 1994.

[18] M. A. Bernstein, K. F. King, and X. J. Zhou. *Handbook of MRI pulse sequences*. Elsevier, 2004.

[19] V. E. Arpinar, M. J. Hamamura, E. Degirmenci, and L. T. Muftuler. MREIT experiments with 200 μA injected currents: a feasibility study using two reconstruction algorithms, SMM and harmonic Bz. *Physics in Medicine and Biology*, 57(13):4245–4261, 2012.

[20] M. J. Hamamura and L. T. Muftuler. Fast imaging for magnetic resonance electrical impedance tomography. volume 26, pages 739–745. Elsevier, 2008.

[21] G. C. Scott, M. L. G. Joy, R. L. Armstrong, and R. M. Henkelman. Sensitivity of magnetic-resonance current-density imaging. *Journal of Magnetic Resonance (1969)*, 97(2):235–254, 1992.

[22] U. Mikac, F. Demšar, K. Beravs, and I. Serša. Magnetic resonance imaging of alternating electric currents. *Magnetic Resonance Imaging*, 19(6):845–856, 2001.

[23] C. Park, B. I. Lee, O. Kwon, and E. J. Woo. Measurement of induced magnetic flux density using injection current nonlinear encoding (ICNE) in MREIT. *Physiological Measurement*, 28(2):117–127, 2006.

[24] A. S. Minhas, E. J. Woo, and S. Y. Lee. Magnetic flux density measurement with balanced steady state free precession pulse sequence for MREIT: a simulation

study. In *2009 Annual International Conference of the IEEE Engineering in Medicine and Biology Society*, pages 2276–2278. IEEE, 2009.

[25] A. S. Minhas, E. J. Woo, and R. Sadleir. Simulation of MREIT using balanced steady state free precession (b-SSFP) pulse sequence. In *Journal of Physics: Conference Series*, volume 224, page 012019. IOP Publishing, 2010.

[26] Y. Q. Han, Z. J. Meng, W. C. Jeong, Y. T. Kim, A. S. Minhas, H. J. Kim, H. S. Nam, O. Kwon, and E. J. Woo. MREIT conductivity imaging of canine head using multi-echo pulse sequence. In *Journal of Physics: Conference Series*, volume 224, page 012078. IOP Publishing, 2010.

[27] H. Lee, W. C. Jeong, H. J. Kim, E. J. Woo, and J. Park. Alternating steady state free precession for estimation of current-induced magnetic flux density: A feasibility study. *Magnetic Resonance in Medicine*, 2015.

[28] H. Lee, C. H. Sohn, and J. Park. Current-induced alternating reversed dual-echo-steady-state for joint estimation of tissue relaxation and electrical properties. *Magnetic Resonance in Medicine*, 2016.

[29] T. P. DeMonte, R. S. Yoon, D. B. Jorgenson, and M. L. G. Joy. A system for in-vivo cardiac defibrillation current density imaging in a pig. In *Engineering in Medicine and Biology Society, 2003. Proceedings of the 25th Annual International Conference of the IEEE*, volume 1, pages 175–178. IEEE, 2003.

[30] T. I. Oh, W. C. Jeong, J. E. Kim, S. Z. K. Sajib, H. J. Kim, O. I. Kwon, and E. J. Woo. Noise analysis in fast magnetic resonance electrical impedance tomography (MREIT) based on spoiled multi gradient echo (SPMGE) pulse sequence. *Physics in Medicine and Biology*, 59(16):4723–4738, 2014.

[31] O. I. Kwon, M. Chauhan, H. J. Kim, W. C. Jeong, H. Wi, T. I. Oh, and E. J. Woo. Fast conductivity imaging in magnetic resonance electrical impedance tomography (MREIT) for RF ablation monitoring. *International Journal of Hyperthermia*, 30(7):447–455, 2014.

[32] K. Sümser, N. Naji, M. Sadighi, H. H. Eroğlu, and M. Eyüboğlu. MRI-SPAMM based magnetic resonance electrical impedance tomography (MREIT). In *The International Society for Magnetic Resonance in Medicine (ISMRM) 24th Annual Meeting, May 7-13,2016,Singapore, Singapore*, page 1940. ISMRM, 2016.

[33] B. M. Eyüboğlu, Ö. Birgül, and Y. Z. Ider. Magnetic resonance electrical impedance tomography (MR-EIT): A new technique for high resolution conductivity imaging. In *Proceedings of the Second EPSRC Engineering Network Meeting on Biomedical Applications of EIT, London, UK*, pages 76–79, 2000.

[34] Ö. Birgül, B. M. Eyüboğlu, and Y. Z. Ider. New technique for high-resolution absolute conductivity imaging using magnetic-resonance electrical impedance

tomography (MR-EIT). In *Medical Imaging 2001*, pages 880–888. International Society for Optics and Photonics, 2001.

[35] O. Kwon, J. Y. Lee, and J. R. Yoon. Equipotential line method for magnetic resonance electrical impedance tomography. *Inverse Problems*, 18(4):1089, 2002.

[36] M. S. Özdemir, B. M. Eyüboğlu, and O. Özbek. Equipotential projection-based magnetic resonance electrical impedance tomography and experimental realization. *Physics in Medicine and Biology*, 49(20):4765, 2004.

[37] H. S. Khang, B. I. Lee, S. H. Oh, E. J. Woo, S. Y. Lee, M. H. Cho, O. Kwon, J. R. Yoon, and J. K. Seo. J-substitution algorithm in magnetic resonance electrical impedance tomography (MREIT): phantom experiments for static resistivity images. *IEEE Transactions on Medical Imaging*, 21(6):695–702, 2002.

[38] Ö. Birgül, B. M. Eyüboğlu, and Y. Z. Ider. Current constrained voltage scaled reconstruction (CCVSR) algorithm for MR-EIT and its performance with different probing current patterns. *Physics in Medicine and Biology*, 48(5):653, 2003.

[39] Y. Z. Ider, S. Onart, and W. R. B. Lionheart. Uniqueness and reconstruction in magnetic resonance-electrical impedance tomography (MR-EIT). *Physiological Measurement*, 24(2):591, 2003.

[40] Y. Z. Ider and S. Onart. Algebraic reconstruction for 3D magnetic resonance-electrical impedance tomography (MREIT) using one component of magnetic flux density. *Physiological Measurement*, 25(1):281, 2004.

[41] Y. Z. Ider and Ö. Birgül. Use of the magnetic field generated by the internal distribution of injected currents for electrical impedance tomography (MR-EIT). *Turkish Journal of Electrical Engineering & Computer Sciences*, 6(3):215–226, 2000.

[42] Ö. Birgül, O. Ozbek, B. M. Eyüboğlu, and Y. Z. Ider. Magnetic resonance-conductivity imaging using 0.15 tesla MRI scanner. In *Engineering in Medicine and Biology Society, 2001. Proceedings of the 23rd Annual International Conference of the IEEE*, volume 4, pages 3384–3387. IEEE, 2001.

[43] Ö. Birgül, B. M. Eyüboğlu, and Y. Z. Ider. Experimental results for 2D magnetic resonance electrical impedance tomography (MR-EIT) using magnetic flux density in one direction. *Physics in Medicine and Biology*, 48(21):3485–3504, 2003.

[44] L. T. Muftuler, M. Hamamura, Ö. Birgül, and O. Nalcioğlu. Resolution and contrast in magnetic resonance electrical impedance tomography (MREIT) and its application to cancer imaging. *Technology in Cancer Research & Treatment*, 3(6):599–609, 2004.

[45] S. H. Oh, B. I. Lee, E. J. Woo, S. Y. Lee, M. H. Cho, O. Kwon, and J. K. Seo. Conductivity and current density image reconstruction using harmonic Bz algorithm in magnetic resonance electrical impedance tomography. *Physics in Medicine and Biology*, 48(19):3101–3116, 2003.

[46] J. K. Seo, K. Jeon, C. O. Lee, and E. J. Woo. Non-iterative harmonic Bz algorithm in MREIT. *Inverse Problems*, 27(8):1–12, 2011.

[47] W. C. Jeong, Y. T. Kim, H. J. Kim, C. Y. Lim, H. M. Park, and E. J. Woo. Conductivity imaging of animal and human body using 3T magnetic resonance electrical impedance tomography (MREIT). In *Progress In Electromagnetics Research Symposium Proceedings,*, pages 53–56, Kuala Lumpur, Malaysia, 2012.

[48] J. K. Seo, H. C. Pyo, C. Park, O. Kwon, and E. J. Woo. Image reconstruction of anisotropic conductivity tensor distribution in MREIT: computer simulation study. *Physics in Medicine and Biology*, 49(18):4371, 2004.

[49] E. Değirmenci and B. M. Eyüboğlu. Anisotropic conductivity imaging with MREIT using equipotential projection algorithm. *Physics in Medicine and Biology*, 52(24):7229–7242, 2007.

[50] E. Değirmenci and B. M. Eyüboğlu. Anisotropic conductivity imaging with MREIT using j-substitution and hybrid j-substitution algorithms. In *World Congress on Medical Physics and Biomedical Engineering, September 7-12, 2009, Munich, Germany*, pages 315–318. Springer, 2009.

[51] E. Degirmenci. *High resolution imaging of anisotropic conductivity with magnetic resonance electrical impedance tomography (MR-EIT).* PhD Thesis, Middle East Technical University, Turkey, 2010.

[52] O. I. Kwon, W. C. Jeong, S. Z. K. Sajib, H. J. Kim, and E. J. Woo. Anisotropic conductivity tensor imaging in mreit using directional diffusion rate of water molecules. *Physics in Medicine and Biology*, 59(12):2955, 2014.

[53] H. H. Eroglu, M. Sadighi, K. Sumser, N. Naji, and B. M. Eyuboglu. Experimental realization of induced current magnetic resonance current density imaging. In *Proceedings of the Annual International Conference of the IEEE Engineering in Medicine and Biology Society, Milano, Italy*, pages 614–617, 2015.

[54] L. A. Van, A. T. Berg, and U. Katscher. Measuring electrical conductivity at low frequency using the eddy currents induced by the imaging gradients. page 3467. Proceedings of the 20th Annual Meeting of ISMRM,,Melbourne, Victoria, 2012.

[55] J. Su, B. Zheng, S. F. Y. Li, and S. Y. Huang. Further study of the effects of a time-varying gradient fields on phase maps—theory and experiments. In *Proceedings of the 23rd Annual Meeting of ISMRM, Toronto, Ontario, Canada*, page 3291, 2015.

[56] C. Liu, W. Li, and I. Argyridis. Imaging electric conductivity and conductivity anisotropy via eddy currents induced by pulsed field gradients. In *Proceedings of the 22nd Annual Meeting of ISMRM, Milano, Italy*, page 0638, 2014.

[57] S. Mandija, A. Lier, U. Katscher, P. I. Petrov, S. F. W. Neggers, P. R. Luijten, and C. A. T. Berg. A geometrical shift results in erroneous appearance of low frequency tissue eddy current induced phase maps. *Magnetic resonance in medicine*, 2015.

[58] E. Gibbs and C. Liu. Feasibility of imaging tissue electrical conductivity by switching field gradients with mri. *Tomography: a journal for imaging research*, 1(2):125–135, 2015.

[59] O. F. Oran and Y. Z. Ider. Feasibility of conductivity imaging using subject eddy currents induced by switching of mri gradients. *Magnetic Resonance in Medicine*, 2016.

[60] X. Zhang, J. Liu, and B. He. Magnetic-resonance-based electrical properties tomography: a review. *IEEE Reviews in Biomedical Engineering*, 7:87–96, 2014.

[61] J. Liu, X. Zhang, S. Schmitter, V. de Moortele, and B. He. Gradient-based electrical properties tomography (gept): A robust method for mapping electrical properties of biological tissues in vivo using magnetic resonance imaging. *Magnetic Resonance in Medicine*, 74(3):634–646, 2015.

[62] N. Gurler and Y. Z. Ider. Gradient-based electrical conductivity imaging using mr phase. *Magnetic Resonance in Medicine*, 2016.

[63] Y. T. Kim, B. I. Lee, E. J. Woo, and H. J. Kim. In vivo MREIT experiment of canine brain. In *13th International Conference on Electrical Bioimpedance and the 8th Conference on Electrical Impedance Tomography*, pages 512–515. Springer, 2007.

[64] W. C. Jeong, Y. T. Kim, A. S. Minhas, T. H. Lee, H. J. Kim, H. S. Nam, O. Kwon, and E. J. Woo. In vivo conductivity imaging of human knee using 3 mA injection current in MREIT. In *Journal of Physics: Conference Series*, volume 224, page 012148. IOP Publishing, 2010.

[65] M. Sadighi. Magnetic resonance conductivity tensor imaging (MRCTI) at 3 tesla. Master's Thesis, Middle East Technical University, Turkey, 2014.

[66] R. C. Gonzalez and R. E. Woods. Digital image processing. *Nueva Jersey*, 2008.

[67] R. C. Aster, B. Borchers, and C. H. Thurber. *Parameter Estimation and Inverse Problems*. Academic Press, 2012.

[68] P. C. Hansen. *The L-curve and its use in the numerical treatment of inverse problems*. IMM, Department of Mathematical Modelling, Technical University of Denmark, 1999.

[69] F. Liu, K. Richard, and W. F. Block. Mrilab: Performing fast 3D parallel MRI numerical simulation on a simple PC. In *The International Society for Magnetic Resonance in Medicine (ISMRM) 21th Annual Meeting, April 20-26,2016, Utah, USA*, page 2072. ISMRM, 2013.

[70] J. P. Wansapura, S. K. Holland, R. S. Dunn, and W. S. Ball. NMR relaxation times in the human brain at 3.0 tesla. *Journal of Magnetic Resonance Imaging*, 9(4):531–538, 1999.

[71] H. H. Eroğlu and B. M. Eyüboğlu. Design and implementation of a monopolar constant current stimulator. In *The 17th National Biomedical Engineering Meeting,Istanbul, Turkey*, pages 283–286, 2012.

[72] *I. Rectifier, Series PVX6012PbF Microelectronic Power IC Relay*, 2008.

[73] D. C. Ghiglia and M. D. Pritt. *Two-dimensional phase unwrapping: theory, algorithms, and software*, volume 4. Wiley New York, 1998.

[74] B. Spottiswoode. 2D phase unwrapping algorithms, 02 2009. URL: `http://www.mathworks.com/matlabcentral/fileexchange/22504-2d-phase-unwrapping-algorithms`.

[75] O. Dietrich, J. G. Raya, S. B. Reeder, M. F. Reiser, and S. O. Schoenberg. Measurement of signal-to-noise ratios in mr images: Influence of multichannel coils, parallel imaging, and reconstruction filters. *Journal of Magnetic Resonance Imaging*, 26(2):375–385, 2007.

[76] C. Göksu. A programmable current source for magnetic resonance current density imaging (MRCDI) at 3 tesla. Master's Thesis, Middle East Technical University, Turkey, 2014.

[77] R. W. Brown, Y. N. Cheng, E. M. Haacke, M. R. Thompson, and R. Venkatesan. *Magnetic resonance imaging: physical principles and sequence design*. John Wiley & Sons, 2014.

APPENDIX A

PUBLICATIONS AND PATENT APPLICATION DURING MASTER OF SCIENCE STUDY

A.1 Publications During M.Sc. Study

1- N. A. Naji, H. H. Eroğlu, K. Sümser, M. Sadighi and M. Eyüboğlu. Enhancing induced current magnetic resonance electrical impedance tomography (ICMREIT) image reconstruction, *Proceedings of the 12th IASTED International Conference Biomedical Engineering (BioMed 2016), Innsbruck, Austria*, pages 149-154, 2016.

2- K. Sümser, N. Naji, M. Sadighi, H. H. Eroğlu and B. M. Eyüboğlu. MRI-SPAMM based Magnetic Resonance Electrical Impedance Tomography, *Proceedings of the 24th ISMRM Annual Meeting, Singapore,Singapore*, page 1940, 2016.

A.2 Patent Application During M.Sc. Study

1- K. Sümser, M. Sadighi, N. Naji, H. H. Eroğlu and B. M. Eyüboğlu. Spin Etiketli Manyetik Rezonans Akım Yoğunluğu ve Elektriksel Empedans Görüntüleme, *Pending Patent*, TR 2015/13995.